

THE UNIVERSITY OF CHICAGO

A BIOPHYSICAL EXPLORATION OF ALPHA-SYNUCLEIN BINDING TO MODEL
MEMBRANES

A DISSERTATION SUBMITTED TO
THE FACULTY OF THE DIVISION OF THE PHYSICAL SCIENCES
IN CANDIDACY FOR THE DEGREE OF
DOCTOR OF PHILOSOPHY

DEPARTMENT OF CHEMISTRY

BY
BENJAMIN R. SLAW

CHICAGO, ILLINOIS

JUNE 2022

TABLE OF CONTENTS

LIST OF FIGURES	v
LIST OF TABLES.....	vii
LIST OF APPENDICES.....	viii
LIST OF ABBREVIATIONS.....	ix
ACKNOWLEDGEMENTS.....	xi
ABSTRACT.....	xiv
1. BACKGROUND	
1.1: History	1
1.2: Structural characteristics of α Syn	3
1.3: α Syn's role <i>in vivo</i> : Observations from biology and physiology	4
1.3.1: Genetics studies	4
1.3.2: The synaptic vesicle cycle	6
1.4: α Syn and the lipid membrane: Observations from biophysical studies.....	8
1.5: Specific aims and organization of this thesis.....	14
1.6: List of publications	16
1.7: References.....	17
2. DEVELOPMENT OF A NOVEL CONFOCAL BINDING ASSAY TO QUANTITATIVELY MEASURE PROTEIN/VESICLE BINDING	
2.1: Overview.....	22
2.2: Methods	25
2.2.1: Confocal Microscopy.....	25
2.2.2: Preparation of small unilamellar vesicles (SUVs) <i>via</i> freeze-thaw extrusion.....	32
2.2.3: Preparation of microscope slides and samples for protein binding assay....	32
2.2.4: Instrumental settings and image collection protocol	34
2.2.5: Image analysis.....	38
2.2.6: Considerations for robust data collection	43
2.3: Case study: Using the confocal binding assay to observe annexin binding	44
2.3.1: Materials	45
2.3.2: Confocal microscope parameters.....	46
2.3.3: Results.....	47
2.3.4: Discussion.....	48
2.4: References.....	49
Appendix 2.1: prepareDataForAnalysis.m	52

Appendix 2.2: extractDetectionInfo.m	54
3. THE IMPACT OF MEMBRANE DEFECT PRESENTATION ON ALPHA-SYNUCLEIN BINDING TO MODEL MEMBRANES	
3.1: Overview.....	56
3.2: Review of packing defects.....	59
3.3: Materials and methods.....	63
3.3.1: Protocol for creating osmotically-stressed vesicles.....	64
3.3.2: Confocal microscopy parameters.....	64
3.3.3: Molecular dynamics simulations	65
3.3.4: Quantifying membrane defect presentation using PackMem	65
3.4: Osmotic tension does not appear to measurably impact α Syn binding	67
3.5: α Syn exhibits differential binding as a function of lipid tail composition	70
3.6: Discussion.....	72
3.7: References.....	78
4. THE C-TERMINAL DOMAIN OF ALPHA-SYNUCLEIN CONFERS STERIC STABILIZATION ON SYNAPTIC VESICLE-LIKE SURFACES	
4.1: Overview.....	80
4.2: Methods	82
4.2.1: Theory of small-angle x-ray scattering (SAXS).....	82
4.2.2: Preparation of synaptic vesicle mimics using spherical-nanoparticle supported lipid bilayers (SSLBs).....	87
4.2.3: Protein purification	88
4.2.4: SAXS sample prep and PEG-induced depletion protocol	89
4.3: Results.....	90
4.3.1: The C-terminal domain is responsible for dispersing synaptic vesicle mimics.....	90
4.3.2: Electrostatics and steric contributions both play a role in steric stabilization.....	93
4.3.3: Divalent ions alter the force response behavior of synaptic vesicle mimics in the presence of α Syn	95
4.4: Significance of α Syn's C-terminal domain in physiology and pathology	96
4.5: References.....	100
5. QUANTITATIVE ANALYSIS OF TOTAL REFLECTION X-RAY FLUORESCENCE FROM FINELY LAYERED STRUCTURES USING XERAY	
5.1: Overview.....	102
5.2: Background.....	102
5.3: Theory of Total Reflection X-ray Fluorescence (TXRF)	105
5.4: Methods	110
5.4.1: Protocol for running TXRF experiments on Langmuir monolayers at the air/fluid interface.....	110

5.4.2: Explanation of the XeRay tool and improvements over traditional data analysis methods	111
5.5: Case study 1: Using XeRay to determine Ca ²⁺ accumulation underneath an SOPA monolayer	115
5.6: Case study 2: Using XeRay to analyze fluorescence data obtained from a dodecane/surfactant/water interface.....	122
5.7: Conclusions.....	124
5.8: Notes	125
5.9: References.....	126
6. LESSONS LEARNED FROM THE CREATION AND DEVELOPMENT OF A RESEARCHER-LED SAFETY ORGANIZATION AT THE UNIVERSITY OF CHICAGO	
6.1: Overview.....	128
6.2: Background.....	129
6.3: The advent and expansion of safety teams in the United States	131
6.4: Creation of the JRSI at The University of Chicago	133
6.5: Description and analysis of implemented programs and events.....	136
6.5.1: Development of the JRSI's organizational structure	136
6.5.2: Evaluating safety culture and organizational effectiveness	138
6.5.3: Educating researchers, teachers, and safety contacts.....	139
6.5.4: Facilitating open dialogues and collaborations.....	142
6.5.5: Defragmenting safety efforts and resources	146
6.6: Conclusions.....	148
6.7: References.....	150
Appendix 6.1: Handout for first-year training	153
Appendix 6.2: Lab Safety Contact (LSC) Responsibilities and Guidebook.....	154
Appendix 6.3: Peer Lab Walkthrough Scoring Rubric 2019	175
7. CONCLUSIONS	
7.1: Summary of findings and comments	183
7.2: Future directions	185
7.2.1: Probing α Syn binding with confocal microscopy.....	185
7.2.2: The C-terminal domain and steric stability <i>in vivo</i>	187
7.3: References.....	189

LIST OF FIGURES

1.1	α-Synuclein has been shown to adopt an alpha-helical structure upon membrane binding	2
1.2	Overview of the synaptic vesicle cycle.....	5
1.3	Computational study shows that increasing membrane curvature also increases transient lipid defect presentation.....	8
1.4	Packing defect presentation in both leaflets of a simulated membrane with enforced curvature	10
1.5	Sample perturbations that can result in increased presentation of packing defects in lipid membranes	11
1.6	Hypothesized conformations of membrane-bound α-Synuclein	13
2.1	Cartoon of the vesicle immobilization scheme utilized in the confocal assay	24
2.2	Diagrammatic comparison of brightfield and confocal microscopy.....	26
2.3	Two lenses in a simplified optical path demonstrate how a pinhole works in confocal microscopy	27
2.4	Diffraction-limited signals produce individual Airy patterns which need to be resolved for sub-pixel localization	29
2.5	Impact of the microscope point spread function (PSF) on collected images.....	31
2.6	Sample chamber used in the confocal binding assay.....	33
2.7	Spot detection and significance testing employed by cmeanalysis	39
2.8	Sample binding curve obtained using the confocal assay.....	42
2.9	Sample images of annexin-V-CF555 binding obtained using the confocal assay.....	46
2.10	Annexin-V binding curve for 25 mol% DOPS vesicles obtained using the confocal fluorescence assay.....	47
3.1	Vesicle swelling as a result of osmotic pressure produces large increases in the vesicle surface area	57
3.2	Lipid molecular geometry helps to predict pure equilibrium packing.....	60
3.3	Sample plots displaying the probability of finding a defect of a given area in a simulation.....	67
3.4	Sample images of HiLyte Fluor 488-tagged αSyn binding obtained using the confocal assay	68
3.5	Aggregate mean relative intensity data for αSyn binding to osmotic vesicles	69
3.6	Linear regression fitting and packing defect size constants obtained from molecular dynamics simulations of a membrane under variable lateral tension	70
3.7	Aggregate mean relative intensity data for αSyn binding to monounsaturated and di-monounsaturated vesicles	71
4.1	Diagram of the interaction between a point scatterer and an x-ray	82
4.2	Sample SAXS scattering profile obtained for 60 nm silica nanoparticles in solution.....	85
4.3	An interparticle correlation peak emerges in the SAXS profile as the volume fraction of scattering particles increases	86
4.4	αSyn-SSLBs remain dispersed in solution until a critical concentration of osmotic depletant is added.....	91

4.5	The critical osmotic pressure required for clustering α Syn-SSLBs changes as a function of protein length and electrostatic screening	92
4.6	Dilution experiments demonstrate that the clustering of α Syn-SSLBs is reversible.....	94
4.7	Depletion attraction-induced clustering is enhanced with small amounts of divalent ions in solution.....	95
4.8	Calcium-induced clustering of α Syn-SSLBs without osmotic depletant is not reversible.....	97
5.1	Schematic of the air/liquid TXRF setup	109
5.2	Two integration scenarios of the x-ray fluorescence signal.....	113
5.3	Fluorescence spectra and integrated signal from the bulk.xfluo data file.....	117
5.4	Fitted bulk.xfluo data set and visualization of the likelihood distribution of the angle offset	119
5.5	Example of an improperly set fitting range	120
5.6	Fitting results for 1 mM CaCl ₂ with an SOPA film.....	121
5.7	Fitting results for the dodecane/water calibration sample	123
5.8	Fitting results for Sr ²⁺ fluorescence from a dodecane/surfactant/water interface.....	124
6.1	Schematic representation of organizational culture based on Edgar Schein's levels of culture	131
6.2	Student-led safety initiatives and teams in the U.S. that were established through partnership with The Dow Lab Safety Academy.....	132
6.3	Responsibilities of and collaboration between EH&S, ORS, and the JRSI.....	135
6.4	Photographs from the Peer Lab Walkthrough event.....	144

LIST OF TABLES

3.1	Vesicle compositions utilized in chapter 3	63
-----	--	----

LIST OF APPENDICES

2.1	prepareDataForAnalysis.m	52
2.2	extractDetectionInfo.m	54
6.1	Handout for first-year training	153
6.2	Lab Safety Contact (LSC) Responsibilities and Guidebook.....	154
6.3	Peer Lab Walkthrough Scoring Rubric 2019.....	175

LIST OF ABBREVIATIONS

α Syn	α -synuclein
NAC	Non-amyloid component
PD	Parkinson's disease
SV	Synaptic vesicle
ALPS	Amphipathic lipid packing sensor
JRSI	Joint Research Safety Initiative
AFM	Atomic force microscopy
SPR	Surface plasmon resonance
SUV	Small unilamellar vesicle
SLB	Supported lipid bilayer
PMT	Photomultiplier tube
APD	Avalanche photodiode
NA	Numerical aperture
PSF	Point spread function
HBS	HEPES-buffered saline
DLS	Dynamic light scattering
DOPC	1,2-dioleoyl- <i>sn</i> -glycero-3-phosphocholine
PE	Phosphoethanolamine (lipid headgroup)
WLL	White light laser
HyD	Hybrid GaAsP/photomultiplier tube detector
SMD-HyD	Single molecule sensitive hybrid GaAsP/photomultiplier tube detector
AOBS	Acousto-optical beam splitter
LoG	Laplacian-of-Gaussian
BSA	Bovine serum albumin
DOPS	1,2-dioleoyl- <i>sn</i> -glycero-3-phosphatidylserine
Cy5-PE	1,2-dioleoyl- <i>sn</i> -glycero-3-phosphoethanolamine-N-(Cyanine 5)
AV-CF555	Annexin-V-CF555
DPPC	1,2-dipalmitoyl- <i>sn</i> -glycero-3-phosphocholine
DOPA	1,2-dioleoyl- <i>sn</i> -glycero-3-phosphate
16:0 lyso PC	1-palmitoyl-2-hydroxy- <i>sn</i> -glycero-3-phosphocholine
DOG	1,2-dioleoyl-glycerol
DMPC	1,2-dimyristoyl- <i>sn</i> -glycero-3-phosphocholine
POPC	1-palmitoyl-2-oleoyl- <i>sn</i> -glycero-3-phosphocholine
ASA	Accessible surface area
HBS-150	HEPES-buffered saline with 150 mM glucose
HBS-105	HEPES-buffered saline with 105 mM glucose
SSLB	Spherical-nanoparticle supported lipid bilayer
SAXS	Small-angle x-ray scattering
XPCS	X-ray photon correlation spectroscopy
PEG	Polyethylene glycol
α Syn Δ CTD	C-terminal tail truncated α -synuclein (residues 1-101)

MWC	Molecular weight cutoff
PEG10k	Polyethylene glycol with molecular weight cutoff = 10,000 Daltons
TXRF	Total reflection x-ray fluorescence
XANES	X-ray absorption near edge spectroscopy
SOPA	1-stearoyl-2-oleoyl- <i>sn</i> -glycero-3-phosphate
GUI	Graphical user interface
TRR	Trust region reflective
DMPA	1,2-dimyristoyl- <i>sn</i> -glycero-3-phosphate
DHP	Di-hexadecyl phosphate
OSHA	Occupational Safety and Health Administration
DLSA	Dow Lab Safety Academy
UMN JST	University of Michigan Joint Safety Team
ACS	American Chemical Society
EH&S	Environmental Health and Safety
ORS	Office of Research Safety
PME	Pritzker School for Molecular Engineering
IME	Institute for Molecular Engineering
LSC	Lab safety contact
PI	Principle investigator
IRB	Institutional Review Board
DPhPC	1,2-diphytanoyl- <i>sn</i> -glycero-3-phosphocholine

ACKNOWLEDGEMENTS

To say that graduate school has been difficult for me would be the understatement of the century; I truly would not have been able to come this far and produce the work you're about to read if I didn't have the support of a robust network of colleagues, friends, and family.

First, I'd like to thank my faculty advisor, Ka Yee Lee, for her patience and support as I grew into the scientist I am today. Ka Yee did a fantastic job at creating a lab where people like me could be truly independent and pursue the research questions that motivate them, even if they encounter a few (or in my case, a lot) of setbacks along the way. She always met my frustrations at a lack of results or experimental difficulties with patience and grace, and encouraged me to think about problems differently to arrive at a feasible solution; I would not be where I am today were it not for her support.

Next, I need to acknowledge the support and contributions of my labmates – Dan, Luke, Zhiliang, Sofi, Miah, Sam, Alessandra, and Pascale. I truly cannot emphasize the important roles they've all played in shaping my mentality as a scientist, a mentor, and a mentee, from our hours-long debates about niche scientific topics after a seminar or group meeting, to the panicked late-night slack chats where data just wasn't making any sense. You all have offered me kindness, comradery, and friendship during the most difficult times of my graduate school career. From the bottom of my heart, thank you.

I would also like to thank Christine Labno, Shirley Bond, and Vytas Bindokas from the Integrated Light Microscopy Core for all of their help and support as I developed the confocal

binding assay outlined in chapter 2 of this thesis. Whenever I had difficulties with the instruments or extremely technical questions about how they worked, Christine, Shirley, and Vytas did their absolute best to help fix the problem, answer my questions, or point me in the direction of someone who knew the answers they didn't. It was truly a delight to get to spend so much time in the microscopy core with people who are so immensely invested in and knowledgeable of their work.

During my time in graduate school I have also been heavily involved in departmental affairs, from organizing Tiger Talks to sitting on many different committees aimed at addressing systemic problems within the department. An enormous amount of my success in these roles can be attributed to Vera Dragisich, who has always been willing to make time to strategize or bounce ideas around to help better the department. Vera, your presence in the department and your efforts to help improve it have truly made a huge impact on how I approach difficult situations in my personal life and beyond. Thank you for your constant support, and for always making time for a quick "cheers" at departmental events.

And finally, immense thanks are due to my friends and family who supported me through both the highs and lows of my graduate school journey. Dad, Susan, and David, thank you for your continuous support despite knowing absolutely nothing about what I was working on or what the end goal was. Brian, Lauren, Julie, Dave, Lucia, Eric, Laura, Link, Sheikh, and Beau, thank you for the wonderful family dinners, extended camping trips, and video game nights that helped keep me sane in the face of adversity. Omar and Romeo, thank you for always listening to me vent about whatever my frustrations were, for all of the wonderful cooking adventures we've shared when I

could get away from lab, and for the constant reassurance that I could, in fact, do this. Turns out, you were right all along.

ABSTRACT

This dissertation work aims to explore the interactions of α -synuclein, an intrinsically disordered protein found primarily in neurons, with model lipid vesicles. α -synuclein is of particular interest to researchers due to its implicated role Parkinson's disease, dementia with Lewy bodies, and other common neurodegenerative disorders classified as synucleinopathies. Current knowledge suggests that α -synuclein plays a role in the synaptic vesicle cycle by binding to loaded synaptic vesicles ready for exocytosis, but more work is required to elucidate the protein's exact function *in vivo*. One particularly interesting hypothesis that has emerged in recent years is that α -synuclein may be able to differentiate between potential vesicular binding partners by sensing their size or curvature; ample experimental evidence supports this phenomenon, but the exact mechanism that α -synuclein uses to "sense" such small changes in curvature remains unknown.

In this work, I will describe several lines of evidence to support the hypothesis that α -synuclein senses membrane curvature by probing differences in membrane hydrophobic defect presentation. First, I will describe a novel confocal binding assay developed to explicitly study α -synuclein binding on a per-vesicle level; this method offers many advantages over more traditional protein binding assays, including very low sample consumption as well as the ability to quantify the total amount of protein bound under membrane-saturating conditions. When this new methodology is used in conjunction with molecular dynamics simulations to quantify membrane defect presentation, we find that membranes displaying more and larger defects display more bound protein at saturation than membranes of similar composition displaying fewer defects. Additionally, we explore the impact of a hypo-osmotic pressure and subsequent vesicle swelling

on membrane defect presentation and α -synuclein binding. When similar experiments using the confocal binding assay are performed on hypo-osmotically stressed vesicles, we find that the resulting differences in membrane defect presentation are likely too small to meaningfully impact α -synuclein binding on a macroscopic scale. Overall, these findings support the idea that α -synuclein senses curvature through membrane defect presentation, and suggests that both the lipid composition and osmotic pressure of synaptic vesicles may play a role in helping α -synuclein to determine its physiological binding partners.

CHAPTER 1.

BACKGROUND

Section 1.1: History

The first synuclein protein was originally identified in 1987 in the Torpedo electric organ as a 143-amino acid protein expressed solely in neurons and primarily localized to the nucleus and the presynaptic nerve terminal [1]. Shortly thereafter, amino acid sequencing of amyloid plaques in Alzheimer's patients revealed a similar peptide inclusion that was dubbed the "non-A β component of AD amyloid," or NAC, arising from a truncation of the 140-amino acid NAC precursor protein [2]. Since then, a large body of research has developed around what would later be called the synuclein family of proteins, comprised of three close homologues (α -, β -, and γ -synuclein) with a highly conserved N-terminal domain across multiple vertebrate species [3-5]. Though all three synucleins are hypothesized to play a role in normal neuronal function and plasticity, α -synuclein (α Syn) has received the most attention due to its appearance in Lewy bodies, a proteinaceous inclusion that is the main symptomatic hallmark of Parkinson's disease in brain tissues [6].

In the years since α Syn was first identified, it has been found to play a role in a wide variety of neurodegenerative diseases, including the aforementioned Alzheimer's disease, Parkinson's disease, dementia with Lewy bodies, and multiple system atrophy [7, 8]. In fact, the link between α Syn dysfunction and the onset of neurodegenerative diseases appears so strong that these pathologies have collectively come to be referred to as "synucleinopathies." While many interactions and behaviors of α Syn have been elucidated in the years since its discovery, much

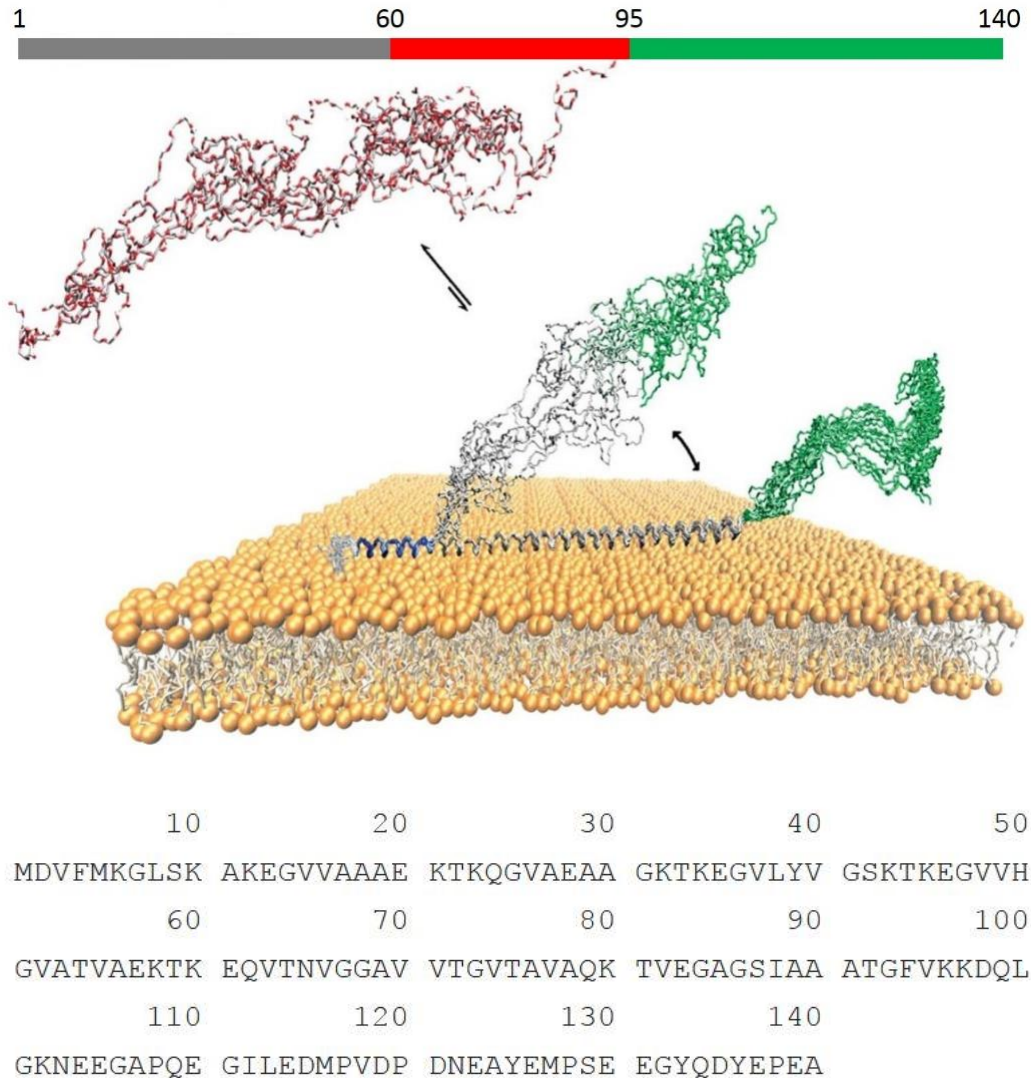


Figure 1.1: α -Synuclein has been shown to adopt an alpha-helical structure upon membrane binding. (Top): While intrinsically disordered in solution, both solution and solid-state NMR experiments have shown that the N-terminal domain (residues 1-95) of α -synuclein adopts an alpha-helical secondary structure upon associating with model synaptic vesicles. The C-terminal domain (residues 96-140) remains intrinsically disordered, and is hypothesized to project off of the membrane surface due to its relatively high density of negatively charged residues. (Bottom): Canonical amino acid sequence of the full-length protein. (Top) adapted from [9], (Bottom) reproduced from the UniProt database [85].

remains unknown about its normal physiological role in neurons or the processes that contribute to its dysfunction.

Section 1.2: Structural characteristics of α Syn

Alpha-synuclein is a 140-amino acid intrinsically disordered protein that has been shown to adopt a partial alpha-helical structure upon binding to lipid membranes (Figure 1.1) [9]. Broadly speaking, the protein can be divided into three structural domains:

- The N-terminal region typically refers to the first 60 amino acids of the protein, which contains a number of positively charged lysine residues that are hypothesized to play a critical role in protein/membrane interactions.
- The non-amyloid component region (NAC region) consists of residues 61-95, and has been heavily implicated in α Syn aggregation associated with Parkinson's disease (PD) [10]. Deletion or truncation of this region has been shown to reduce α Syn aggregation and fibril formation associated with PD. It should also be noted that some studies refer to residues 1-95 as the "N-terminal domain" due to the seven imperfect 11-mer repeat sequences which adopt an alpha-helical formation upon membrane binding [11, 12].
- The C-terminal region is comprised of amino acids 96-140 and contains a high density of negatively charged residues at physiological pH. Unlike the N-terminal domain, this region remains intrinsically disordered upon membrane binding. Additionally, the C-terminus of α Syn has been shown to have a plethora of binding partners, ranging in size from individual ions to other synaptic proteins. While the impact of the C-terminal region in diseases like PD is still unknown, its presence in the wild-type protein seems to inhibit α Syn aggregation and could potentially impact the overall membrane binding process.

While a large amount of research has been done exploring the structural impact of α Syn on aggregation and fibril formation, such information lies outside the scope of this work. For an overview on these topics, the reader is directed to the following review articles which offer summaries of the current knowledge surrounding the diseased states of α Syn [13-15].

Section 1.3: α Syn's role *in vivo*: Observations from biology and physiology

Section 1.3.1: Genetics studies

The lack of consensus about α Syn's behavior can be partially attributed to the inconsistent and often conflicting conclusions drawn from both cellular and animal studies. For example, a study examining the impact of deleting only the α -homologue synuclein in mice found that such a deletion resulted in reduced learning ability for tests involving working and spatial memory [16]. Another study involving both single- and double-knockout mouse models for α - and β -synuclein found that the deletion of these proteins caused no major impairment of basic brain function or overall rate of survival [17]. A later α -, β -, and γ - triple-knockout mouse study showed that deletion of the full synuclein family results in age-dependent neuronal dysfunction, alterations in synapse structure and transmission, and an overall decreased rate of survival [18], but these results conflict with the findings of a similar study which found no changes in synaptic structure and slight changes in dopamine handling in triple-knockout mice [19]. More recently, researchers have tried to address these discrepancies by studying and comparing mouse models with different combinations of synuclein knockouts, but their findings only serve to complicate the picture further [20].

Cellular models examining the impact of α Syn overexpression and depletion offer a bit more clarity into its potential physiological role. One study involving acute hippocampal slices obtained from a mouse model found that overexpression of α Syn resulted in reduced synaptic vesicle (SV) exocytosis and an overall reduction in size of both the readily releasable and recycling synaptic vesicle pools [21]. A similar study using PC12 and chromaffin cells found that α Syn overexpression results in impaired dopamine release and SV exocytosis while also increasing the number of docked vesicles at the inner plasma membrane [22]. In contrast to these findings,

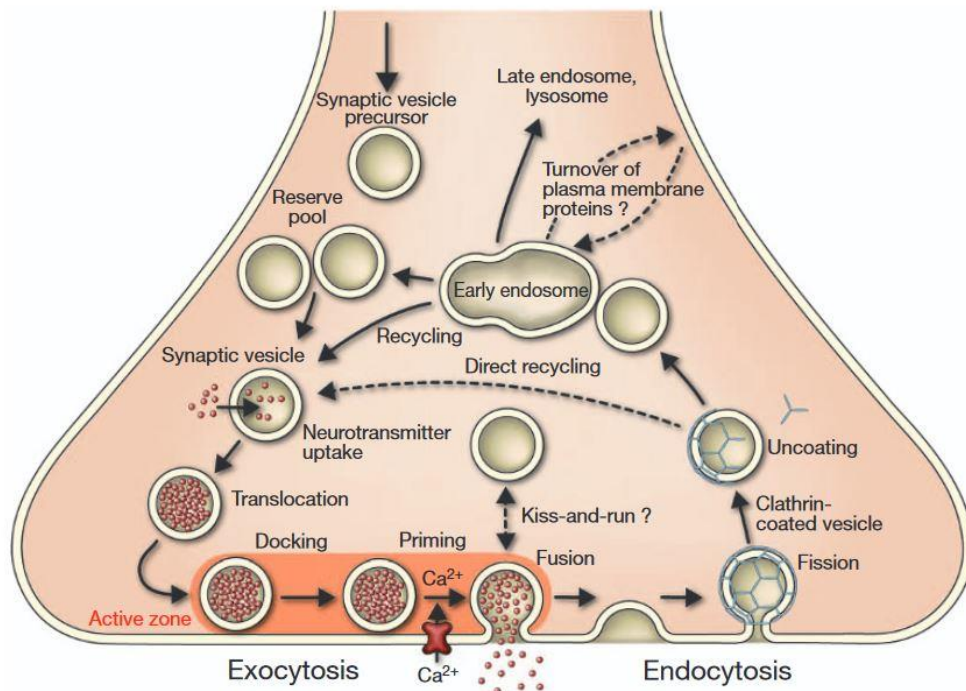


Figure 1.2: Overview of the synaptic vesicle cycle. Pictured above is a simplified diagram of the synaptic vesicle cycle. After synaptic vesicle components are brought to the synapse from elsewhere in the neuron, they are incorporated into the early endosome. A concerted effort of various proteins causes individual synaptic vesicles of the proper size (~50 nm) to bud off and separate from the endosome. These vesicles are subsequently loaded with neurotransmitter via the combined efforts of a vacuolar-type proton pump, which creates a proton gradient across the lipid membrane, and a neurotransmitter transporter which uses this proton gradient to facilitate loading. Filled synaptic vesicles are then translocated to the active zone of the synapse, where they undergo docking and priming to prepare for exocytosis. When the synapse receives a calcium influx, the primed synaptic vesicles undergo rapid fusion and exocytosis to release their neurotransmitter contents into the synaptic cleft. Spent vesicles are then endocytosed and recycled to begin the cycle anew, but the details on the exact mechanisms for this are still actively debated. Adapted from [24].

another study examined hippocampal synapses in α Syn-knockout mice and found impairments in synaptic response and slower replenishment of plasma membrane-docked vesicles compared to their wild-type counterparts [23]. With this information, what conclusions then are we to make about α Syn's role in vivo? While some of the discrepancies in reported results could possibly be attributed to differences in experimental conditions and selected models, these data taken together suggest that α Syn has a complicated and nuanced role in the long-term regulation of neurotransmitter release and synaptic vesicle pool maintenance.

Section 1.3.2: The synaptic vesicle cycle

One hypothesis for the role of α Syn in vivo that emerges from its prevalence and localization in the synaptic terminal is that it could play a role in maintaining the synaptic vesicle cycle. The synaptic vesicle cycle refers to the continuous series of events associated with neurotransmission, outlined in figure 1.2 [24]. Briefly, synaptic vesicles are loaded with neurotransmitter within the synapse and transported to the presynaptic active zone, where they undergo docking, priming, and eventually exocytosis. Membrane components of synaptic vesicles are then recovered via endocytosis and translocated back into the so-called "reserve pool" of vesicles to undergo neurotransmitter loading again; this process repeats ad infinitum, hence describing it as a cycle.

While the overall steps of the SV cycle appear to be relatively straightforward, many questions still remain about the molecular-level interactions that contribute to the macroscopic observed behavior. For example, a number of studies have demonstrated the importance of the SNARE protein machinery in docking, priming, and fusing vesicles for neurotransmitter

exocytosis [25, 26], but more information is still needed to determine how such a machinery interacts with other scaffolding proteins or the impact of such an interaction on exocytosis [27]. Additionally, there is still much debate in the field about how SV components are salvaged post-exocytosis, with four endocytic pathways currently identified based on empirical differences in their speed and molecular mechanisms [28, 29]. Further on in the cycle, there are also outstanding questions regarding how recycled SVs are clustered into different, spatially-segregated pools within the neuronal terminal [30]. α Syn could play a role in any or all parts of the SV cycle due to its high abundance in the neuronal cytoplasm [31]; more research is clearly necessary to elucidate the molecular drivers of SV cycling and how α Syn fits into the bigger picture.

α Syn's potential role in the SV cycle is both complicated and obfuscated by the different molecules with which the protein has been reported to interact. Over the last decade, several studies have aimed at elucidating α Syn's protein interactome via co-immunoprecipitation assays [32], bioinformatics [33], and other biochemical methods [34]; notably, the large variety of proteins throughout the neuron that have been reported to interact with α Syn are emblematic of the promiscuity it seems to have in selecting binding partners. This promiscuity is further evidenced by the plethora of small-molecule ligands with which α Syn has been shown to interact, including Ca^{2+} [35, 36], Cu^{2+} [37, 38], dopamine [39], and a variety of other biologically-relevant divalent cations [40]. Taken together with the high sequence similarity and potential compensatory function of β - and γ -synucleins [18, 41], it becomes clear that much remains to be explored to assess α Syn's normal physiological role *in vivo*.

Section 1.4: α Syn and the lipid membrane: Observations from biophysical studies

Of particular interest to the biophysics community is α Syn's interaction with lipid membranes. α Syn belongs to a class of proteins hypothesized to have the ability to “sense” membrane curvature, a key physical property of lipid membranes. Physiologically, this sensitivity for curved membranes likely plays a role in both protein sorting and activity, and a variety of mechanisms for generating and enforcing membrane curvature have been identified in recent years [for a good review of the mechanisms of membrane curvature generation, see 42]. From within the membrane, curvature can be generated via altering lipid composition [43-45], conformational changes or specific localization of integral membrane proteins [46], or through the hydrophobic insertion of membrane-binding proteins [47-50]. Forces outside of the membrane can also result

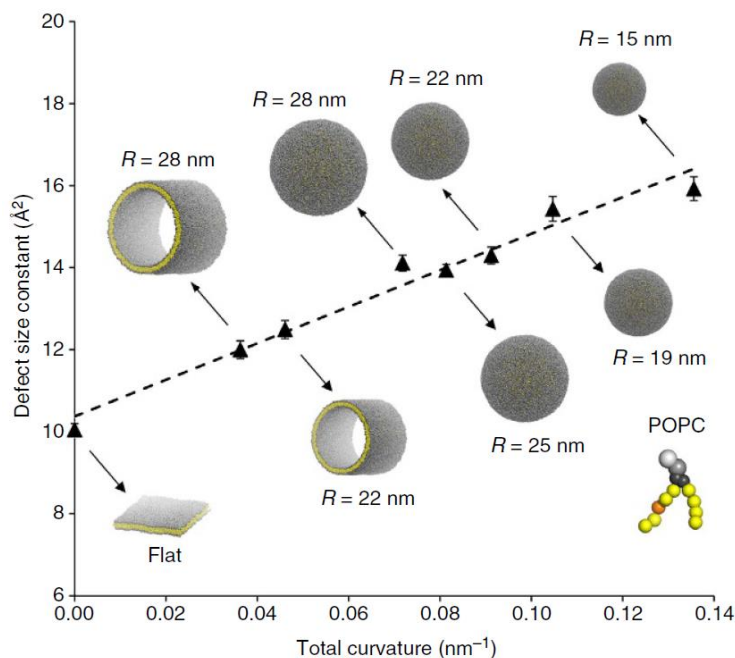


Figure 1.3: Computational study shows that increasing membrane curvature also increases transient lipid defect presentation. In this study, the authors used coarse-grained molecular dynamics simulations to show that increasing the total curvature of a membrane also increases the packing defect size constant, which can be interpreted as measure of both the size and frequency of defects in a membrane. A higher defect size constant corresponds to both larger and greater presentation of defects, whereas a smaller size constant implies fewer and smaller defects. Simulations were conducted using a pure POPC membrane and the GROMACS 4 simulation package. Reproduced from [55].

in the generation of a specific curvature, such as the association of crescent-shaped BAR domains [51], oligomerization of different membrane-associated proteins [52], or active transport along cell structural elements [53]. The breadth and robust nature of curvature-generating processes suggests that membrane curvature plays an important role in many physiological processes.

Despite our demonstrated understanding of how lipids and proteins can influence membrane curvature, a variety of questions remain unanswered about how a given protein can actually “sense” this curvature *in vivo*. One hypothesis proposes that protein geometry can confer curvature sensitivity; such curvature-sensing proteins often exhibit a concave or convex surface displaying solvent-exposed cationic side chains which can preferentially adsorb onto a membrane containing anionic lipid headgroups [54]. In contrast to this hypothesis, other proteins are believed to sense curvature through the recognition of lipid packing defects since it is well-documented that the presentation of such defects increases with increasing membrane curvature (figures 1.3, 1.4) [55, 56]. Proteins that can sense lipid packing defects typically do so via an intrinsically-disordered amphipathic lipid packing sensor (ALPS) motif that adopts an alpha-helical structure upon membrane binding [57-59]. Though ALPS motifs have been identified with a variety of amino acid sequences, a unifying theme is that such motifs tend to exhibit unique amphipathic properties [60]. Typically, the adoption of an alpha-helix upon membrane binding results in the formation of hydrophobic and hydrophilic regions on opposing faces of the helix; this allows a protein with an ALPS motif to make favorable hydrophobic contacts between its aliphatic side chains and the hydrophobic core of the membrane while keeping the hydrophilic face hydrated. Thus, the phenomenon of curvature sensing by ALPS motifs and other proteins is considered to be

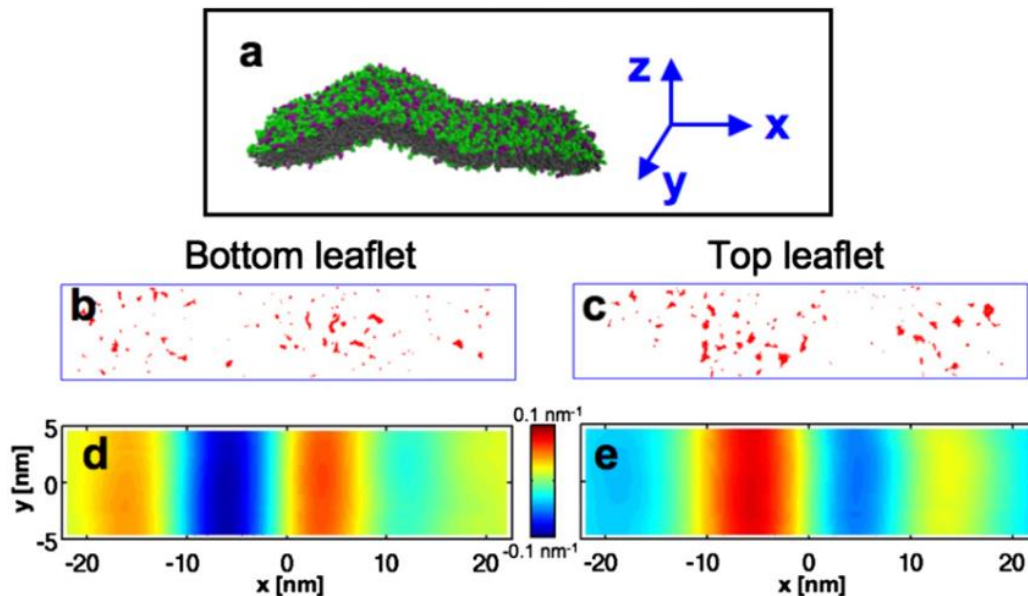


Figure 1.4: Packing defect presentation in both leaflets of a simulated membrane with enforced curvature. In the simulations represented above, a 3:7 mol% DOPC:DOPS membrane patch was subjected to varying amounts of curvature and the resulting membrane packing defect presentation was analyzed as a function of the imposed curvature. (a): Snapshot of the simulated membrane used for this analysis. (b): Bottom-up view of the defect presentation in the bottom leaflet; red patches represent observed defects, or regions where the hydrophobic core of the membrane is transiently exposed to the surrounding solvent. (c): Top-down view of the defect presentation in the top leaflet. (d): Heatmap representing the local curvature of the bottom leaflet; warm regions indicate more positive curvature, whereas cold regions indicate more negative curvature. (e): Heatmap representing the local curvature of the top leaflet. Reproduced from [89].

entropically-driven because increased presentation of membrane defects allows for greater conformational flexibility upon membrane binding [61].

Many experimental studies involving model lipid membranes have demonstrated that α Syn exhibits curvature sensitivity similar to that of the ALPS motif [62, 63]. In fact, some studies have reported that the binding affinity of α Syn for target membranes can increase by as much as two orders of magnitude depending on the membrane curvature [64, 65]. Such an increase in binding is consistent with the aforementioned hypothesis that curvature sensitivity arises from increased presentation of membrane defects; as a membrane becomes more and more curved, the lateral

packing of lipids in the outer leaflet decreases such that the energetic cost of burying hydrophobic side chains in the membrane core also decreases, leading to increased affinity. This picture of α Syn binding, though consistent, omits the fact that the size of synaptic vesicles is subject to change *in vivo* as a result of neurotransmitter loading, from around 40 nm to 60 nm in diameter [66]. Understanding how small changes in curvature resulting from osmotic loading impact α Syn binding will no doubt be important for elucidating its role in the SV cycle.

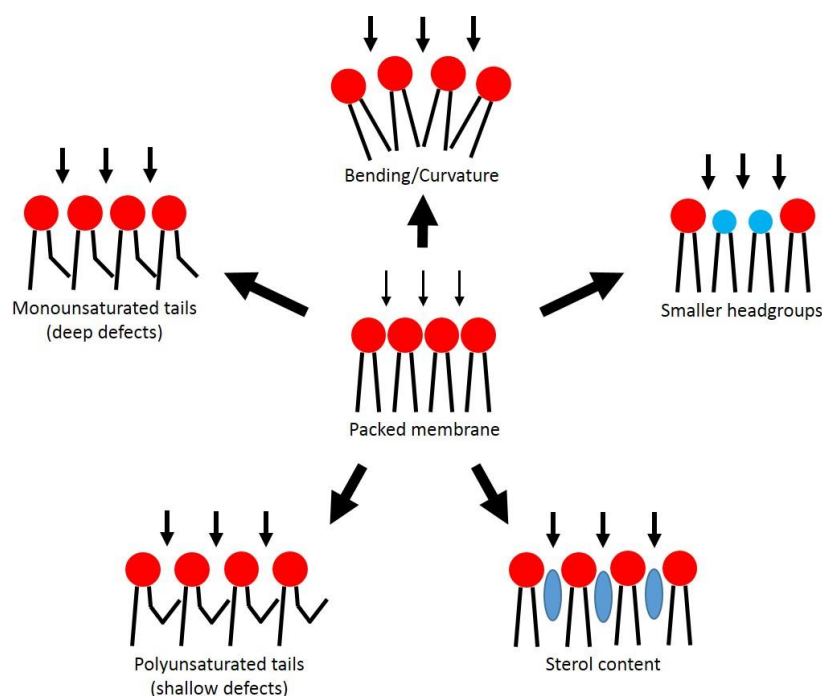


Figure 1.5: Sample perturbations that can result in increased presentation of packing defects in lipid membranes. Pictured above are several perturbations that have the propensity to result in increased membrane defect presentation. Considering a flat, saturated membrane as reference, defect presentation can be increased by (1) bending or enforcing curvature on the membrane, which would give rise to more defects due to geometrical restraints in packing, (2) substituting monounsaturated for saturated lipid tails, where a kink in the monounsaturated tails prevents efficient packing and results in more deep defects, (3) substituting polyunsaturated for saturated lipid tails, which manifests more shallow defects due to the large amount of flexibility of the polyunsaturated chains, (4) increasing the sterol content, which has long been shown to interrupt efficient packing of saturated tails, or (5) substituting smaller headgroups (such as phosphatidic acid, PA) for larger ones (such as phosphatidylcholine, PC), which introduces surface roughness into the outer leaflet of the membrane. Adapted from [73].

Despite its clearly demonstrated impact on α Syn's behavior, membrane curvature is not the only physical parameter that has been shown to be important to α Syn's binding affinity. α Syn's affinity for membranes has also been shown to be influenced by (1) the membrane charge, where more anionic lipids lead to better binding [67, 68], (2) temperature, where the protein has been shown to adopt different conformations at higher temperatures and in different lipid phase states [68, 69], and (3) overall membrane lipid composition, where the lipid head groups, tails, and sterol content all appear to play a role in binding [69-72]. Studies involving changes to the vesicle lipid composition in particular offer even more support for the hypothesis that α Syn senses membrane curvature through packing defects; perturbations such as higher degrees of unsaturation in the lipid tails or increased cholesterol content in a rigid membrane would clearly result in changes to the lateral lipid packing (and hence, defect presentation), as illustrated in figure 1.5 [73].

The questions surrounding α Syn's physiological behavior grow deeper when we consider its membrane-bound structure. At present, evidence in the field suggests that α Syn may adopt one of two different conformations upon membrane binding depending on the local environment (figure 1.6). The first conformation features a linear, continuous alpha-helix that spans the entirety of the N-terminal domain (first ~95 residues) with an unusual 11/3 periodicity (in which 11 residues form 3 helical turns) and has been referred to as the "extended-helix" conformation [74, 75]. In contrast, the second conformation is characterized by a break in the binding helix; instead of a linear, continuous helix, this conformation has two distinct helices separated by a non-helical flexible linker region spanning residues ~39-45 and is thus called the "broken-helix" or "horseshoe" conformation [76, 77]. It should also be noted that there is some empirical evidence which suggests that α Syn can interconvert between these two conformations depending on the

protein:lipid or protein:detergent ratio [78]. Considering this, some researchers have speculated that the different membrane-bound conformations play different roles in α Syn's physiology, where some outside mechanism (such as post-translational modification) is responsible for causing the transition between states. Though an attractive hypothesis, to date no link between such outside mechanisms and α Syn's binding conformation has been identified.

The existence of the broken-helix conformation under different conditions has inspired some researchers to explore whether this binding mode plays a specific role in α Syn's physiology. A number of such studies have suggested that a broken-helix conformation could allow α Syn to act as a “bridge” between two distinct membranes (e.g., between a synaptic vesicle and the inner plasma membrane [79] or between multiple synaptic vesicles [80, 81]). The latter example is of particular interest because it could offer a partial explanation for the macroscopic organization of

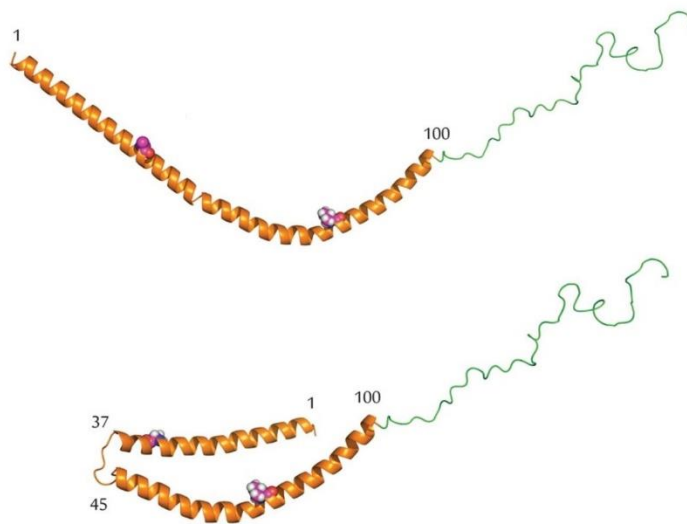


Figure 1.6: Hypothesized conformations of membrane-bound α -Synuclein. Two distinct conformations of membrane-bound α -synuclein are hypothesized to exist depending on the local lipid environment. An extended helix (**top**) has been found to be favored in pulsed dipolar ESR spectroscopy studies involving small unilamellar vesicles (SUVs), rodlike sodium dodecyl sulfate (SDS) micelles, and lipid bicelles [86], whereas a broken helix (**bottom**) has been observed when the protein binds to micelles [87]. Adapted from [88].

synaptic vesicle pools within the neuronal terminal, but more evidence would be needed to support such a mechanism *in vivo*. More recently, alternative hypotheses to explain synaptic pool organization have emerged, including a study suggesting that synapsin-1a (another abundant protein in the neuronal cytoplasm) in sufficient concentrations can form liquid-liquid condensates capable of recruiting SVs [82]. Such condensates have also been shown to recruit α Syn [83, 84], but the implications for this interaction and its impact on the SV cycle have yet to be explored.

Section 1.5: Specific aims and organization of this thesis

This thesis aims to address several questions surrounding the normal physiological function of α Syn and its vesicular binding partners as outlined above. More specifically, I will address the following scientific questions:

- What is the nature of α Syn's vesicular curvature sensitivity, and how can lipid parameters influence α Syn binding?
- What role, if any, does an induced osmotic tension intended to mimic neurotransmitter loading play in helping to determine α Syn binding specificity?
- Once bound, what role does α Syn play in modulating macroscopic synaptic vesicle behavior?
- What is the specific function of the C-terminal domain of α Syn in its normal physiological environment?

In line with the questions above, this thesis is organized as follows: the development of a novel confocal microscopy-based protein binding assay for directly observing protein/vesicle association

under dilute conditions (Chapter 2); exploration of lipid parameters such as lateral tension and defect presentation hypothesized to impact α Syn binding (Chapter 3); the role of α Syn's C-terminal domain in the steric stabilization of synaptic vesicle mimics (Chapter 4). Additionally, I will discuss the development of a method for quantitative analysis of total reflection x-ray fluorescence data on lipid monolayers (Chapter 5), lessons learned from the creation and development of the Joint Research Safety Initiative (JRSI), a student-led safety organization (Chapter 6), and conclusions and future directions (Chapter 7).

Section 1.6: List of publications

Gong, Z., Kerr, D., Hwang, H. L., Henderson, J. M., Suwathee, T., **Slaw, B. R.**, Cao, K. D., Lin, B., Bu, W., Lee, K. Y. C. Quantitative Analysis of Total Reflection X-ray Fluorescence from Finely Layered Structures Using XeRay. *Review of Scientific Instruments* **88**, 033112 (2017).

Zinn, S. R., **Slaw, B. R.**, Lettow, J. H., Menssen, R. J., Wright, J. H., Mormann, K., Ting, J. M. Lessons Learned from the Creation and Development of a Researcher-Led Safety Organization at The University of Chicago. *ACS Chem. Health Saf.* **27**, 114–124 (2020).

Chung, P. J., Hwang, H.L., **Slaw, B. R.**, Leong, A., Adams, E. J., Lee, K. Y. C. The C-Terminal Domain of α -Synuclein Confers Steric Stabilization on Synaptic Vesicle-Like Surfaces. *Advanced Materials Interfaces* **7**, 1902151 (2020).

Slaw, B.R. *et al.* The Impact of Membrane Defect Presentation on α -Synuclein Binding to Model Membranes. In preparation, 2022.

Section 1.7: References

- [1] Maroteaux, L., Campanelli, J. T. & Scheller, R. H. *J Neurosci* **8**, 2804–2815 (1988).
- [2] Uéda, K. *et al. Proc Natl Acad Sci USA* **90**, 11282 (1993).
- [3] Jakes, R., Spillantini, M. G. & Goedert, M. *FEBS Letters* **345**, 27–32 (1994).
- [4] Lavedan, C. *et al. Human Genetics* **103**, 106–112 (1998).
- [5] George, J. M. *Genome Biol* **3**, REVIEWS3002–REVIEWS3002 (2002).
- [6] Spillantini, M. G., Crowther, R. A., Jakes, R., Hasegawa, M. & Goedert, M. *Proc Natl Acad Sci USA* **95**, 6469 (1998).
- [7] Spillantini, M. G. *et al. Neuroscience Letters* **251**, 205–208 (1998).
- [8] Spillantini, M. G. *et al. Nature* **388**, 839–840 (1997).
- [9] Fusco, G. *et al. Nature Communications* **5**, 3827 (2014).
- [10] Bodles, A. M., Guthrie, D. J. S., Greer, B. & Irvine, G. B. *Journal of Neurochemistry* **78**, 384–395 (2001).
- [11] Burré, J. *J Parkinsons Dis* **5**, 699–713 (2015).
- [12] Snead, D. & Eliezer, D. *Journal of Biological Chemistry* **294**, 3325–3342 (2019).
- [13] Meade, R. M., Fairlie, D. P. & Mason, J. M. *Molecular Neurodegeneration* **14**, 29 (2019).
- [14] Bernal-Conde, L. D. *et al. Frontiers in Neuroscience* **13**, 1399 (2020).
- [15] Goedert, M. *Nature Reviews Neuroscience* **2**, 492–501 (2001).
- [16] Kokhan, V. S., Afanasyeva, M. A. & Van'kin, G. I. *Behavioural Brain Research* **231**, 226–230 (2012).
- [17] Chandra, S. *et al. Proc Natl Acad Sci U S A* **101**, 14966 (2004).
- [18] Greten-Harrison, B. *et al. Proc Natl Acad Sci USA* **107**, 19573 (2010).
- [19] Anwar, S. *et al. J. Neurosci.* **31**, 7264 (2011).
- [20] Connor-Robson, N., Peters, O. M., Millership, S., Ninkina, N. & Buchman, V. L. *Neurobiol Aging* **46**, 107–112 (2016).

- [21] Nemani, V. M. *et al. Neuron* **65**, 66–79 (2010).
- [22] Larsen, K. E. *et al. J Neurosci* **26**, 11915–11922 (2006).
- [23] Cabin, D. E. *et al. J. Neurosci.* **22**, 8797 (2002).
- [24] Jahn, R. & Fasshauer, D. *Nature* **490**, 201–207 (2012).
- [25] Schoch, S. *et al. Science* **294**, 1117–1122 (2001).
- [26] Nickel, W. *et al. Proc Natl Acad Sci USA* **96**, 12571 (1999).
- [27] Kesavan, J., Borisovska, M. & Bruns, D. *Cell* **131**, 351–363 (2007).
- [28] Chanaday, N. L. & Kavalali, E. T. *eLife* **7**, e36097 (2018).
- [29] Chanaday, N. L., Cousin, M. A., Milosevic, I., Watanabe, S. & Morgan, J. R. *J. Neurosci.* **39**, 8209 (2019).
- [30] Denker, A. & Rizzoli, S. *Frontiers in Synaptic Neuroscience* **2**, 135 (2010).
- [31] Iwai, A. *et al. Neuron* **14**, 467–475 (1995).
- [32] Betzer, C. *et al. PLOS ONE* **10**, e0116473 (2015).
- [33] Hernandez, S. M., Tikhonova, E. B. & Karamyshev, A. L. *Frontiers in Aging Neuroscience* **12**, 72 (2020).
- [34] Lassen, L. B., Reimer, L., Ferreira, N., Betzer, C. & Jensen, P. H. *Brain Pathol* **26**, 389–397 (2016).
- [35] Nielsen, M. S., Vorum, H., Lindersson, E. & Jensen, P. H. *Journal of Biological Chemistry* **276**, 22680–22684 (2001).
- [36] Lowe, R., Pountney, D. L., Jensen, P. H., Gai, W. P. & Voelcker, N. H. *Protein Science* **13**, 3245–3252 (2004).
- [37] Natalello, A., Benetti, F., Doglia, S. M., Legname, G. & Grandori, R. *Proteins: Structure, Function, and Bioinformatics* **79**, 611–621 (2011).
- [38] Rasia, R. M. *et al. Proc Natl Acad Sci U S A* **102**, 4294 (2005).
- [39] Illes-Toth, E., Dalton, C. F. & Smith, D. P. *Journal of The American Society for Mass Spectrometry* **24**, 1346–1354 (2013).
- [40] Binolfi, A. *et al. J. Am. Chem. Soc.* **128**, 9893–9901 (2006).

- [41] Burré, J. *et al. Science* **329**, 1663 (2010).
- [42] Jarsch, I. K., Daste, F. & Gallop, J. L *J Cell Biol* **214**, 375–387 (2016).
- [43] Cooke, I. R. & Deserno, M. *Biophys J* **91**, 487–495 (2006).
- [44] Koldsø, H., Shorthouse, D., Hélie, J. & Sansom, M. S. P. *PLOS Computational Biology* **10**, e1003911 (2014).
- [45] Roux, A. *et al. The EMBO Journal* **24**, 1537–1545 (2005).
- [46] MacKinnon, R. *Science* **306**, 1304 (2004).
- [47] Miller, S. E. *et al. Developmental Cell* **33**, 163–175 (2015).
- [48] Hu, J. *et al. Cell* **138**, 549–561 (2009).
- [49] Jiang, Z., de Messieres, M. & Lee, J. C. *J. Am. Chem. Soc.* **135**, 15970–15973 (2013).
- [50] Hoover, B. M. *et al. J. Phys. Chem. B* **125**, 1582–1594 (2021).
- [51] Mim, C. *et al. Cell* **149**, 137–145 (2012).
- [52] Morén, B. *et al. MBoC* **23**, 1316–1329 (2012).
- [53] Day, C. A. *et al. Traffic* **16**, 572–590 (2015).
- [54] Peter, B. J. *et al. Science* **303**, 495 (2004).
- [55] Vanni, S., Hirose, H., Barelli, H., Antonny, B. & Gautier, R. *Nature Communications* **5**, 4916 (2014).
- [56] Risselada, H. J. & Marrink, S. J. *Phys. Chem. Chem. Phys.* **11**, 2056–2067 (2009).
- [57] Bigay, J., Casella, J.-F., Drin, G., Mesmin, B. & Antonny, B. *The EMBO Journal* **24**, 2244–2253 (2005).
- [58] Vanni, S. *et al. Biophysical Journal* **104**, 575–584 (2013).
- [59] Drin, G. *et al. Nature Structural & Molecular Biology* **14**, 138–146 (2007).
- [60] Giménez-Andrés, M., Čopič, A. & Antonny, B. *Biomolecules* **8**, 45 (2018).
- [61] González-Rubio, P., Gautier, R., Etchebest, C. & Fuchs, P. F. J. *Biochimica et Biophysica Acta (BBA) - Biomembranes* **1808**, 2119–2127 (2011).

- [62] Pranke, I. M. *et al.* *J Cell Biol* **194**, 89–103 (2011).
- [63] Antonny, B. *Annu. Rev. Biochem.* **80**, 101–123 (2011).
- [64] Middleton, E. R. & Rhoades, E. *Biophysical Journal* **99**, 2279–2288 (2010).
- [65] Yang, J. A. *et al.* *Langmuir* **29**, 4603–4615 (2013).
- [66] Budzinski, K. L. *et al.* *Biophysical Journal* **97**, 2577–2584 (2009).
- [67] Pirc, K. & Ulrih, N. P. *Biochimica et Biophysica Acta (BBA) - Biomembranes* **1848**, 2002–2012 (2015).
- [68] Kjaer, L., Giehm, L., Heimburg, T. & Otzen, D. *Biophys J* **96**, 2857–2870 (2009).
- [69] O’Leary, E. I., Jiang, Z., Strub, M.-P. & Lee, J. C. *Journal of Biological Chemistry* **293**, 11195–11205 (2018).
- [70] Man, W. K. *et al.* *Nature Communications* **12**, 927 (2021).
- [71] Hannestad, J. K. *et al.* *Proc Natl Acad Sci USA* **117**, 14178 (2020).
- [72] Vamparys, L. *et al.* *Biophysical Journal* **104**, 585–593 (2013).
- [73] Harayama, T. & Riezman, H. *Nature Reviews Molecular Cell Biology* **19**, 281–296 (2018).
- [74] Bussell, R. & Eliezer, D. *Journal of Molecular Biology* **329**, 763–778 (2003).
- [75] Jao, C. C., Der-Sarkissian, A., Chen, J. & Langen, R. *Proc Natl Acad Sci U S A* **101**, 8331 (2004).
- [76] Chandra, S., Chen, X., Rizo, J., Jahn, R. & Südhof, T. C. *Journal of Biological Chemistry* **278**, 15313–15318 (2003).
- [77] Borbat, P., Ramlall, T. F., Freed, J. H. & Eliezer, D. *J. Am. Chem. Soc.* **128**, 10004–10005 (2006).
- [78] Georgieva, E. R., Ramlall, T. F., Borbat, P. P., Freed, J. H. & Eliezer, D. *Journal of Biological Chemistry* **285**, 28261–28274 (2010).
- [79] Eliezer, D. Chapter 42 - Protein Folding and Aggregation in in vitro Models of Parkinson’s Disease: Structure and Function of α -Synuclein. in *Parkinson’s Disease* (eds. Nass, R. & Przedborski, S.) 575–595 (Academic Press, 2008). doi:[10.1016/B978-0-12-374028-1.00042-7](https://doi.org/10.1016/B978-0-12-374028-1.00042-7).

- [80] Soper, J. H. *et al. MBoC* **19**, 1093–1103 (2008).
- [81] Diao, J. *et al. eLife* **2**, e00592 (2013).
- [82] Milovanovic, D., Wu, Y., Bian, X. & De Camilli, P. *Science* **361**, 604 (2018).
- [83] Atias, M. *et al. Proc Natl Acad Sci USA* **116**, 11116 (2019).
- [84] Hoffmann, C. *et al. Journal of Molecular Biology* 166961 (2021).
- [85] The UniProt Consortium. *Nucleic Acids Research* **49**, D480–D489 (2021).
- [86] Georgieva, E. R., Ramlall, T. F., Borbat, P. P., Freed, J. H. & Eliezer, D. *J. Am. Chem. Soc.* **130**, 12856–12857 (2008).
- [87] Ulmer, T. S., Bax, A., Cole, N. B. & Nussbaum, R. L. *Journal of Biological Chemistry* **280**, 9595–9603 (2005).
- [88] Ramezani, M. *et al. npj Parkinson's Disease* **5**, 12 (2019).
- [89] Cui, H., Lyman, E. & Voth, G. A. *Biophysical Journal* **100**, 1271–1279 (2011).

CHAPTER 2.

DEVELOPMENT OF A NOVEL CONFOCAL BINDING ASSAY TO QUANTITATIVELY MEASURE PROTEIN/VESICLE BINDING

Section 2.1: Overview

Biophysical characterization of protein/lipid binding has been of great interest to scientific researchers for decades as evidenced by the wide variety of assays and techniques reported in scientific literature. Broadly speaking, the experimental setup being used for such characterizations can be classified as either solution- or surface-based. Solution-based techniques, such as liposome sedimentation assays and isothermal titration calorimetry, can be powerful tools to elucidate ensemble protein binding behavior, but such methods also have unique limitations. Liposome sedimentation assays, for example, can be very useful for determining *if* a protein of interest binds to lipid vesicles, but extraction of quantitative binding data proves difficult if not impossible due to the non-equilibrium conditions resulting from ultracentrifugation and resuspension [1, 2]. Conversely, isothermal titration calorimetry can provide much more quantitative information but has inherently low sensitivity and requires comparatively large amounts of protein [3]. Often, binding characterization studies elect to present data from several solution-based methods in aggregate as a means of circumventing the limitations of any individual technique [4], but all such techniques are limited to reporting on average protein behavior as opposed to an individual binding mechanism.

In contrast to solution-based techniques, surface-based techniques tend to offer much better sensitivity at the cost of less physiological relevance or more complex sample preparation. For example, atomic force microscopy (AFM) has often been used to explore how lipid-binding

proteins and peptides alter membrane organization and packing on a molecular level [5, 6], but these experiments are typically performed on a planar supported lipid bilayer with fewer degrees of freedom than their vesicular counterparts. Surface plasmon resonance (SPR), while capable of measuring protein adsorption in the sub-nanomolar range, requires delicate surface preparation before sensors can be used for biological measurements [7, 8]. Additionally, SPR suffers from the same limitation as AFM, where only supported lipid bilayers can be used. Though these methods and more boast label-free measurements (i.e. no further modification of the protein or substrate of interest is required), their inability to examine vesicular systems limits their applicability in elucidating physiologically relevant protein/lipid interactions.

In recent years, surface-based techniques have been continually adapted and redesigned to allow researchers to study more physiologically-relevant vesicular systems. One particularly versatile example is the emergence of surface-tethered vesicle fluorescence experiments, which typically involve immobilizing vesicles using the functionally irreversible interaction of biotin and streptavidin [9]. Such fluorescence-focused techniques offer greater flexibility for researchers in part due to the existing prevalence of instrumentation and wide variety of fluorophores commercially available. This flexibility is clearly evidenced by the large body of literature featuring adaptations to the original biotin/streptavidin immobilization platform; Berquand et al. used biotin/streptavidin coupling to immobilize fluorescently-tagged small unilamellar vesicles (SUVs) before triggering the formation of a free-floating supported lipid bilayer (SLB) [10]; Sarmiento et al. explored the effect of surface tethering on lipid domain reorganization using giant unilamellar vesicles doped with two different fluorophores [11]; Kuhn et al. expanded the technique to allow for immobilization of more complex assemblies, like fluorescently-tagged virus

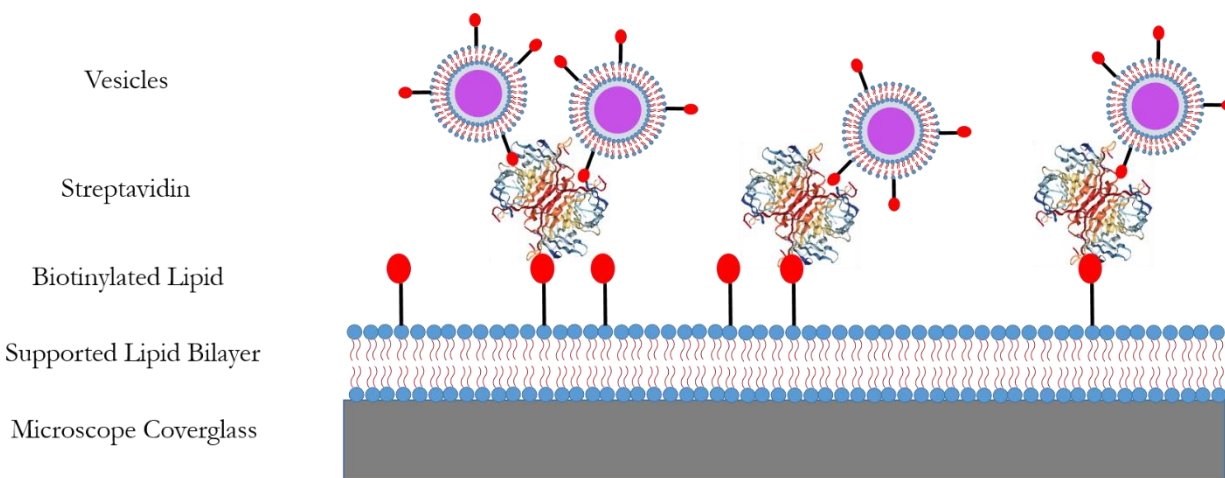


Figure 2.1: Cartoon of the vesicle immobilization scheme utilized in the confocal assay. Pictured above is a cartoon schematic of immobilized vesicles used in this assay. Samples are prepared layer by layer from the bottom up; we first create a supported lipid bilayer with trace amounts of biotinylated lipid on a cleaned glass coverslip, then sequentially add streptavidin followed by vesicles of interest doped with a similar amount of biotinylated lipid as the SLB. The end result is the “sandwich” complex above, where a single streptavidin acts as a linker or the “meat” between the biotinylated SLB and target vesicles, or “bread.”

particles and yeast cells [12]. Though these are only a few examples of new immobilization experiments that have emerged for studying vesicles, they clearly demonstrate the versatility and sensitivity that such fluorescence-based techniques can offer.

To further emphasize the versatility and sensitivity of fluorescent surface-based immobilization techniques, I have developed an assay which uses confocal microscopy to directly observe the association of fluorescently-tagged proteins and immobilized vesicles under dilute conditions. In this assay, vesicles of interest are immobilized *via* the formation of a biotin/streptavidin sandwich complex before titrating in known amounts of protein (figure 2.1). Protein binding is then directly observed and measured by identifying colocalization events, or locations in an image where protein and vesicle fluorescence overlap. Since it is well characterized that the fluorescent intensity of a tagged vesicle scales according to its size [13], extruded vesicles with a tight polydispersity can be used as an internal reference for determining the relative amount

of bound protein. By determining the relative protein fluorescence over many colocalization events and titrating in different amounts of protein, I can create a binding curve and extract equilibrium dissociation constants for any protein/vesicle system of interest. In this chapter, I will describe protocols for creating surface-immobilized vesicles, robust confocal microscopy imaging, and data analysis using the publicly-available package cmeanalysis. Additionally, I will present a brief case study as a proof-of-principle examining the association of annexin and phosphatidylserine-containing vesicles. Further experiments performed involving this assay will be described in chapter 3.

Section 2.2: Methods

Section 2.2.1: Confocal Microscopy

Confocal microscopy was first conceived of and patented in the late 1950's by Marvin Minsky [14]. In comparison to traditional bright-field measurements, confocal microscopy offers both a much better signal-to-noise ratio in low-intensity environments as well as increased optical resolution in the z-direction; this is achieved by several changes in the configuration of the optical path (figure 2.2). In bright-field microscopy, the optics are configured such that the entire observable area of the sample is uniformly and simultaneously illuminated, resulting in an image that contains both features of interest as well as a large amount of unwanted background light. Confocal microscopy differs from bright-field in that confocal (1) introduces a pinhole filter in the optical path, (2) only illuminates a single point within the sample at a time, (3) generates an image pixel-by-pixel using an extremely fast "raster scanning" technique, and (4) typically relies on high-

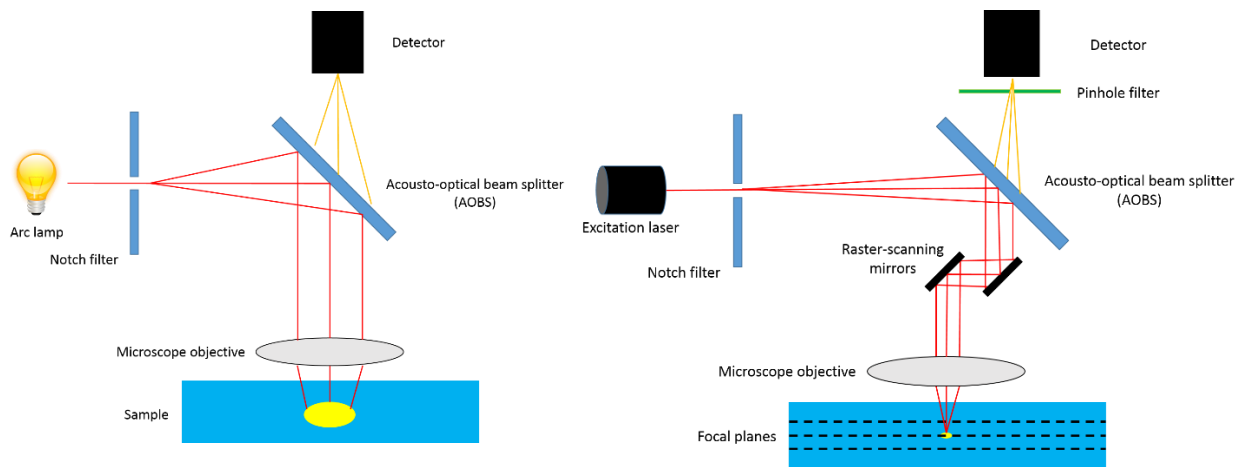


Figure 2.2: Diagrammatic comparison of brightfield and confocal microscopy. (Left): Simplified optical path of a typical brightfield microscope. An elemental arc lamp is used to generate excitation light of a fixed wavelength. Excess light is removed from the optical path using a notch filter, which permits only the desired excitation wavelength to pass through. An acousto-optical beam splitter (AOBS) or dichroic mirror directs the excitation light through the microscope objective onto the sample, where a relatively large field is uniformly illuminated. Light emitted from the sample passes back through the AOBS to eventually reach the detector. **(Right):** Simplified optical path of the confocal microscope used in this work. In contrast to the brightfield example, a highly-collimated supercontinuum white light laser is used generate excitation light with any wavelength between 470 and 670 nm, inclusive. Generated light passes through an optional notch filter, which can narrow the spectral bandwidth to minimize noise. An AOBS then directs light to a series of raster-scanning mirrors, which rotate at high frequencies to quickly generate an image from individually excited points within the sample. Light emitted from the sample passes back through the AOBS before a pinhole filter is used to stop out-of-focus light from the reaching the detector. The resulting image represents a small optical section, or z-slice, of the sample.

intensity lasers for excitation as opposed to a broad-spectrum source. The rationale for each of these changes will be explained in the upcoming paragraphs.

The introduction of a pinhole filter into the optical path of a microscope effectively removes any out-of-focus background light from the collected image. To better understand why this is the case, it is helpful to consider a simplified optical path involving two lenses as opposed to the single lens found in traditional bright-field microscopy (figure 2.3). The addition of a second lens into the optical path allows us to spatially separate the emission from a focal point of interest

(figure 2.3, red paths) from any background emission emanating from the surrounding optical cone (figure 2.3, orange paths). The unwanted background emission can subsequently be removed by inserting an opaque screen with a pinhole aperture behind the second lens; thus, only emitted light from the focal point of the first lens will be allowed to reach the detector. As a result of this configuration, only one point within a sample can be illuminated and observed at a time; in order to generate a full image involving many points, the incident beam must be scanned over an area of interest in a rectangular raster. This is typically accomplished by a series of mirrors rotating at very high frequencies, as represented in figure 2.2. With modern technology, the rotational frequencies of these mirrors can reach up to 8000 Hz, which would produce a complete 512 x 512 pixel image in under a second. Therefore, even though a complete confocal image must be assembled point by point, this method can be just as fast (if not faster) as collecting images on a traditional bright-field microscope.

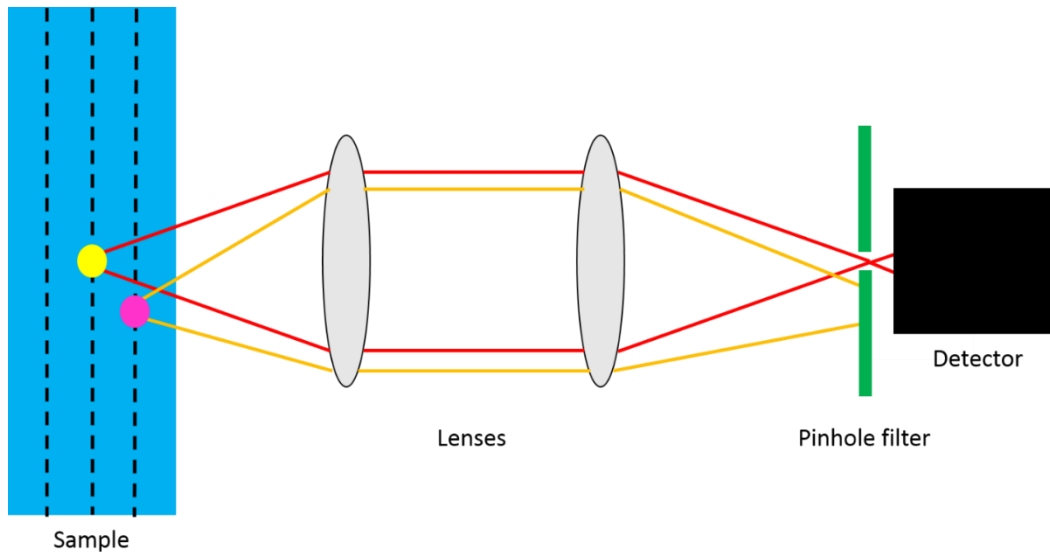


Figure 2.3: Two lenses in a simplified optical path demonstrate how a pinhole works in confocal microscopy. In this simplified optical path, a pinhole filter is placed in front of the detector to prevent out-of-focus light from being detected. Light emitted from the yellow circle, representing the in-focus optical section of the sample, passes through two lenses before being re-focused into the gap in the pinhole filter and reaching the detector (red paths). Light emitted from the pink circle, representing out-of-focus emission, passes through the same two lenses and eventually gets re-focused into a different spot where there is no gap in the pinhole filter (orange paths). Adapted from [18].

As mentioned previously, a pinhole filter effectively prevents out-of-focus light from reaching the detector; while beneficial for increasing the optical contrast of a point of interest, this configuration also results in very little observable signal. To account for this reduction in signal, modern microscopes typically use laser light as an excitation source and either a photomultiplier tube (PMT) or avalanche photodiode (APD) as a detector. In comparison to broad-spectrum light sources, lasers produce far more radiant intensity and are generally much better behaved. When used in concert with a PMT or APD, which effectively amplifies weak photon signals, a microscope can generate enough fluorescence emission to produce a high-quality image.

While the use of a pinhole filter is extremely effective at reducing background light detection, it introduces another phenomenon to consider when analyzing data: diffraction. Diffraction results from light passing through an aperture of any size, and for a single-point source manifests as a series of concentric light and dark rings surrounding a brighter central disk, as shown in figure 2.4; the central disk and surrounding rings are often referred to as the Airy disk and Airy pattern, respectively, after George Biddell Airy, who first formally characterized the phenomenon in 1835 [15]. The size of the central Airy disk in the xy-plane is related to both the wavelength of light (λ) used for excitation as well as the numerical aperture (NA) of the microscope objective; this relationship was first discussed by Ernst Abbe in the context of defining the minimum resolvable distance between two points, and was calculated for a given system using the following formula,

$$Distance = \frac{\lambda}{2NA} = \frac{\lambda}{2n \sin \theta}$$

where n is the refractive index of the imaging medium and θ is the maximal half-angle over which the objective can collect light [16]. This simple relationship provides insight into how to increase the resolution of a system (e.g., decreasing the incident wavelength, increasing the numerical aperture), but also demonstrates that there is a fundamental limit to how small the Airy disk can get for a given optical configuration, even if the source of the signal is much, much smaller. Thus, experiments aiming to observe objects smaller than the smallest achievable Airy disk are said to be “diffraction limited.”

Diffraction-limited experiments offer their own unique set of challenges. When trying to observe an object much smaller than the Airy disk, one needs to consider the resolution limit, or

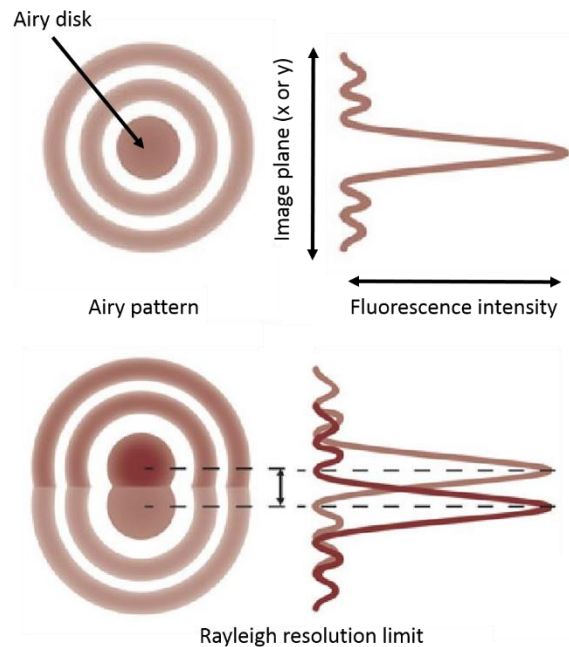


Figure 2.4: Diffraction-limited signals produce individual Airy patterns which need to be resolved for sub-pixel localization. (Top): As a result of diffraction a point emitter would produce an Airy pattern, or a series of concentric rings surrounding a large central disk, after passing through an aperture. The intensity profile of an Airy pattern shows that most of the intensity is contained in the central disk, called the Airy disk. **(Bottom):** Representation of the Rayleigh resolution limit, where the center of one Airy disk aligns with the first minimum of its neighbor’s pattern. The Rayleigh resolution limit represents one of many accepted measures for resolvable signals. Adapted from [18].

minimum observable separation between two such objects. Though many different measures exist for determining whether a set of signals is resolved (such as the aforementioned Abbe resolution limit), the most common one used for optical microscopy is the Rayleigh criterion [17]. The Rayleigh criterion, named for John William Strutt, 3rd Baron Rayleigh, defines the lateral resolution limit of two point emitters as the distance where the maximum of the Airy disk of one emitter is directly overlapping the first minimum of the Airy pattern of another emitter (figure 2.4). Mathematically, this distance can be represented as,

$$\textit{Rayleigh Resolution Limit} = \frac{0.61\lambda}{NA} = \frac{0.61\lambda}{n \sin \theta}$$

where λ is the wavelength of incident light, NA is the numerical aperture of the lens, n is the refractive index of the imaging medium, and θ is the maximal half-angle over which the objective can collect light [19]. Although Rayleigh himself admitted that this definition is somewhat arbitrary and based on the abilities of the human eye, it has nonetheless become a standard criterion used within the microscopy community.

In addition to limitations on the achievable resolution limit, and particularly when attempting to observe diffraction-limited phenomena, one must also consider the impact of the microscope optics on the images collected. Until this point, I have been making the implicit assumption that the microscope objective is perfect (i.e., without aberrations) and capable of focusing light into an infinitesimally small point; under these assumptions and with a sufficiently small pinhole, a point-emitter will produce the aforementioned Airy pattern in an image. However, depending on the optical setup of the microscope being used these assumptions may not be

completely valid. If some small abnormality exists in the microscope optics, it will systematically impact all of the signals that pass through them and effectively blur or smear the Airy patterns in the resulting image. While undesirable, this effect is unavoidable given current limitations in manufacturing lenses and other optical components; as such, rather than trying to eliminate the phenomenon, many experimentalists find it helpful to measure a point spread function (PSF), which is a function describing how the signal from a point-emitter is blurred after passing through a given optical setup [20]. Mathematically, since the point spread function impacts all signals observed by a detector, a given image can be considered a convolution of the objects of interest and the microscope PSF, as shown in figure 2.5. As a result of this relationship, it is therefore also possible in post-collection analysis to deconvolute the PSF from a dataset to achieve sub-diffraction resolution, provided an experimentalist has a measured PSF in hand. While such deconvolution methods can be used as powerful tools for sub-diffraction-limited studies, the details of these methods lie outside the purview of this thesis; for more information, the reader is directed to any number of articles written on the subject [22-25].

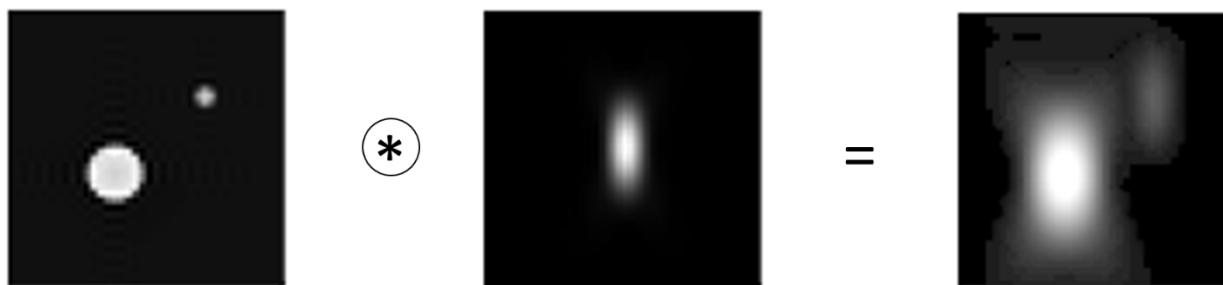


Figure 2.5: Impact of the microscope point spread function (PSF) on collected images. The point spread function (PSF) is a function which describes the impact of the microscope optics on the light traveling through them. Since the PSF impacts all images obtained by the microscope, any obtained image will mathematically be a convolution of the fluorescent objects of interest and the PSF. While unavoidable, many techniques and analyses are reported in the literature for measuring and deconvoluting the PSF from the original objects. Adapted from [21].

Section 2.2.2: Preparation of small unilamellar vesicles (SUVs) *via* freeze-thaw extrusion

All small unilamellar vesicles (SUVs) used in this work were prepared via a conventional freeze-thaw extrusion method. Purified lipid powders were first solubilized in high-purity chloroform before being mixed to produce the desired vesicle composition. Upon mixing, the resulting solution was rapidly dried under a stream of ultra-high purity nitrogen gas and placed in a vacuum desiccator for at least an hour to evaporate off any residual solvent. The lipid mixture was subsequently rehydrated in 1x HEPES-buffered saline (HBS, 150 mM NaCl, 10 mM HEPES, pH 7.2) while being gently vortexed at 37 °C for 45 minutes to produce an aqueous solution of multilamellar vesicles. After vortexing, the solution was subjected to five freeze-thaw cycles to produce unilamellar vesicles by alternatively submerging the sample in a dry ice/denatured ethanol bath and a 45 °C water bath. The resulting vesicles, while unilamellar, are incredibly polydisperse; to reduce the polydispersity, vesicle samples were first extruded twice through two 200 nm track-etched membranes at 50 psi Ar using a Lipex extruder (Evonik Transferra Nanosciences, Burnaby, BC, Canada) before being extruded 15 more times through two 50 nm track-etched membranes at 250 psi Ar. The polydispersity of the resulting solution was then measured via dynamic light scattering (DLS) on a Malvern Zetasizer (Malvern, UK). Extruded samples were stored at 4 °C and used within two weeks after preparation.

Section 2.2.3: Preparation of microscope slides and samples for protein binding assay

For microscopy experiments, coverslips (#1, Fisherbrand) were gently scrubbed with a Milli-Q-water-saturated Kimwipe and subjected to three consecutive rinses with denatured ethanol, water, and denatured ethanol. Separately, a matching number of Pyrex cloning cylinders (Corning Life Sciences, Nuevo Leon, Mexico) were given three consecutive rinses with denatured

ethanol, water, and denatured ethanol before being allowed to dry under a loosely-covering Kimwipe. Rinsed coverslips were similarly allowed to air dry under a loosely-covering Kimwipe for about half an hour before then being placed in a UV/Ozone cleaner (Model 342A, Jelight Company Inc., Irvine, CA) for approximately 15 minutes to remove any residual organic contaminants. Once cleaned, a Pyrex cloning cylinder was affixed to each coverslip using clear nail polish (Electron Microscopy Sciences) to produce a usable sample chamber (figure 2.6).

After allowing the nail polish to dry for ~15 seconds, buffer was immediately added to the sample chamber to prevent contaminants in the air from settling on the freshly-cleaned surface. A supported lipid bilayer (SLB) vesicle stock consisting of 99.5 mol% 1,2-dioleoyl-*sn*-glycero-3-

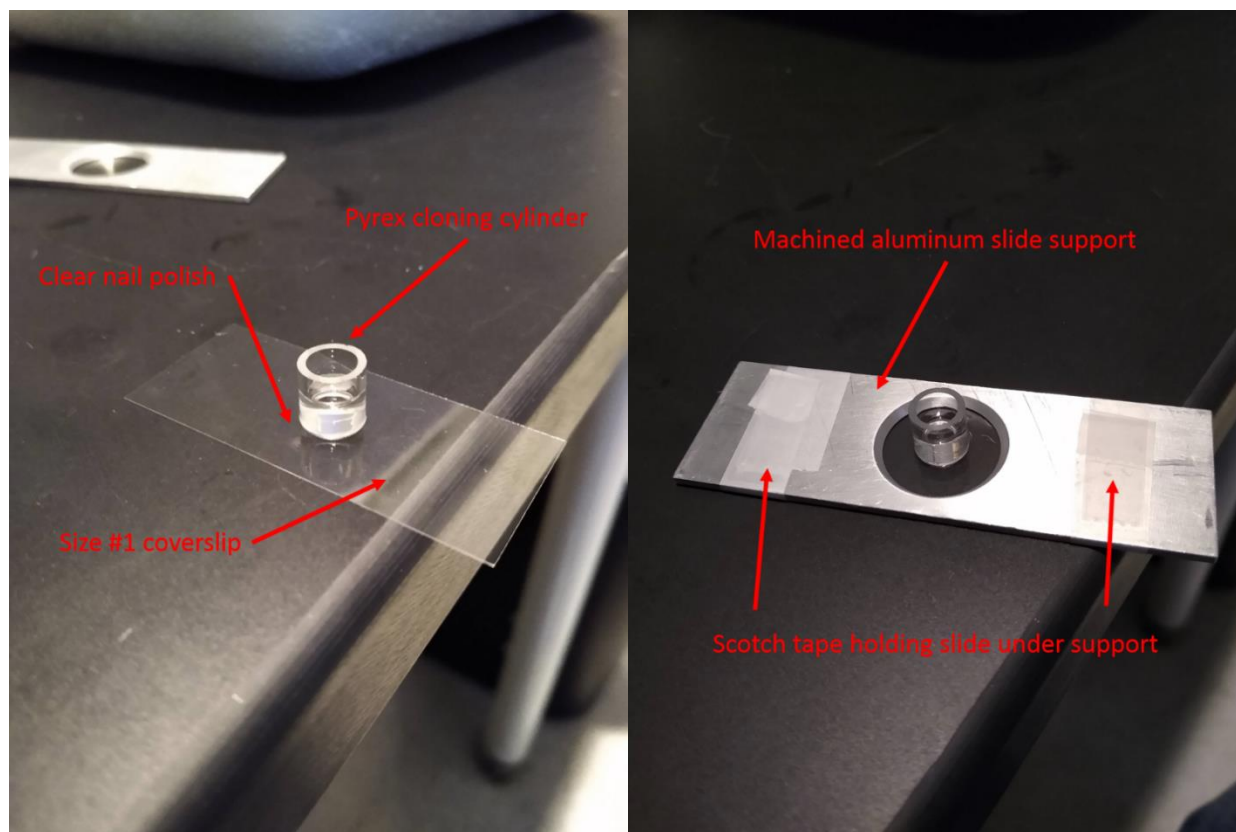


Figure 2.6: Sample chamber used in the confocal binding assay. (Left): To create the sample chamber pictured above, an 8 mm-diameter Pyrex cloning cylinder was affixed to a cleaned microscope coverslip with clear nail polish. **(Right):** When imaging, a prepared sample is affixed to a machined aluminum support to reinforce the coverslip and prevent it from breaking.

phosphocholine (DOPC) and 0.5 mol% 18:1 biotinyl cap phosphoethanolamine (PE) was then added to the sample chamber to a final concentration of 0.2 mM lipid and allowed to incubate for 30 minutes to allow an SLB to form. After 30 minutes, the sample chamber was thoroughly rinsed twice with fresh HBS and replaced with an ~40 nM streptavidin solution, which was allowed to bind to the biotinylated lipid in the SLB for approximately 15 minutes. Once bound, excess streptavidin was removed from the sample chamber by thoroughly rinsing twice with HBS and replacing the sample volume with a solution of the vesicles of interest to a final concentration of roughly 1 μ M. The solution was then incubated for 15 minutes to allow vesicles to bind to the SLB-immobilized streptavidin; a cartoon of the final streptavidin sandwich complex is shown in figure 2.1.

Upon completion of the last incubation, excess vesicles were removed from the sample chamber by thoroughly rinsing twice with HBS and replacing the sample volume with a solution containing the protein of interest. The sample was then allowed to equilibrate at room temperature for a minimum of 30 minutes before imaging. All imaging was completed within one hour after the protein equilibration to ensure stability in observed protein fluorescence. All incubations were done at room temperature, and samples were stored in a dark box while not being imaged.

Section 2.2.4: Instrumental settings and image collection protocol

Images were captured with a Leica SP8 3D STED laser scanning confocal microscope (Leica Microsystems, Inc., Buffalo Grove, IL) outfitted with a supercontinuum white light laser (WLL) and both standard hybrid GaAsP/PMT (standard HyD) as well as chilled, single-molecule sensitive hybrid GaAsP/PMT (SMD-HyD) detectors. To ensure uniformity and replicability between

experiments, an imaging sequence protocol was created to allow optimized parameters to easily be loaded into the system. The imaging sequence protocol loads in both the number of scans to capture as well as the following parameters for each individual scan:

- *Excitation laser:* With the aforementioned supercontinuum WLL, each scan can have its own unique excitation wavelength (between 470 and 670 nm) and intensity with minimal change in the optical path of the microscope.
- *Emission window:* The microscope software allows the acceptable emission window to be tailored for each laser line and detector within a scan. Both standard and SMD-HyD detectors also have the ability to impose time gating on the observed signal (e.g., with time gating active one could filter out any emitted light observed by the detector some time t after the excitation laser pulse). Time gating can be useful to differentiate fluorophores with overlapping excitation/emission behavior, as well as to minimize noise from errant scattered light. The gain setting for each detector used is also included in the imaging sequence protocol.
- *Averaging and accumulation:* To optimize signal collection, the software allows the user to average and/or accumulate multiple scans to produce an image. The result is exactly what it sounds like; with increased averaging, each pixel in the resulting image will be an average of the corresponding pixels in n scans (where n is the number of scans). With increased accumulation, each pixel in the resulting image will be the sum of the corresponding pixels from n scans. In practice, averaging is typically used to minimize signals from a sample that are not fixed (e.g. solubilized fluorophores) while accumulation is used to boost fixed signals that are very dim or have low emission. Averaging and

accumulation can be applied on a line-by-line basis, a frame-by-frame basis, or both as necessary.

- *Pinhole size:* The size of the pinhole filter, in either natural or Airy units, can be individually chosen for each scan and stored in the imaging sequence protocol. For all measurements conducted with this assay, a pinhole size of 0.5 Airy units was used, which corresponds to an optical section or z-slice of roughly 0.6 μm depending on the excitation wavelength used.

In addition, the microscopy software requires the user to specify the following parameters on startup (i.e., these parameters are not stored in the imaging sequence protocol):

- *Image bit depth:* Images are collected in grayscale and can be acquired in 8-, 12-, or 16-bit formats. The bit depth corresponds to the range of possible intensities that an individual pixel can display; for example, the pixels in an 8-bit image can store intensities between 0 and 256 grays, whereas in a 16-bit image a pixel can store intensities between 0 and 65,536 grays. All images collected using this assay were 16-bit format to allow for a broad range of interpretable and analyzable signals.
- *Image size:* The image size can range anywhere from 256 x 256 pixels to 2048 x 2048 pixels. All images collected and analyzed using this methodology were 2048 x 2048 pixels to maximize the spatial resolution of diffraction-limited spots.
- *Objective and zoom factor:* The microscope is outfitted with objectives ranging from 10x-100x magnification, with an optional artificial zoom factor available. The zoom factor is artificial because it is achieved by attenuating the rotational distance of the raster-scanning

mirrors as opposed to otherwise modifying the optical path. For all experiments conducted using this assay, a 63x/1.4 NA oil immersion objective was used in conjunction with a 4x zoom factor, resulting in 252x total magnification.

For all experiments conducted using this methodology a total of four scans were collected to create each image, where three scans were of the vesicle fluorophore at different time points and one scan was of the protein fluorophore (the rationale for this will be discussed in further detail in section 2.2.5). These four scans were then saved as individual frames in a four-dimensional hyperstack, which could easily be opened and converted into different file types suitable for analysis with ImageJ. A total of five images consisting of four scans each were collected for each sample, and the microscope objective was moved a significant distance between each image to ensure minimal photobleaching. The five images captured for each sample are saved as a single .lif file for ease of transfer to other machines.

It should also be noted that, due to the small size of the vesicle sample (~50 nm) compared to the observable optical section (~600 nm), a special focusing protocol had to be created to allow for efficient data collection. Briefly, this consisted of (1) course-grained focusing of the objective in a similar fashion to other microscopy experiments using the eyepieces in xyzt scan mode, followed by (2) changing the scan mode to xzyt and setting the acousto-optical beam splitter (AOBS) to “reflection” instead of “fluorescence,” and (3) adjusting the z-position until the reflection of the sample coverslip is in the field of view. The microscope can then be switched back into xyzt scan mode while maintaining the correct z-position.

Section 2.2.5: Image analysis

Signal detection and intensity fitting of confocal microscopy images were carried out using cmeanalysis, a MATLAB-based software package developed by the Danuser lab at UT Southwestern Medical Center [26]. Originally designed to identify the association of endocytic accessory proteins and clathrin-coated pits, cmeanalysis uses a robust statistical analysis algorithm to detect and mathematically fit the intensities of different fluorophores within a microscopy image or movie. Compared to similar software packages, cmeanalysis offers a variety of benefits that are ideal for studying protein/vesicle association, such as increased sensitivity under low signal-to-noise conditions and better selectivity for what constitutes a signal of interest. Additionally, implementation in the MATLAB environment affords the user added flexibility for both incorporating cmeanalysis into other analysis protocols and modifying the program to fit the needs of different experiments.

The analysis workflow used to process confocal microscopy data can be described as occurring in three broad steps. First, the user must organize the data into a format that cmeanalysis can recognize. For the purposes of these experiments, this involves using Fiji, a free open-source platform designed for processing biological microscopy images, to open the aforementioned .lif files and saving each image's hyperstack as an individual file in .tif format [27]. Note that each set of five images representing one sample should be saved in its own directory to avoid confusion and mishandling data. The user should then run the MATLAB script "prepareDataForAnalysis.m," which effectively just separates each image hyperstack into its four component scans and saves them in a particular file structure that cmeanalysis can easily navigate. For the reader's reference, this script is reproduced in appendix 2.1.

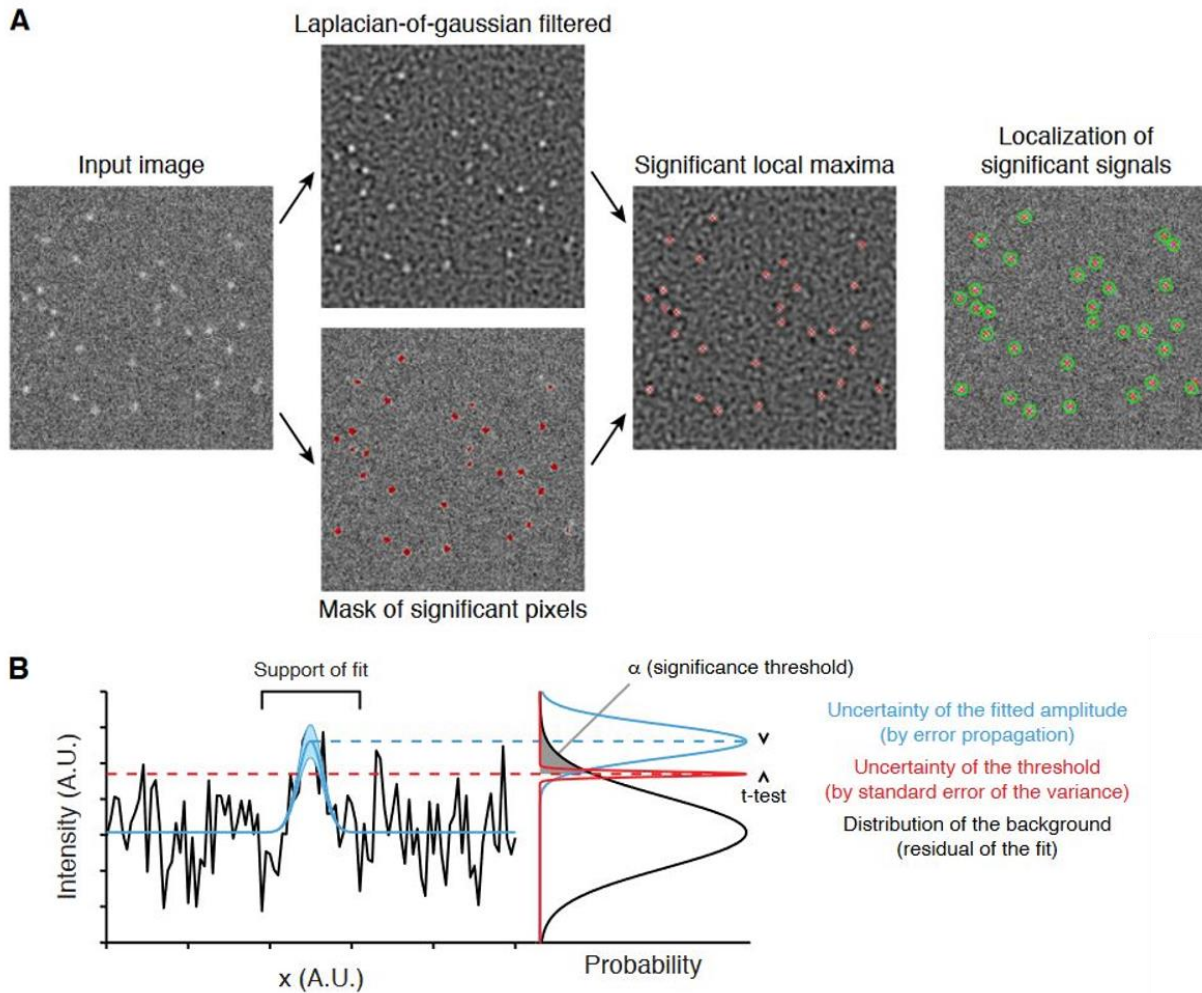


Figure 2.7: Spot detection and significance testing employed by cmeanalysis. (A) Example of cmeanalysis’ spot detection algorithm working on simulated data. First, a mask of significant pixels is generated by iteratively fitting a Gaussian to each pixel in an input image. This mask is compared to a Laplacian-of-Gaussian-filtered version of the same input image, and areas of overlap between the two are considered potentially significant and worthy of further analysis. (B) Sample significance testing applied to a 1-D cross section of a diffraction-limited signal. As described by Aguet et al., “A Gaussian function approximating the point-spread-function (PSF) of the microscope (blue) is fitted to the raw intensities (black), with amplitude, local background, and position as free parameters. The spread of the Gaussian approximation is defined by the PSF. Residuals of the fit yield the noise distribution and, by error propagation, the uncertainty on the fitted amplitude (blue shaded area). The amplitude is considered significant if it lies above a threshold value in the noise distribution, shown here for the 95th percentile. The uncertainty on this threshold is calculated from the standard error of the variance (red). Significance is determined with a one-tailed, two-sample t-test.” Adapted from [26].

With organized data in hand, the user can proceed on to the second phase of analysis, where the `cmeanalysis` package is used to detect and fit significant signals in each scan. The procedure used by `cmeanalysis` to process microscopy images can be described as follows. After reading a scan into memory, the program identifies statistically significant signals on a pixel-level basis by fitting a Gaussian to each individual pixel; this produces a first-pass estimate of both the signal amplitude and background which are used to create a pixel-level mask of potential signals of interest. Separately, candidate positions of signals of interest are determined by applying a Laplacian-of-Gaussian (LoG) filter to the same scan. A LoG filter is typically used for edge detection in microscopy analysis, and consists of taking the Laplacian (i.e., second derivative) of a Gaussian-blurred image; the Laplacian highlights regions of the image in which a rapid change of intensity occurs, and a Gaussian blur “pre-filter” is used to minimize the impact of normal background fluctuations and noise. Significant maxima in the LoG-filtered image are then compared to the aforementioned pixel-level mask, and locations where both images are found to have significant signals are considered candidates for further analysis (figure 2.7a).

Once candidate signal locations are identified, `cmeanalysis` runs a deconvolution algorithm to acquire sub-pixel localization and an amplitude estimate for each significant signal. As mentioned in the previous section, deconvolution aims to remove the microscope PSF, or the impact of a particular microscope’s optics, from the images it acquires. One powerful feature of `cmeanalysis` compared to similar packages is that it allows the user to run deconvolution without any knowledge of the specific microscope’s PSF. The program estimates the PSF either by (1) iteratively fitting a Gaussian to significant signals and selecting the most probable standard deviation found from the fit, or (2) calculating an expected PSF using a theoretical model, which

requires the numerical aperture, total magnification, and pixel size of the experimental setup as well as the wavelength of light being used as a probe. While the former methodology would likely yield a better estimate of the specific microscope PSF, it would also require a significant amount of computational resources and time; coupled with the fact that this fitting procedure often would fail due to low significant signal, I opted to use the second method for estimating my experimental PSF. Once a PSF estimate is obtained, it is used as the standard deviation of a Gaussian function to fit all candidate signals obtained from the overlay of the pixel-level mask and LoG-filtered image. This fitting step returns both the fitted amplitude of a signal and an estimation of the local background intensity.

With fitted amplitude and background measurements in hand, `cmeanalysis` then determines whether the fit candidate signals are considered significant. This is accomplished by performing a one-sided, two-sample t-test comparing the fit amplitude of the signal to the distribution of the surrounding noise; if the fit signal amplitude lies above a certain threshold defined by the user, it is considered significant (figure 2.7b). For all analysis reported here, significant signal was defined as any candidate intensity greater than the 95th percentile of the background noise distribution (i.e., I have defined significant signals as being the highest 5% of pixel intensities contained in an image). Information including the sub-pixel localization, amplitude, and local background for all candidate signals that satisfy this significance criterion are then saved to a MATLAB file that can be used for further analysis.

When `cmeanalysis` has completed fitting and significance testing on an image, the user can then proceed to the third phase of data analysis which involves determining (1) if significant

signals are colocalized (i.e., overlapping) between the different scans of an image, and (2) the relative intensity of the two fluorophore signals that constitute a positive colocalization event. To accomplish this, I have written a short MATLAB script that iteratively reads in the detection results from cmeanalysis and, if a significant signal was found in the same location across all four scans, extracts the fit amplitudes of the signals from the first vesicle scan and the protein scan (appendix 2.2). It should be noted that the second and third vesicle scans obtained are only used to determine whether the vesicles identified in the first scan are sufficiently immobilized; any vesicles in the first scan that do not appear in the same location in subsequent scans are thus excluded from analysis. For each positive colocalization identified, the script then calculates the relative intensity of the contributing signals by normalizing each protein signal by its corresponding vesicle signal. This process is repeated for all five images within a sample set, and all colocalization events across all images are averaged to produce a single value, which will be referred to as the mean relative intensity. Error in the mean relative intensity value is represented by the standard error of the mean. Iterating this process over many samples while titrating in different amounts of protein can thus be used to produce a binding curve like the one pictured in figure 2.8.

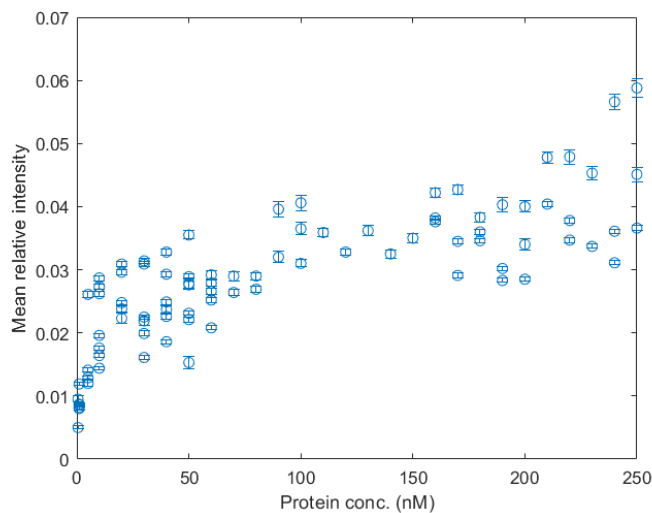


Figure 2.8: Sample binding curve obtained using the confocal assay. Each point in the plot above represents the average relative intensity (unitless) of all colocalization events identified in a sample. Error bars represent the standard error of the mean.

Section 2.2.6: Considerations for robust data collection

A great deal of work has gone into refining this assay and ensuring replicability between sample preps. In this section, I will briefly highlight some practical things to consider when trying to adapt this assay for new experiments.

- *Surface passivation:* For all reported experiments, surface passivation and biotinylation was achieved by creating a supported lipid bilayer (SLB) within the sample chamber. While a significant body of research exists examining how, why, and under what conditions SLBs form, there does not appear to be a uniform protocol for how to make them [28-30]. The protocol I eventually settled on here has been adapted from both published sources [31] and anecdotal protocols provided by peers. I have also tested surface passivation protocols involving deposition of a bovine serum albumin (BSA)/BSA-biotin mixture on a bare glass slide; while such methods have been shown to work previously, they turned out to not be suitable for my needs due to potential interactions with my proteins of interest. When adapting this assay for one's own experiments, care should be taken to ensure the surface is sufficiently passivated and the SLB does not impact measurements.
- *Dilution and homogenization:* In early iterations of this assay, I added concentrated vesicle and protein stock solutions directly to pre-measured buffer within the sample chamber. While this would occasionally yield decent samples, the number of surface-immobilized vesicles varied widely both within and between samples. After much trial and error, I found that pre-diluting and mixing solutions (via repeatedly pipetting half of the volume up and down) resulted in much better homogeneity. To illustrate this, the third phase of the analysis workflow (appendix 2.2) features a quick calculation to estimate the final bound

lipid concentration; while this concentration fluctuates between 13 and 18 nM, the standard deviation of the concentration is always 1 nM or less for all 10 samples prepared in one session.

Section 2.3: Case study: Using the confocal binding assay to observe annexin binding

To validate and further refine the confocal binding assay methodology and analysis, I first used this technique to measure the binding of fluorescently-tagged annexin-V to model synthetic vesicles. Annexin-V is a well-characterized member of the annexin family of proteins, which are ubiquitous and evolutionarily conserved in both plant and animal life. While the specific function and physiological localization of each annexin protein varies, all members of the family share a conserved structural motif of roughly 70 amino acids and have the capability to bind to negatively-charged phospholipids in a Ca^{2+} -dependent manner [32]. Originally isolated and identified in human placenta tissue, the binding of annexin-V to lipid membranes has been used as a platform for a number of biochemical assays and experiments, including a standardized method to detect different apoptotic cells and a tool to detect the progression and efficacy of cancer diagnoses and treatment [33-35]. Additionally, the impact of solubilized calcium ions on annexin-V's affinity for target membranes has been thoroughly explored through protein truncation, calcium titration, and point mutation experiments [36-38]. Although research into annexin-V's normal physiological behavior is ongoing, the breadth of published studies exploring its interaction with model vesicles makes it an excellent subject for validating a new technique.

In this section, I will describe the experiments I conducted using the confocal binding assay to measure the association of annexin-V to surface-immobilized vesicles. Annexin-V binding was explored for two different vesicle compositions: one containing 75 mol% DOPC, 0.5 mol% 18:1

biotinyl cap PE, 0.1 mol% Cy5-PE, and 25 mol% 1,2-dioleoyl-*sn*-glycero-3-phosphatidylserine (DOPS), which has been shown to be essential for annexin membrane binding, and one comprised of 99.4 mol% DOPC, 0.5 mol% biotinyl cap PE, and 0.1 mol% Cy5-PE, which serves as a negative control. All experiments presented here were performed under calcium-saturating conditions, where the bulk concentration of Ca^{2+} was 1 mM.

Section 2.3.1: Materials

All lipids were purchased as either dried powders (DOPC, DOPS, 18:1 biotinyl cap PE) or as a premixed chloroform solution (Cy5-PE) from Avanti Polar Lipids (Birmingham, AL). Three vesicle solutions were prepared for these assays, including an SLB mixture (99.95 mol% DOPC, 0.05 mol% 18:1 biotinyl cap PE), a PS-containing mixture (74.85 mol% DOPC, 25 mol% DOPS, 0.1 mol% Cy5-PE, 0.05 mol% 18:1 biotinyl cap PE), and a PS-lacking mixture (99.85 mol% DOPC, 0.1 mol% Cy5-PE, 0.05 mol% 18:1 biotinyl cap PE). All vesicles were prepared using the freeze-thaw-extrusion method previously discussed. Unless otherwise noted, vesicle solutions and sample manipulations were all done in HEPES-buffered saline (HBS, 10 mM HEPES, 150 mM NaCl, pH 7.2), and calcium (Spectrum Chemical, New Brunswick, NJ) was added to the sample chamber to a final concentration of 1 mM immediately before the addition of protein. Annexin-V fluorescently tagged with CF555 (AV-CF555) was purchased as a lyophilized powder from Biotium (Fremont, CA) and resuspended in HBS to a final concentration of 20 nM before use.

Section 2.3.2: Confocal microscope parameters

Images were captured with a Leica SP8 3D STED laser scanning confocal microscope (Leica Microsystems, Inc., Buffalo Grove, IL) outfitted with a 63x/1.4 NA objective and supercontinuum white light laser. Excitation of Cy5-tagged vesicles was accomplished using a laser line at 633 nm with 10% laser intensity, and emission was collected over the range of 660-720 nm. Excitation of CF555-tagged annexin was accomplished using a laser line at 555 nm with 10% laser intensity, and emission was collected over the range of 565-620 nm. Collected images were 2048 x 2048 pixels in size, and were obtained using a 400 Hz scan head speed corresponding to an optical dwell time of 0.591 ps. The confocal pinhole size used for all experiments was 0.5 Airy units in diameter.

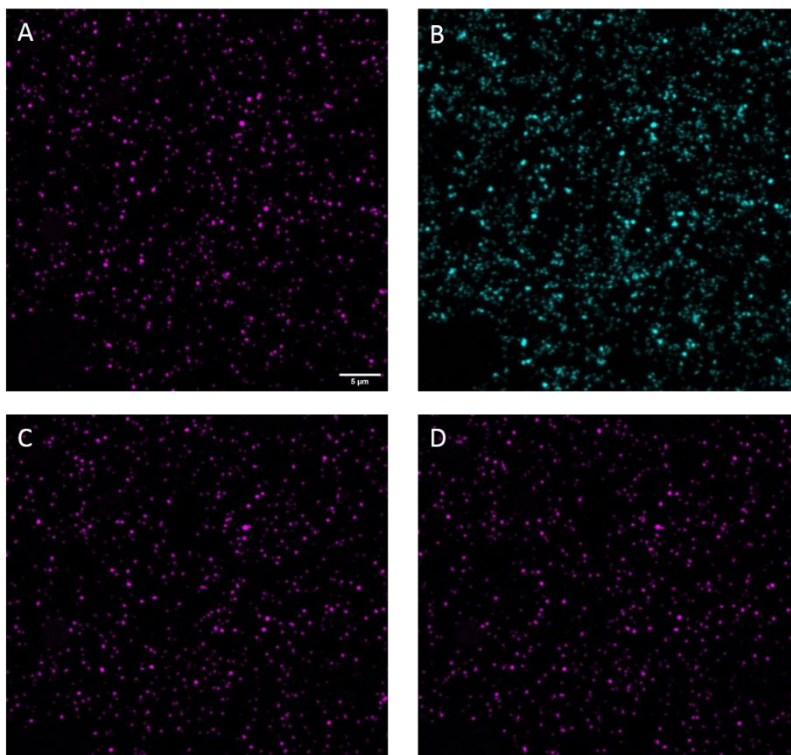


Figure 2.9: Sample images of annexin-V-CF555 binding obtained using the confocal assay. Pictured above are the four scans which comprise a single image obtained in the measurement of AV-CF555 binding to PS-containing vesicles. **(A)**: First scan of vesicles containing a small amount of Cy5-PE. **(B)**: Scan of the AV-CF555. **(C, D)**: Second and third vesicle scans, respectively, used to determine if vesicles are properly immobilized. All images have been contrast-enhanced with post-analysis look-up tables (LUTs) for visual clarity. The white scale bar represents 5 µm.

Section 2.3.3: Results

Sample images used for analysis are presented in figure 2.9. A total of 56 samples were analyzed with cmeanalysis to produce the binding curve between AV-CF555 and PS-containing vesicles shown in figure 2.10. To give a sense of scale, the data presented represent over 130,000 colocalization events identified from roughly 460,000 total vesicles observed across all samples. Robust fitting of the mean relative intensity data using a standard Hill model yields a dissociation constant of $K_d = 1.82$ nM and a Hill number of $n = 1.36$. Similar experiments were performed with AV-CF555 and PS-lacking vesicles, but none of these samples displayed significant binding and are therefore not shown.

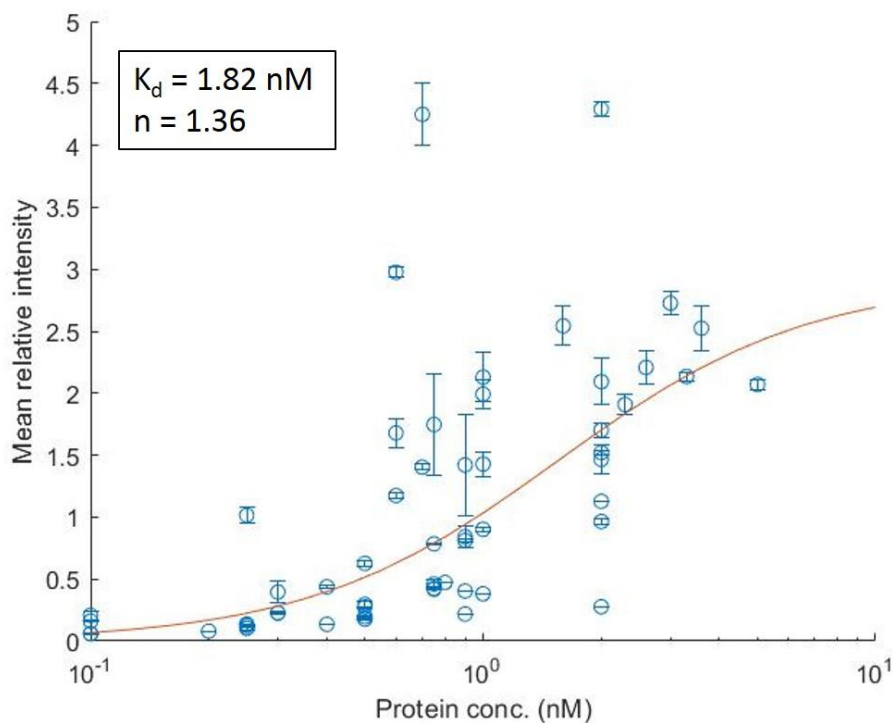


Figure 2.10: Annexin-V binding curve for 25 mol% DOPS vesicles obtained using the confocal fluorescence assay. Each blue circle on the plot above represents the mean relative intensity value calculated from a single sample. Error bars represent the standard error of the mean calculated for each sample. The red curve is the result of fitting a standard Hill model to the data, whose parameters are reproduced in the top left corner of the image.

Section 2.3.4: Discussion

Literature precedent reports that under calcium-saturating conditions, annexin-V should bind to vesicles presenting PS in the outer leaflet and that this binding appears cooperative with respect to both calcium and other annexin-V monomers [37, 39, 40]. As a result of this supposed cooperativity, I elected to use the standard Hill model,

$$\theta = b * \frac{[AV - CF555]^n}{K_d + [AV - CF555]^n}$$

to fit the mean relative intensity data, where θ is the bound fraction of protein, b is a scaling factor to account for the unitless mean relative intensity, K_d is the dissociation constant, and n is the Hill coefficient. Robust fitting using this model produced a Hill coefficient of $n = 1.36$, which agrees with the precedent that annexin-V displays some cooperativity with other annexin-V monomers despite differences in experimental setup. Additionally, the dissociation constant $K_d = 1.82$ nM agrees well with the value reported by Kapyt *et al.*, wherein the dissociation constant of annexin-V-FITC binding to immobilized PS headgroups was found to be 6.6 nM [41]. Coupled with the lack of colocalization events observed on PS-lacking vesicles, these data suggest that the experimental setup and analysis methods described here are valid and can be used to explore protein binding to any vesicle of interest.

Section 2.4: References

- [1] Senju, Y., Lappalainen, P. & Zhao, H. *Phosphoinositides: Methods and Protocols* (ed. Botelho, R. J.) 195–204 (Springer US, 2021). doi:[10.1007/978-1-0716-1142-5_14](https://doi.org/10.1007/978-1-0716-1142-5_14).
- [2] Gu, W. *et al. Nature Communications* **12**, 4718 (2021).
- [3] Hughes, E., Clayton, J. C. & Middleton, D. A. *Biochimica et Biophysica Acta (BBA) - Biomembranes* **1788**, 559–566 (2009).
- [4] Padmanarayana, M. *et al. Biochemistry* **53**, 5023–5033 (2014).
- [5] El Kirat, K., Dufrière, Y. F., Lins, L. & Brasseur, R. *Biochemistry* **45**, 9336–9341 (2006).
- [6] García-Sáez, A. J., Chiantia, S., Salgado, J. & Schwille, P. *Biophysical Journal* **93**, 103–112 (2007).
- [7] Liu, Y. & Cheng, Q. *Anal. Chem.* **84**, 3179–3186 (2012).
- [8] Phillips, K. S. *et al. Anal. Chem.* **78**, 596–603 (2006).
- [9] Boukobza, E., Sonnenfeld, A. & Haran, G. *J. Phys. Chem. B* **105**, 12165–12170 (2001).
- [10] Berquand, A. *et al. Langmuir* **19**, 1700–1707 (2003).
- [11] Sarmento, M. J., Prieto, M. & Fernandes, F. *Biochimica et Biophysica Acta (BBA) - Biomembranes* **1818**, 2605–2615 (2012).
- [12] Kuhn, P. *et al. Integrative Biology* **4**, 1550–1555 (2012).
- [13] Kunding, A. H., Mortensen, M. W., Christensen, S. M. & Stamou, D. *Biophysical Journal* **95**, 1176–1188 (2008).
- [14] Elliott, A. D. *Curr Protoc Cytom* **92**, e68–e68 (2020).
- [15] Airy, G. B. *On the Diffraction of an Object-glass with Circular Aperture: From the Transactions of the Cambridge Philosophical Society, Vol. V, Part III.* (Printed at the Pitt Press by John Smith, 1835).
- [16] Image formation. in *Optical Physics* (eds. Tannhauser, D. S., Lipson, H. & Lipson, S. G.) 327–382 (Cambridge University Press, 1995). doi:[10.1017/CBO9781139170413.015](https://doi.org/10.1017/CBO9781139170413.015).
- [17] Latychevskaia, T. *Appl. Opt.* **58**, 3597–3603 (2019).
- [18] Semwogerere, D. & Weeks, E. R. Confocal microscopy. in *In Encyclopedia of Biomaterials and Biomedical Engineering, Biomaterials, Biomedical Engineering.* Informa Healthcare (2005).

- [19] Dunst, S. & Tomancak, P. *Genetics* **211**, 15–34 (2019).
- [20] Cole, R. W., Jinadasa, T. & Brown, C. M. *Nature Protocols* **6**, 1929–1941 (2011).
- [21] En.wikipedia.org. *Point spread function*. Available at: <https://en.wikipedia.org/wiki/Point_spread_function> Accessed 17 February 2022.
- [22] O. Beltramo-Martin *et al.* Review of PSF reconstruction methods and application to post-processing. In *Proc. SPIE* vol. 11448 (2020).
- [23] Scharr, H., Rademske, P., Alonso, L., Cogliati, S. & Rascher, U. *Remote Sensing of Environment* **267**, 112718 (2021).
- [24] Lee, J.-S., Wee, T.-L. E. & Brown, C. M. *J Biomol Tech* **25**, 31–40 (2014).
- [25] Wallace, W., Schaefer, L. H. & Swedlow, J. R. *BioTechniques* **31**, 1076–1097 (2001).
- [26] Aguet, F., Antonescu, C. N., Mettlen, M., Schmid, S. L. & Danuser, G. *Developmental Cell* **26**, 279–291 (2013).
- [27] Schindelin, J. *et al.* *Nature Methods* **9**, 676–682 (2012).
- [28] Ferhan, A. R. *et al.* *Nature Protocols* **14**, 2091–2118 (2019).
- [29] Crites, T. J. *et al.* *Curr Protoc Cell Biol* **68**, 24.5.1-24.5.31 (2015).
- [30] Castellana, E. T. & Cremer, P. S. *Surf Sci Rep* **61**, 429–444 (2006).
- [31] Zhu, Y. Preparation of Supported Lipid Bilayers. The Moran-Mirabal Research Group. <https://www.chemistry.mcmaster.ca/moran-mirabal/resources/SUPPORTED-LIPID-BILAYER-PREPARATION-SOP-9-2015.pdf>. (2015). Accessed February 10, 2022.
- [32] Gerke, V. & Moss, S. E. *Physiological Reviews* **82**, 331–371 (2002).
- [33] Hirai, Y. *et al.* *Asia Oceania J Obstet Gynaecol* **18**, 155–162 (1992).
- [34] Koopman, G. *et al.* *Blood* **84**, 1415–1420 (1994).
- [35] Blankenberg, F. G. *et al.* *Proc Natl Acad Sci USA* **95**, 6349 (1998).
- [36] Wang, J., Liu, J., Cao, Y., Hu, M. & Hua, Z. *Molecules* **22**, 2256 (2017).
- [37] Tait, J. F., Gibson, D. F. & Smith, C. *Analytical Biochemistry* **329**, 112–119 (2004).
- [38] Jin, M., Smith, C., Hsieh, H.-Y., Gibson, D. F. & Tait, J. F. *Journal of Biological Chemistry* **279**, 40351–40357 (2004).

[39] Janko, C. *et al. Physical Biology* **10**, 065006 (2013).

[40] Gauer, J. W. *et al. Biophysical Journal* **104**, 2437–2447 (2013).

[41] Kaptzy, J., Banman, S., Goping, I. S. & Mercer, J. R. *J Biomol Screen* **17**, 1293–1301 (2012).

Appendix 2.1: prepareDataForAnalysis.m

This short script takes a series of 4-scan hyperstack .tif images as input, and returns the individual scans saved in .tif format in a folder structure that can easily be parsed by cmeanalysis.

```
clear

main_dir = pwd;
save_dir = uigetdir();
disp(strrep(save_dir,pwd, ''))
filenames = uigetfile('.tif', 'MultiSelect', 'on');
no_files = length(filenames);

for i = 1:no_files
    cd(main_dir)
    filename = filenames{i};
    file = fopen(filename);
    tot_frames = length(file{1,1});
    lipid_ind = 1;
    proteina_ind = 2;
    lipid_ind2 = 3;
    lipid_ind3 = 4;
    lipid = uint16(zeros(2048,2048,length(lipid_ind)));
    proteina = uint16(zeros(2048,2048,length(proteina_ind)));
    lipid2 = uint16(zeros(2048,2048,length(lipid_ind2)));
    lipid3 = uint16(zeros(2048,2048,length(lipid_ind3)));

    for j = 1
        lipid(:, :, j) = file{1,1}{lipid_ind(j),1};
        proteina(:, :, j) = file{1,1}{proteina_ind(j),1};
        lipid2(:, :, j) = file{1,1}{lipid_ind2(j),1};
        lipid3(:, :, j) = file{1,1}{lipid_ind3(j),1};
    end

    BF_lipid = lipid(:, :, 1);
    BF_proteina = proteina(:, :, 1);
    BF_lipid2 = lipid2(:, :, 1);
    BF_lipid3 = lipid3(:, :, 1);

    lipid_filename = [filename(1:length(filename)-4), '_lipid.tif'];
    proteina_filename = [filename(1:length(filename)-4), '_proteina.tif'];
    lipid_filename2 = [filename(1:length(filename)-4), '_lipid2.tif'];
    lipid_filename3 = [filename(1:length(filename)-4), '_lipid3.tif'];

    lipid_save_dir = [save_dir, '/Cell', num2str(i), '/ch1'];
    mkdir(lipid_save_dir)
    cd(lipid_save_dir)
    imwrite(BF_lipid, lipid_filename)

    lipid_save_dir2 = [save_dir, '/Cell', num2str(i), '/ch2'];
    mkdir(lipid_save_dir2)
    cd(lipid_save_dir2)
    imwrite(BF_lipid2, lipid_filename2)

    lipid_save_dir3 = [save_dir, '/Cell', num2str(i), '/ch3'];
```

```
mkdir(lipid_save_dir3)
cd(lipid_save_dir3)
imwrite(BF_lipid3, lipid_filename3)

proteina_save_dir = [save_dir, '/Cell', num2str(i), '/ch4'];
mkdir(proteina_save_dir)
cd(proteina_save_dir)
imwrite(BF_proteina, proteina_filename)

close all
end

cd(main_dir)
```

Appendix 2.2: extractDetectionInfo.m

This script is used to extract the intensities of significant signals after running cmeanalysis. A quick calculation is carried out at the end to estimate the 3D concentration of surface bound vesicles (if they were in solution as opposed to surface-immobilized).

```
clear

od = pwd;
where_cells = uigetdir();
cd(where_cells)

all_files = dir;
all_dir = all_files([all_files(:).isdir]);
no_files = numel(all_dir)-2;

total_vesicles = 0;

for i = 1:no_files
    clear filename hval_Ar_total position A_vals_lipid A_vals_protein
    clear c_vals_lipid c_vals_protein A_vals_lipid_final A_vals_protein_final
        dirname = [where_cells, '/Cell', num2str(i), '/ch1'];
        cd(dirname);
        addpath(genpath([dirname, '/Detection/']))
        load('detection_v2.mat')

    %for the below, the first field is the result from runDetection
    %(frameInfo.XXX, where XXX can is A, c, x, y), the hval_Ar field is a
    %logical array where a 1 corresponds to a statistically significant
    %signal detected, and a 0 corresponds to no statistically significant
    %signal detected. the first row in hval_Ar will always be all 1's
    %because it's the master channel. for all lipid values, to make sure
    %that signal was detected in all three vesicle images over time,
    %multiply by the value in hval_Ar for both rows 3 and 4 (timepoints 2
    %and 3, respectively, based on the input of 1 -- vesicle 1, 2 --
    %protein 1, 3 -- vesicle 2, 4 -- vesicle 3)

    A_lipid =
    (frameInfo.A(1,:) .* frameInfo.hval_Ar(3,:) .* frameInfo.hval_Ar(4,:))';
    A_protein = (frameInfo.A(2,:) .* frameInfo.hval_Ar(2,:))';

    c_lipid =
    (frameInfo.c(1,:) .* frameInfo.hval_Ar(3,:) .* frameInfo.hval_Ar(4,:))';
    c_protein = (frameInfo.c(2,:) .* frameInfo.hval_Ar(2,:))';

    x_lipid =
    (frameInfo.x(1,:) .* frameInfo.hval_Ar(3,:) .* frameInfo.hval_Ar(4,:))';
    x_protein = (frameInfo.x(2,:) .* frameInfo.hval_Ar(2,:))';

    y_lipid =
    (frameInfo.y(1,:) .* frameInfo.hval_Ar(3,:) .* frameInfo.hval_Ar(4,:))';
    y_protein = (frameInfo.y(2,:) .* frameInfo.hval_Ar(2,:))';

    temp=length(A_lipid);
```

```

disp(['Cell number: ', num2str(i)])
disp(['A_lipid length: ', num2str(temp)])
total_vesicles = total_vesicles + temp;

for j = 1:length(A_lipid)

    final_A_lipid(j,i)=A_lipid(j);
    final_A_protein(j,i)=A_protein(j);
    final_c_lipid(j,i)=c_lipid(j);
    final_c_protein(j,i)=c_protein(j);
    final_x_lipid(j,i)=x_lipid(j);
    final_x_protein(j,i)=x_protein(j);
    final_y_lipid(j,i)=y_lipid(j);
    final_y_protein(j,i)=y_protein(j);
end
end

combined_A_lipid=vertcat(final_A_lipid(:));
combined_A_protein=vertcat(final_A_protein(:));
combined_c_lipid=vertcat(final_c_lipid(:));
combined_c_protein=vertcat(final_c_protein(:));
combined_x_lipid=vertcat(final_x_lipid(:));
combined_x_protein=vertcat(final_x_protein(:));
combined_y_lipid=vertcat(final_y_lipid(:));
combined_y_protein=vertcat(final_y_protein(:));
position=find(combined_A_lipid>0 & combined_A_protein>0);
distance = sqrt((combined_x_protein-combined_x_lipid).^2 +
(combined_y_protein-combined_y_lipid).^2);

final_colocalizations = [combined_A_lipid(position)
combined_A_protein(position)
combined_A_protein(position)./combined_A_lipid(position) distance(position)
combined_c_protein(position)];

%%%%%%%%%%%%%%%%%%%%%%%%%%%%%%%%%%%%%%%%%%%%%%%%%%%%%%%%%%%%%%%%%%%%%%%%
%apparent_lipid_concentration will be in units of Molar
%the calculation is:
%(avg # vesicles/image)*(20029 lipids/vesicle)*(23601 possible images per
%sample) / Avogadros # / volume of sample solution

%lipids per vesicle are approximated using the headgroup surface areas for
%the lipids being used and the following equation:

%N_tot = [4*pi*r^2 + 4*pi*(r-t)^2]/a

%where r is the radius of the vesicle, t is the thickness of the bilayer
&(usually ~5 nm), and a is the headgroup area of a particular lipid species

%possible images per sample are calculated by dividing the total surface area
%inside the pyrex cloning cylinder by the area per image obtained from the
%microscope

%%%%%%%%%%%%%%%%%%%%%%%%%%%%%%%%%%%%%%%%%%%%%%%%%%%%%%%%%%%%%%%%%%%%%%%%
mean_vesicles_per_image = total_vesicles / 5;
apparent_lipid_concentration = ((mean_vesicles_per_image * 20029 *
23601) / (6.02e23)) / (100e-6);

```

CHAPTER 3.

THE IMPACT OF MEMBRANE DEFECT PRESENTATION ON ALPHA-SYNUCLEIN BINDING TO MODEL MEMBRANES

Section 3.1: Overview

In chapter 1, I discussed many of the biophysical membrane parameters which have been shown to influence α Syn binding, including the membrane charge, temperature, and lipid composition. Many experiments have been performed to elucidate the individual roles these membrane parameters might play in driving α Syn binding, but a wide gap still exists between α Syn's normal physiological context and the simplified model systems used in a laboratory. α Syn is predominantly found in high concentrations in the axonal terminal of a neuron, where it is hypothesized to play an important role facilitating the transport of neurotransmitter-filled synaptic vesicles to the neuronal active zones for exocytosis [1]. While such a hypothesis is attractive for its simplicity, it raises several questions that need to be further addressed: if α Syn does play a role in the transport of neurotransmitter-filled vesicles, how exactly does it determine which vesicles are filled and ready for transport? Does the local membrane environment play a role in determining α Syn's preferred vesicular binding partners? And if so, what exactly is different about the membrane environment between empty and neurotransmitter-filled vesicles?

In considering the broader context of the synaptic vesicle cycle, one hypothesis that emerges is that α Syn may be able to differentiate between its empty and filled targets based on the membrane's osmotic tension. A hypo-osmotic tension occurs when there is a larger concentration of impermeable solute inside a vesicle than in the surrounding media; in an effort to equilibrate the concentration difference water will rush into vesicle, causing it to swell and producing an

TABLE 3 Post-dilution diameters of DOPG vesicles^a

Dilution factor	Extravesicular NaCl concentration (Hypotonic) (mM)	Mean vesicle diameter (nm)		Swelling (%)	Surface area increase
		Isotonic	Hypotonic		
3.0	250	115.0	118.2	3	2344.3 nm ²
4.6	163	115.2	121.4	5	4753.1 nm ²
7.3	103	115.0	122.0	6	5211.9 nm ²

Figure 3.1: Vesicle swelling as a result of osmotic pressure produces large increases in the vesicle surface area. In the experiments summarized above, vesicles comprised solely of 1,2-dioleoyl-sn-glycero-3-phospho-(1'-rac-glycerol) (DOPG) were subjected to increasing osmotic pressure by diluting the vesicles into solvent with a lower osmolarity. While only moderate swelling of the vesicles was observed by dynamic light scattering (DLS), such small swelling produces a substantial increase in the surface area of the vesicle. Since hydrophobic packing defects have been measured to be on the order of tens of square Angstroms in size, even small amounts of swelling like the ones pictured above are expected to produce many more packing defects. Adapted from [23].

increased lateral tension in the membrane. Since such an increase in osmotic tension has been shown to lead to an increase in the binding of the N-BAR domain of *D. Melanogaster* amphiphysin to its vesicular binding partners it seems logical that α Syn may rely a similar mechanism for differentiating between vesicles, but questions still arise regarding the exact mechanism by which α Syn might “sense” such a tension. [2].

In this chapter, I propose that α Syn is able to differentiate between potential binding partners based on differences in the membrane packing defects that arise from neurotransmitter loading and the subsequent membrane osmotic tension. Owing to their fluid nature under physiological conditions, all lipid membranes are hypothesized to display transient packing defects, or regions where the membrane’s hydrophobic core become temporarily solvent-accessible. Through this lens, an increase in osmotic tension could be interpreted as producing more defects on the vesicle surface due to the aforementioned swelling (figure 3.1); however, direct observation of such defects in a laboratory setting is currently difficult if not impossible due

to both their transiency (lifetime on the order of tens of picoseconds) and miniscule size (area on the order of tens of square angstroms) [3]. Thus, I have adopted a multifaceted experimental approach including both protein binding assays and molecular dynamics simulations intended to explore the relationship between osmotic tension and packing defect presentation, and the influences these phenomena have on α Syn binding.

As one part of my multifaceted approach, I will describe experiments conducted using the confocal protein binding assay detailed in chapter 2. In these experiments, fluorescently-tagged α Syn was titrated into a system where a glucose concentration gradient was used to achieve an osmotic tension in a previously-established synaptic vesicle model [4]. It should be noted that modeling osmotic tension in this way is inherently difficult and requires many assumptions to be made about how the model behaves, such as (1) assuming that the model vesicles will swell in a similar manner to synaptic vesicles without leaking their contents, and (2) that the number and size of membrane packing defects presented on the vesicle surface are directly correlated with the osmotic tension. Thus, to further support the hypothesis that α Syn binding is defect-mediated I will also present confocal binding data obtained using model vesicles where defect presentation was modulated by changing the lipid composition instead of imposing an osmotic gradient. Previous work using molecular dynamics simulations has shown that altering lipid composition is an effective way to guarantee differences in defect presentation, so these experiments serve as a valuable positive control for interpreting the more complicated osmotic tension system [3].

Taken together, data obtained from using the confocal binding assay show that defect presentation likely does influence α Syn binding, but any such increase in defect presentation as a

result of osmotic tension is small or unobservable using the methodology and synaptic vesicle mimics described herein. This conclusion is further supported by molecular dynamics simulations in which an artificial lateral tension was imposed on a flat membrane of the same model composition; these simulations were analyzed to determine membrane defect presentation using the published software PackMem [3]. In line with the aforementioned conclusion, increasing lateral tension does indeed correlate with more packing defects present in the membrane, but the observed trend is small and may not meaningfully influence α Syn binding on a macroscopically-observable scale. Taken together with the fact that purified synaptic vesicles have previously been shown to swell upon neurotransmitter loading, additional work clearly needs to be done to determine the mechanism of membrane swelling and how such behavior can be reproduced in a model system.

Section 3.2: Review of packing defects

Lipid packing defects are broadly defined as regions of a membrane where the hydrophobic core of the bilayer is accessible to the surrounding aqueous solvent. Traditionally, defects have been discussed in the literature from the perspective of lipid geometry and packing; they have been hypothesized to become more prevalent when bilayer lipids deviate from the canonical cylindrical shape or are less tightly packed. To illustrate this idea, consider the different lipids displayed in figure 3.2; depending on the overall structure of the lipid in question, we can assign a shape to it to describe how said lipid prefers to pack in a membrane. Lipids like 1,2-dipalmitoyl-*sn*-glycero-3-phosphocholine (DPPC), whose head group and tails occupy roughly the same cross-sectional membrane area, are assigned a cylindrical shape whereas others like 1,2-dioleoyl-*sn*-glycero-3-phosphate (DOPA), whose tails occupy more space than its head group, and 1-palmitoyl-2-

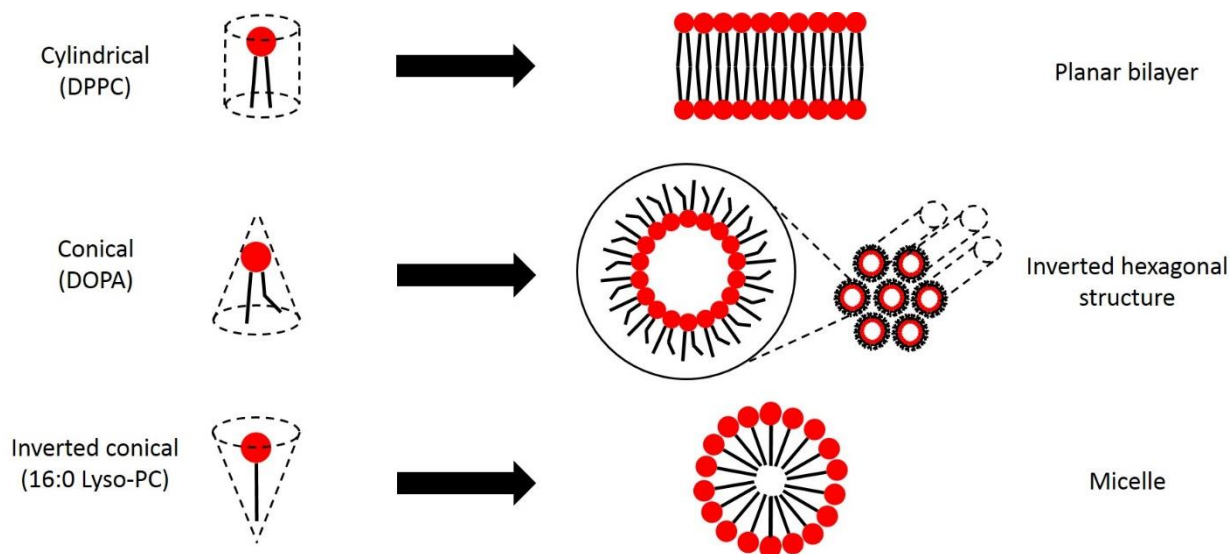


Figure 3.2: Lipid molecular geometry helps to predict pure equilibrium packing. Pure lipids will adopt specific energy-minimized structures based on their molecular geometry. Lipid species whose head group and tails occupy roughly the same amount of space are approximated as a cylinder and will prefer to form a planar lipid bilayer, whereas others will pack into an inverted hexagonal tubule structure or a micelle when the tails occupy more space than the head group or *vice versa*, respectively.

hydroxy-*sn*-glycero-3-phosphocholine (16:0 lyso PC), whose head group is much larger than its tails, are approximated as a cone and an inverted cone, respectively. Cylindrical lipids generally prefer to self-assemble as flat membranes to maintain efficient packing, whereas conical and inverted conical lipids prefer to pack into an inverted hexagonal phase or a micelle.

From the perspective of lipid geometry, packing defects are considered to arise when a bilayer contains a mixture of cylindrical and non-cylindrical lipids. For example, Vamparys *et al.* ran all-atom molecular dynamics simulations and characterized the defect presentation of bilayers containing both 1,2-dioleoyl-*sn*-glycero-3-phosphocholine (DOPC, a cylindrical lipid) and 1,2-dioleoyl-glycerol (DOG, a conical lipid); they found that the addition of 15 mol% DOG into an otherwise DOPC membrane resulted in a higher probability of large defects being present throughout their simulations [6]. In a companion paper, Vanni and coworkers took this idea one

step further and demonstrated that an amphipathic lipid packing sensor (ALPS) peptide prefers to bind to DOPC/DOG membranes displaying large defects over a similar 1,2-dimyristoyl-*sn*-glycero-3-phosphocholine (DMPC, a cylindrical lipid) membrane [9]. Considering these two studies together in concert with the complex compositions of physiological membranes, it becomes apparent that controlling the lipid composition (and hence, defect presentation) of various organelles and the plasma membrane is one approach cells can use to ensure binding specificity.

A variety of other membrane parameters have also been identified to impact defect presentation, including curvature, lipid tail identities, and cholesterol content. Molecular dynamics simulations run by Cui et al. demonstrated that imposing curvature on a flat membrane changed the distribution of available packing defects, with convex membranes presenting more and larger defects compared to a flat or concave membrane of the same composition [8]. This conclusion was further supported by the work of Vanni et al., who ran course-grained molecular dynamics simulations of 1-palmitoyl-2-oleoyl-*sn*-glycero-3-phosphocholine (POPC) membranes with increasing curvature and found that as the total curvature of the membrane increased (i.e., the radius of the cylindrical tube or vesicle decreased) so too did the size and distribution of defects on the outer leaflet [5]. Many similar studies have also correlated increasing curvature with increased binding of α -synuclein (α Syn), but few studies (if any) have extended this idea to encompass lipid packing defects [9-12].

The impact of lipid tails and cholesterol content on membrane defect presentation has also been explored, but to a lesser extent than curvature. To illustrate this, Pinot et al. noted that the inclusion of 30 mol% mono-polyunsaturated lipids into a POPC membrane caused an increased

presentation of shallow defects (depth ≤ 1 Å below the head group glycerol) at the expense of fewer deeper defects (depth > 1 Å below the head group glycerol) [13]. As polyunsaturated lipid tails have also been shown to preferentially associate with membrane-bound α Syn over other tails, one can easily draw the conclusion that α Syn binding is sensitive to shallow defect presentation in a membrane [20]. Similarly, the addition of 50 mol% cholesterol to a DOPC:DOPS bilayer (total composition 38:12:50 DOPC:DOPS:cholesterol) resulted in a greater area fraction of packing defects in the membrane compared to when cholesterol was absent; the authors rationalized that this increased defect presentation also would lead to increased α Syn binding, but due to the limitations of their study they stop short of reporting relative affinity constants [19]. While much remains to be explored regarding the impact of lipid composition and other physical parameters on membrane defect presentation, the aforementioned studies offer strong evidence that a better understanding of lipid packing defects will provide some much-needed context for the binding of all peripheral membrane proteins.

Part of the reason that defect presentation papers are so sparse in the literature is that membrane defects are incredibly difficult to study owing to their miniscule size and transient nature. To overcome this hurdle, in recent years many researchers have performed experiments *in silico* aimed at trying to quantify and explore the impact of membrane defects. The first example of this was published in 2011, when Cui and coworkers used a previously published accessible surface area (ASA) model to quantitatively characterize the differences in defect presentation between concave, convex, and flat membranes [6, 14, 15]. Vamparys *et al.* extended this framework further by developing a method to quantify packing defects based on a cartesian coordinate mapping, which was later streamlined and published for widespread use under the name

Name	POPC	POPS	DOPC	DOPS	DOPE	Cholesterol	18:1 biotinyl cap PE	Cy5-PE
SLB vesicles	0	0	99.5	0	0	0	0.5	0
Osmotic vesicles	0	0	55	20	14.4	10	0.5	0.1
monounsaturated	89.4	10	0	0	0	0	0.5	0.1
di-monounsaturated	0	0	89.4	10	0	0	0.5	0.1

Table 3.1: Vesicle compositions utilized in this chapter. The table above lists the various vesicle mixtures used in the experiments reported here. Osmotic vesicles were used for all experiments exploring the impact of osmotic tension, and were based on the composition utilized by Milovanovic et al [4]. Monounsaturated and di-monounsaturated vesicles were used to explore the impact of membrane defect presentation on α Syn binding without the use of osmotic tension. The supported lipid bilayer (SLB) vesicle mixture used was identical for all confocal binding assay experiments.

PackMem [2, 4]. At the time of writing this thesis, 22 journal articles have cited the use of PackMem, demonstrating the widespread scientific interest and increasing momentum in the field for studying membrane packing defects.

Section 3.3: Materials and methods

All lipids were purchased as either dried powders (POPC, POPS, DOPC, DOPS, DOPE, cholesterol, 18:1 biotinyl cap PE) or as a premixed chloroform solution (Cy5-PE) from Avanti Polar Lipids (Birmingham, AL). The compositions of all vesicles used in this chapter are reported in table 3.1 in units of mol%. All vesicles were prepared using the freeze-thaw-extrusion method previously discussed. Except where otherwise noted, vesicle solutions and sample manipulations were performed in HEPES-buffered saline (HBS, 10 mM HEPES, 150 mM NaCl, pH 7.2). For osmotic tension experiments, osmotic vesicles were prepared in HBS containing 150 mM glucose. Recombinant human α -synuclein nonspecifically labeled with HiLyte Fluor 488 was purchased from Anaspec Inc. (Fremont, CA, USA), and was aliquoted, flash frozen in liquid nitrogen, and stored at -80 °C until further use.

Section 3.3.1: Protocol for creating osmotically-stressed vesicles

For the osmotic tension experiments described in this chapter, I used a glucose loading protocol previously reported in the literature [2]. Briefly, small unilamellar vesicles (SUVs) of the desired composition were prepared in HBS containing 150 mM glucose (HBS-150). Separately, I also prepared an HBS solution containing 105 mM glucose (HBS-105). Prior to adding target vesicles to the passivated and streptavidin-incubated sample, a small volume of SUVs were diluted into a large volume of HBS-105 to produce a 45 mM hypo-osmotic glucose gradient across the vesicle. After exchanging the original sample buffer (HBS-150) for hypo-osmotic buffer (HBS-105), the confocal microscopy procedure was carried out as previously described in chapter 2. All other confocal binding assay experiments involving monounsaturated and di-monounsaturated vesicles were performed as described in chapter 2 without further procedural modification.

Section 3.3.2: Confocal microscopy parameters

Images were captured with a Leica SP8 3D STED laser scanning confocal microscope (Leica Microsystems, Inc., Buffalo Grove, IL) outfitted with a 63x/1.4 NA objective and supercontinuum white light laser. Excitation of Cy5-tagged vesicles was accomplished using a laser line at 633 nm with 10% laser intensity, and emission was collected over the range of 660-720 nm. Excitation of HiLyte Fluor 488-labeled α Syn was accomplished using a laser line at 488 nm with 20% laser intensity, and emission was collected over the range of 498-547 nm. Collected images were 2048 x 2048 pixels in size, and were obtained using a 400 Hz scan head speed corresponding to an optical dwell time of 0.591 ps. The confocal pinhole size used for all experiments was 0.5 Airy units in diameter. To boost low protein signals, three frames were averaged to produce the α Syn images used for analysis.

Section 3.3.3: Molecular dynamics simulations

Molecular dynamics simulations were performed using the NAMD software package [16]. Model lipid bilayers matching the osmotic vesicle composition mentioned previously were generated using the CHARMM-GUI membrane bilayer input generator [17]. Bilayers consisted of approximately 140 lipids per leaflet, and were solvated with explicit water containing 150 mM NaCl; water and ion placement were initialized with a distance-based algorithm. A total of 8 simulations were performed in 2 femtosecond increments for 300 ns each using an NP γ T ensemble, in which the number of atoms (N), pressure (P), surface tension of the bilayer (γ), and temperature (T) were held constant while the total area of the membrane was allowed to fluctuate. Each of the 8 simulations were initialized with a different surface tension to compare the impact of tension on defect presentation; simulated tensions include 0, 0.95, 1.9, 2.8, 3.8, 5, 6, and 7 mN/m, which were selected to mimic the osmotic tensions probed using the confocal binding assay.

Section 3.3.4: Quantifying membrane defect presentation using PackMem

Once each simulation completed 300 ns total of production runs, packing defect analysis was performed on the completed trajectory using PackMem. As previously mentioned, PackMem is a software package used for analyzing the hydrophobic defect presentation of an MD-simulated lipid membrane. Briefly, for each frame analyzed, PackMem generates a Cartesian grid of $1 \times 1 \text{ \AA}$ “patches” overlaid over one leaflet of the simulated membrane. The program then iteratively explores the membrane atoms underneath each grid patch up to a depth d below the central glycerol carbon atom of a lipid; for all analysis presented here, we explored up to the recommended depth $d = 1 \text{ \AA}$ below the average glycerol carbon plane. Individual grid patches are assigned a representative value of 1, 0.1, or 0 if the program first encounters a polar atom, non-polar atom, or

no atom at all, respectively, during its analysis; these values correspond to no defect being present, a shallow membrane defect being present, or a deep defect being present beneath the grid patch, respectively. Once all bilayer patches are explored and defects are classified, defects of the same type on adjacent grid patches are grouped together to allow a total defect area to be calculated. This process is repeated iteratively for one in every five frames extracted from the completed MD trajectory, corresponding to one defect analysis performed for every 100 ps of simulation time; this rate of sampling was selected to guarantee zero correlation between analyzed frames, as previous work has suggested that the lifetime of any given defect will be less than 20 ps [5].

Once PackMem analysis was completed, a separate script provided by the PackMem authors in the R coding language was used to visualize and fit the data. Previous work by the authors and others found that the probability of observing some defect of size A in a simulation can be described by the following relation,

$$p(A) = be^{-A/\pi}$$

where $p(A)$ is the probability of finding a defect of size A in the membrane, b is a pre-exponential fit factor omitted from further analysis, and π is an author-defined packing defect constant in units of \AA^2 [4, 6]. Generally, one can interpret the packing defect constant as a measure of both the quantity and size of defects in a membrane; a higher packing defect constant implies both more and larger defects were present in a simulation. Taking the natural log of the equation above,

$$\ln(p(A)) = \ln(b) - \frac{A}{\pi}$$

we find that the packing defect constant π can easily be obtained as the slope of a line fit to a plot of $\ln(p(A))$ vs. A for any given simulation (figure 3.3). It should be noted that fits performed in this manner omit defects smaller than 15 \AA^2 in size as well as any defects with sufficiently low probability of occurring (i.e., any defects with probability of less than 10^{-4} of occurring) due to expected deviation from linear behavior. Packing defect constants obtained in this manner can be compared across simulations to provide insight into expected differences in their experimental behavior.

Section 3.4: Osmotic tension does not appear to measurably impact α Syn binding

In this study, the association of α Syn with model vesicles under isotonic and hypo-osmotic conditions was assessed using the confocal protein binding assay described in chapter 2. Sample

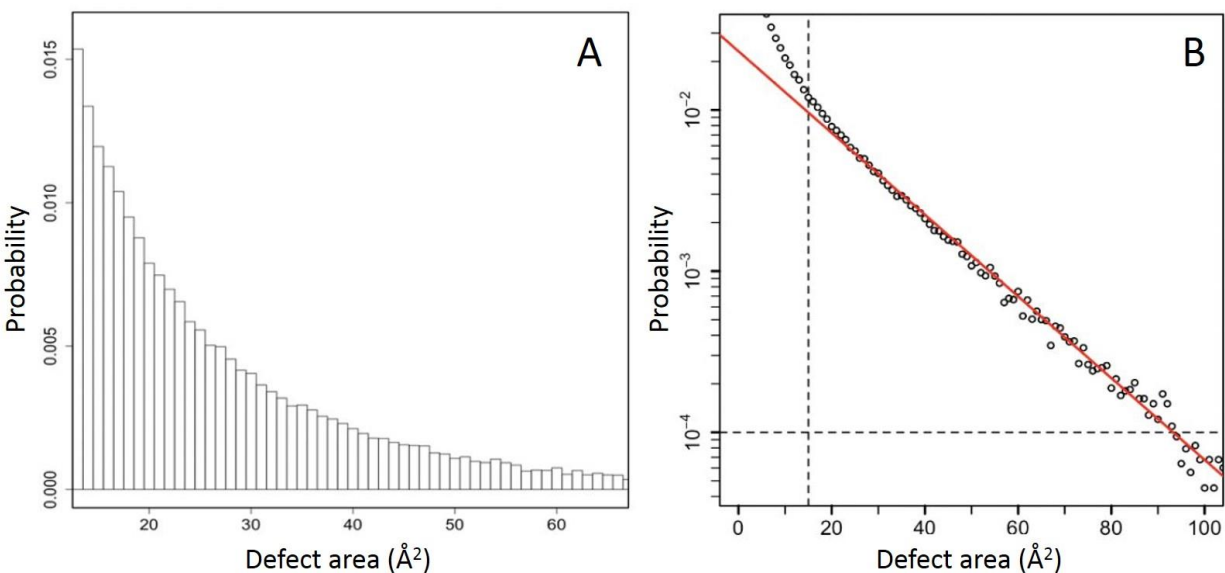


Figure 3.3: Sample plots displaying the probability of finding a defect of a given area in a simulation. (A): Histogram detailing all of the membrane defects larger than 15 \AA^2 over the course of a simulation with zero lateral tension. **(B):** Semilog plot of the histogram presented in panel A; the slope of the line fit to this plot is the packing defect constant π . Dashed lines represent regions of the plot that were omitted from fitting.

microscopy images used for analysis are reproduced in figure 3.4, and data analyzed with cmeanalysis and fit with a standard Michaelis-Menten model for protein binding are presented in figure 3.5. With a total of 89 isotonic and 98 hypo-osmotic samples containing hundreds of thousands of total vesicles analyzed, I found that α Syn has a dissociation constant of 10.56 ± 4.22 nM and a mean relative intensity at saturation of 0.037 ± 0.003 for isotonic vesicles, and a dissociation constant of 12.86 ± 3.90 nM and a mean relative intensity at saturation of 0.039 ± 0.002 for hypo-osmotically stressed vesicles; in other words, for the model synaptic vesicle mimics used here I found that there was no substantial difference in α Syn binding to osmotic vesicles under isotonic or hypo-osmotic conditions. These data have additionally been corroborated using the well-established tryptophan fluorescence assay by other members of my lab. Discussion of

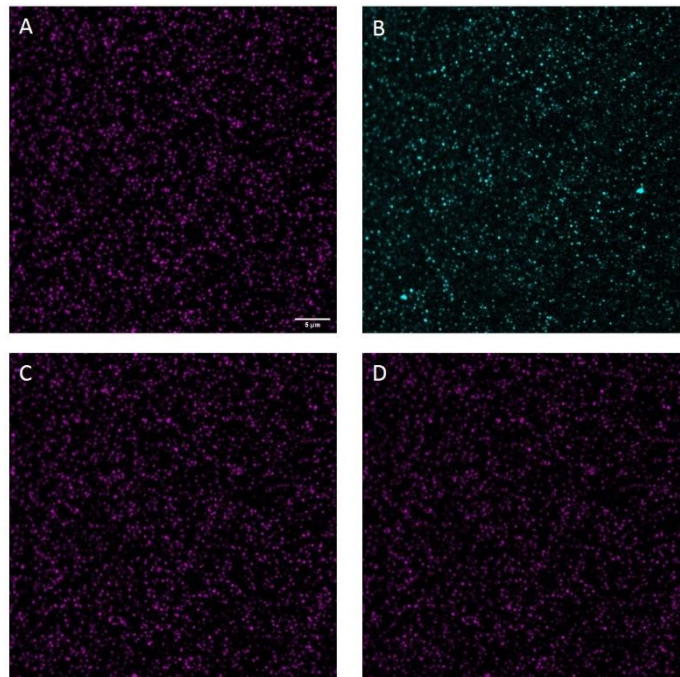


Figure 3.4: Sample images of HiLyte Fluor 488-tagged α Syn binding obtained using the confocal assay. Pictured above are four scans which comprise a single image obtained in the measurement of α Syn-488 binding to DO vesicles. (A): First scan of vesicles containing a small amount of Cy5-PE. (B): Scan of the α Syn-488. (C, D): Second and third vesicle scans, respectively, used to determine if vesicles are properly immobilized. All images have been contrast-enhanced with post-analysis look-up tables (LUTs) for visual clarity. The white scale bar represents 5 μ m.

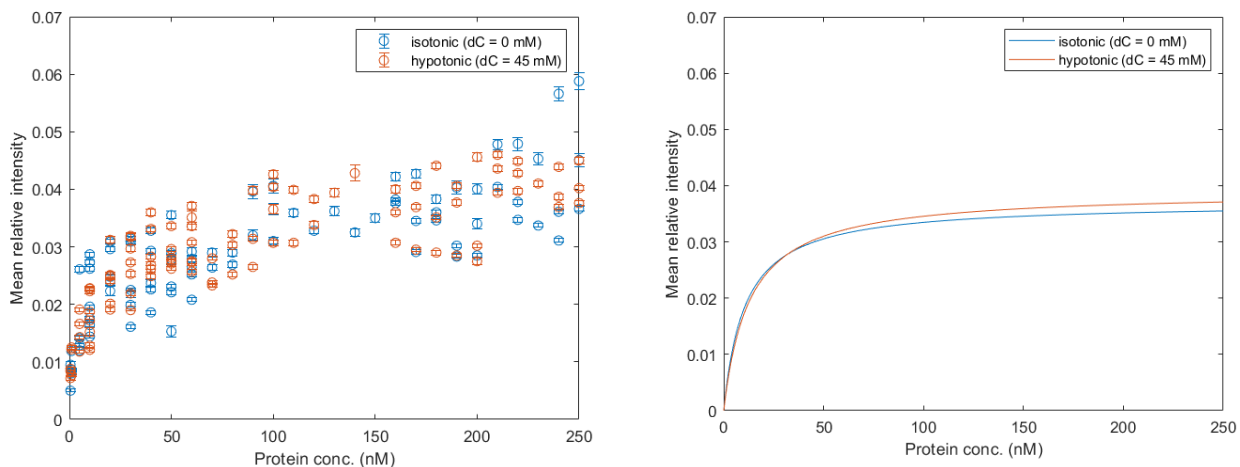


Figure 3.5: Aggregate mean relative intensity data for α Syn binding to osmotic vesicles. (Left): Mean relative intensity data obtained from osmotic vesicles under both isotonic and hypotonically-stressed conditions. **(Right):** Robust fits for the mean relative intensity data using a standard Michaelis-Menten model of binding.

these results and the inherent difficulties and limitations of the model system used will be outlined in section 3.6.

Defect distribution analysis including linear regression fitting for extraction of the packing defect constant and comparison of fit defect constants for the model osmotic vesicle membrane simulated under different lateral tensions is presented in figure 3.6. While there does not seem to be any meaningful trend in the deep defect presentation across simulated tensions, there is a small but clear increase in both the shallow defect presentation and the overall defect presentation as a function of increasing tension. These results support our initial hypothesis that increased osmotic tension across a membrane results in greater defect presentation, but it remains unclear whether such a small increase in packing defect constant will manifest as tangible differences in α Syn binding.

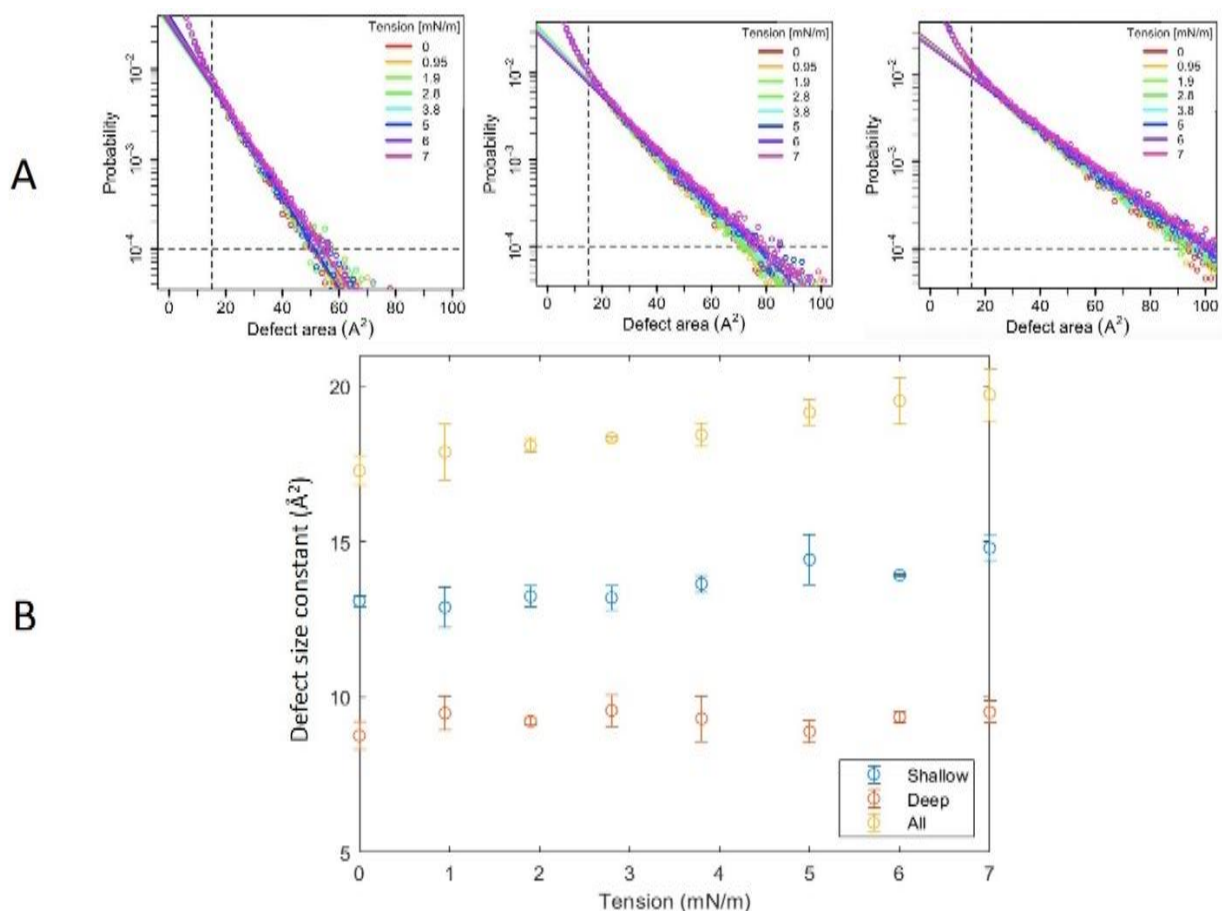


Figure 3.6: Linear regression fitting and packing defect size constants obtained from molecular dynamics simulations of a membrane under variable lateral tension. (A): Linear regression fits for the probability of finding different defects throughout the course of a simulation. **Left:** Deep defects (no atoms encountered during search). **Center:** Shallow defects (hydrophobic atoms encountered during search). **Right:** All defects. **(B):** Defect size constants extracted from the linear regression fits in A. While there doesn't appear to be a trend in the deep defect constant across simulations, both shallow and all defect constants show slight increases as a function of increasing lateral tension. Error bars represent the error in the defect size constant obtained by block averaging, as reported in [3].

Section 3.5: α Syn exhibits differential binding as a function of lipid tail composition

In addition to the aforementioned osmotic experiments and molecular dynamics simulations, I elected to explore differences in α Syn binding using a different set of model vesicles that did not rely on osmotic tension for modulating defect presentation. For these experiments, membrane defect presentation was varied by changing the composition of the lipid tails from 50/50 saturated/monounsaturated (hereon referred to as monounsaturated) to 100% monounsaturated

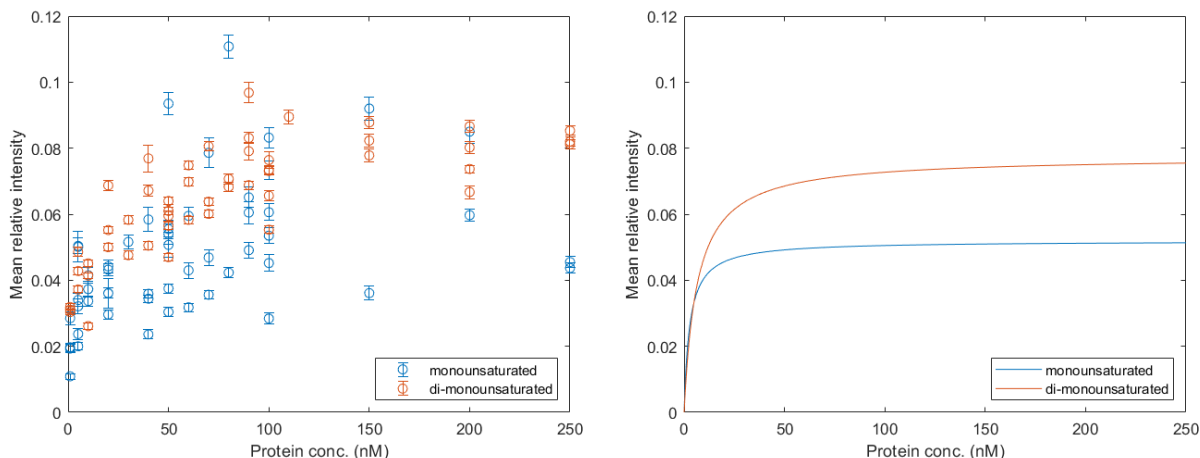


Figure 3.7: Aggregate mean relative intensity data for α Syn binding to monounsaturated and di-monounsaturated vesicles. (Left): Mean relative intensity data obtained from analyzing α Syn’s binding to monounsaturated and di-monounsaturated vesicles (see table 3.1 for exact compositions). **(Right):** Robust fits for the mean relative intensity data using a standard Michaelis-Menten model.

(hereon referred to as di-monounsaturated) while maintaining an identical distribution of lipid head groups between vesicle samples; as previous work reported in the literature shows that substituting the lipid tails in this way results in a higher packing defect constant, I expect there to be quantifiable differences in α Syn binding between these samples if the protein is indeed defect sensing [5].

Binding curves for α Syn associating with either monounsaturated or di-monounsaturated vesicles collected using the confocal binding assay are presented in figure 3.7. Fitting was performed using a standard single-site binding model,

$$\text{Bound fraction} = b * \frac{[\alpha\text{Syn}]}{K_d + [\alpha\text{Syn}]}$$

where $[\alpha\text{Syn}]$ is the concentration of added αSyn , K_d is the equilibrium dissociation constant, and b is a unitless fit parameter representing the mean relative intensity at saturation. Using this model, I found that αSyn has a dissociation constant of 2.76 ± 2.63 nM and a saturation mean relative intensity value of 0.052 ± 0.006 for monounsaturated vesicles, whereas di-monounsaturated vesicles produced a dissociation constant of 6.50 ± 3.42 nM and a saturation mean relative intensity value of 0.077 ± 0.006 ; the reported uncertainty represents the 95% confidence interval in the fit.

Section 3.6: Discussion

At the start of this work, I set out to determine what role, if any, osmotic tension plays in allowing αSyn to differentiate between vesicular binding partners; as a result of increased defect presentation, I hypothesized that I would be able to measure stronger αSyn binding to a hypo-osmotically stressed vesicle compared to an isotonic vesicle of the same composition. However, when considering the results of both the confocal binding assay using osmotic vesicles and the packing defect analysis under increasing lateral tension, it becomes clear that more work using different model systems is necessary to determine the validity of this hypothesis.

A key component of the original hypothesis was the assumption that synaptic vesicles (and their synthetic mimics utilized here) will swell upon exposure to a hypo-osmotic gradient; more lipid packing defects will thus be presented to the external aqueous environment as a function of this swelling, resulting in an enhancement of αSyn binding. Although there is literature precedent which suggests that synaptic vesicles can swell to produce up to a 50% increase in vesicle surface area or 100% increase in internal volume upon neurotransmitter loading, such an effect has not been observed for synthetic vesicles of various compositions [20-22]. Indeed, the only quantitative

correlation between osmotic tension and vesicle swelling empirically reported in the literature uses dynamic light scattering (DLS) to approximate the change in vesicle diameter under a hypo-osmotic gradient; even with an osmotic gradient of ~ 150 mM NaCl across the vesicle ($C_{\text{inside, NaCl}} > C_{\text{outside, NaCl}}$), the authors only observed a 6% increase in the average radius of DOPG vesicles [23]. Similar experiments performed in my lab reinforce this conclusion, as we observed a negligible increase in the average radius of osmotic vesicles *via* DLS upon subjecting them to a hypo-osmotic gradient ($\Delta c = 50$ mM glucose, data not shown). Thus, I can conclude that under the experimental conditions used here an osmotic gradient across the vesicles was likely produced as expected, but this gradient likely did not produce substantial swelling which would result in a measurable increase in α Syn binding.

Another factor which may explain α Syn's similarities in binding to osmotically-stressed vesicles and their isotonic counterparts has to do with our stress-inducing protocol. In the osmotic tension experiments described here, I initially prepare vesicles in HBS containing 150 mM glucose; an osmotic gradient is then created by diluting these vesicles into a buffer containing 105 mM glucose. An assumption inherent to this procedure is that under these conditions the vesicles will maintain their contents over the course of an experiment. Although literature precedent suggests that the half-life for glucose permeating model vesicles is on the order of tens of hours [23], our original hypothesis did not consider that the binding of α Syn to an osmotically-stressed vesicle could result in leakage of the vesicle's contents. As vesicle leakage upon α Syn binding has been reported to occur in experiments involving both monomeric and oligomeric protein [24, 25], it seems logical to believe that membrane permeabilization is also occurring in my experiments and resulting in the observed similarities in binding. To assess this, both a calcein leakage assay

and a glucose leakage assay were performed with osmotic vesicles under both isotonic and hypo-osmotic conditions; these assays were selected to complement each other due to the substantial size difference between a single calcein and a glucose molecule. In performing these assays using our osmotic vesicle model system we found that the addition of α Syn did not cause significant leakage of calcein under either isotonic or hypo-osmotic conditions; in contrast, results obtained using the glucose oxidase assay were inconclusive due to our concentrations being well below the lower detection limit of the assay. Therefore, while we can reasonably say that large osmolytes like calcein would be sufficiently trapped within a vesicle over the course of our experiments, we cannot say for certain if this behavior extends to smaller molecules like glucose; if glucose were indeed leaking from osmotically-stressed vesicles upon α Syn binding, this would easily explain the observed similarities in binding behavior between isotonic and hypotonically-stressed vesicles, but more work is necessary to show that this is the case.

The different results obtained between the MD simulations and the confocal binding assay can also be explained by interrogating the assumptions inherent in our hypothesis. In the MD simulations described here, we make the assumption that a lateral tension applied to a flat membrane is a good proxy for the osmotic tension experienced by the vesicles in the confocal binding assay. This assumption is reasonable in the context of studying planar bilayers or giant unilamellar vesicles where the local protein environment is approximately flat, but tends to break down as the radius of the vesicle decreases and curvature increases. To illustrate this concept, consider the differences in lipid shapes discussed in section 3.2; lipids with a cylindrical shape like DPPC will pack most efficiently in a flat bilayer. If such a bilayer were to become more and more curved, we would expect more and more lipid packing defects to arise due to the geometrical

mismatch between the inner and outer leaflets of the membrane, even under isotonic conditions. Thus, in the extreme of very small vesicle radii and very high local curvature used in the confocal binding assay, it is possible that lipid packing defects sufficient for α Syn binding exist even without the application of an osmotic gradient. To put this another way, it is entirely possible that impact of high curvature on membrane defect presentation far outweighs any osmotic effect; this would explain why we see a clear increase in defect presentation on flat membranes with increasing lateral tension while observing minimal difference in α Syn binding to osmotically-stressed SUVs.

As a positive control for varying packing defect presentation, I opted to study α Syn binding using more simplified monounsaturated and di-monounsaturated vesicles. In these experiments, I am assuming that a change in the lipid tail composition will manifest changes in the packing defect presentation and a measurable difference in α Syn binding; literature precedent supports this idea, even though exact packing defect constants for the compositions used here are not presented [5]. In comparing the results obtained from monounsaturated and di-monounsaturated vesicles using the confocal binding assay we clearly see a difference in the maximum mean relative intensity at saturation (b); this difference suggests that packing defects do indeed play a role in α Syn binding by regulating the total amount of α Syn that can bind to a given membrane. Strangely, though, it appears as if the equilibrium dissociation constant slightly *increases* (i.e., the binding of α Syn is *weaker*) with increasing packing defect presentation, which is contrary to my prediction that more defects would equate to stronger binding. One potential explanation for this behavior is that α Syn's affinity for a membrane defect could be constant if the defect is above a certain size threshold; if this were the case, we would expect the primary difference between monounsaturated and di-

monounsaturated vesicles would be the total number of available defects for α Syn to bind. This expectation jives with the observed differences in mean relative intensity at saturation, and is also supported by similar fluorescence experiments where α Syn was found to have a constant dissociation constant when binding to vesicles of varying size [12].

On the other hand, another potential explanation for the observed differences in α Syn binding to monounsaturated and di-monounsaturated vesicles is that these compositions may create different defect environments. As the mean relative intensity at saturation clearly changes between monounsaturated and di-monounsaturated vesicles, it is reasonable to assume that the total number of defects (and therefore, binding sites) present on the vesicles is changing, but it remains unclear whether there are differences in the exact nature and composition of the defects present (e.g., defects present in these two systems may be comprised of different ratios of shallow and deep elemental defects). For example, one could imagine a situation where the distribution of shallow and deep defects differs between the different membranes studied; if α Syn has a preference for one defect type over the other, then we would expect it to bind more strongly (i.e., with a lower K_d) to the composition exhibiting more of those types of defects regardless of the total number of defects present. Thus, the differences in measured dissociation constants between monounsaturated and di-monounsaturated vesicles could potentially result from other changes in the defect environment of these vesicles, but more computational work exploring the distribution of defects on these membranes is necessary to solidify this link.

In assessing the presented data, the question also arises whether our model system is a good representation of true physiological behavior. In the experiments reported here, I have used

synthetic vesicles as a tool to explore the ways that membrane defect presentation can impact α Syn binding; while these experiments are useful to elucidate this very specific relationship, at present it is unclear how these observations will translate to *in vivo* behavior. For starters, the composition of an actual synaptic vesicle differs wildly from the model systems studied here; Takamori and coworkers estimate that roughly 25% of the total membrane volume is occupied by bulky transmembrane protein domains, which would likely impact both membrane dynamics and defect presentation and has been suggested to contribute to vesicle swelling [20, 26]. Additionally, physiological synaptic vesicles contain a high proportion of both long-chain polyunsaturated lipids and cholesterol, where the former has been shown to display a preference for associating with α Syn over their saturated or monounsaturated counterparts and the latter has been suggested to contribute to synaptic vesicle swelling [14, 27]. More work is clearly necessary to continue to bridge the gap between our study of model systems and true protein behavior *in vivo*.

Section 3.7: References

- [1] Bellani, S. *et al. Commun Integr Biol* **3**, 106–109 (2010).
- [2] Hutchison, J. B., Karunanayake Mudiyansele, A. P. K. K., Weis, R. M. & Dinsmore, A. D. *Soft Matter* **12**, 2465–2472 (2016).
- [3] Gautier, R. *et al. Biophysical Journal* **115**, 436–444 (2018).
- [4] Milovanovic, D., Wu, Y., Bian, X. & De Camilli, P. *Science* **361**, 604 (2018).
- [5] Vanni, S., Hirose, H., Barelli, H., Antony, B. & Gautier, R. *Nature Communications* **5**, 4916 (2014).
- [6] Vamparys, L. *et al. Biophysical Journal* **104**, 585–593 (2013).
- [7] Vanni, S. *et al. Biophysical Journal* **104**, 575–584 (2013).
- [8] Cui, H., Lyman, E. & Voth, G. A. *Biophysical Journal* **100**, 1271–1279 (2011).
- [9] Middleton, E. R. & Rhoades, E. *Biophysical Journal* **99**, 2279–2288 (2010).
- [10] Pranke, I. M. *et al. J Cell Biol* **194**, 89–103 (2011).
- [11] Davidson, W. S., Jonas, A., Clayton, D. F. & George, J. M. *Journal of Biological Chemistry* **273**, 9443–9449 (1998).
- [12] Jensen, M. B. *et al. Journal of Biological Chemistry* **286**, 42603–42614 (2011).
- [13] Pinot, M. *et al. Science* **345**, 693 (2014).
- [14] Brummel, B. E., Braun, A. R. & Sachs, J. N. *Biochim Biophys Acta Biomembr* **1859**, 529–536 (2017).
- [15] Liu, J. *et al. Phys. Chem. Chem. Phys.* **23**, 2117–2125 (2021).
- [16] Humphrey, W., Dalke, A. & Schulten, K. *Journal of Molecular Graphics* **14**, 33–38 (1996).
- [17] Hubbard, S. J. & Thornton, J. M. *NACCESS*. (Department of Biochemistry and Molecular Biology, University College London, 1993).
- [18] Phillips, J. C. *et al. J. Chem. Phys.* **153**, 044130 (2020).
- [19] Jo, S., Kim, T., Iyer, V. G. & Im, W. *Journal of Computational Chemistry* **29**, 1859–1865 (2008).

- [20] Budzinski, K. L. *et al. Biophysical Journal* **97**, 2577–2584 (2009).
- [21] Mui, B. L., Cullis, P. R., Evans, E. A. & Madden, T. D. *Biophysical Journal* **64**, 443–453 (1993).
- [22] Lin, C.-M., Wu, D. T., Tsao, H.-K. & Sheng, Y.-J. *Soft Matter* **8**, 6139–6150 (2012).
- [23] Ertel, A., Marangoni, A. G., Marsh, J., Hallett, F. R. & Wood, J. M. *Biophys J* **64**, 426–434 (1993).
- [24] Hannestad, J. K. *et al. Proc Natl Acad Sci USA* **117**, 14178 (2020).
- [25] van Rooijen, B. D., Claessens, M. M. A. E. & Subramaniam, V. *PLoS One* **5**, e14292–e14292 (2010).
- [26] Takamori, S. *et al. Cell* **127**, 831–846 (2006).
- [27] Lee, J.-S., Cho, W. J., Shin, L. & Jena, B. P. *Exp Biol Med (Maywood)* **235**, 470–477 (2010).

CHAPTER 4.

THE C-TERMINAL DOMAIN OF ALPHA-SYNUCLEIN CONFERS STERIC STABILIZATION ON SYNAPTIC VESICLE-LIKE SURFACES

Section 4.1: Overview

The membrane-binding region of α Syn has been well characterized and shown to bind to highly charged and highly curved lipid membranes; it is commonly accepted that the first ~100 residues of the protein adopt an α -helical structure upon associating with synaptic vesicles, their hypothesized physiological target [1]. While we have a general understanding of how the N-terminal and non-amyloid β component (NAC) domains of the protein contribute to its overall behavior, much remains to be explored regarding the role of the C-terminal domain and its impact on α Syn's function; this is especially apparent considering that phosphorylation of Serine-129 within this domain is one of the clearest indicators of both sporadic and familial Parkinson's disease, despite not knowing how this post-translational modification interacts with or contributes to the diseased state. Exhibiting no known strong interaction partners, the best-established property of the C-terminal domain is that it increases the solubility of α Syn and other proteins through chaperone-like activity [2]. Additionally, other studies have suggested that α Syn modulates the interaction potential between synaptic vesicles through its C-terminal domain, but probing the force response behavior of the C-terminal domain specifically has been experimentally intractable [3]. α Syn's apparent preference for highly curved and highly charged membranes precluded the use of the relatively planar sample substrates prepared for atomic force microscopy, and possible cooperativity between multiple α Syn C-terminal domains once bound to a membrane prohibits single-molecule optical or magnetic tweezer experiments. The lack of tools capable of examining

the interaction potentials of organelle-like membrane surfaces remains a critical barrier to understanding the biophysical function of membrane proteins.

To directly probe the force response of α Syn bound to membrane surfaces, we utilized novel spherical nanoparticle-supported lipid bilayers (SSLBs) and small-angle x-ray scattering (SAXS) to measure the interaction forces between SSLBs with bound α Syn as a function of depletion attraction [4-6]. The nanoparticle core of SSLBs offers unique advantages; not only does the core enforce monodisperse, highly charged membrane curvature akin to that found in synaptic vesicles, but it also affords us increased contrast for performing SAXS measurements. A previous study in the Lee lab used the high scattering cross-section of SSLBs to demonstrate via x-ray photon correlation spectroscopy (XPCS) that the addition of α Syn disperses SSLB aggregates and sterically stabilizes membrane surfaces [7]. While this phenomenon was observed and characterized, the nature of the steric stabilization and which domains of α Syn contributed to this effect remained unclear.

In this chapter, I will provide experimental evidence that the C-terminal domain of α Syn is the primary contributor to the steric stabilization of membrane surfaces. By increasing depletion attraction forces through the addition of polyethylene glycol (PEG), we have measured the force response of α Syn-bound SSLBs using SAXS. Not only does the inclusion of wild-type α Syn increase the osmotic pressure required to reversibly aggregate SSLBs, but complementary experiments involving a C-terminal truncated version of the protein (residues 1-101 out of 140) also show that the C-terminal domain is responsible for the majority of this effect. Data with increasing monovalent salt in solution suggest that steric stabilization is due in part to the

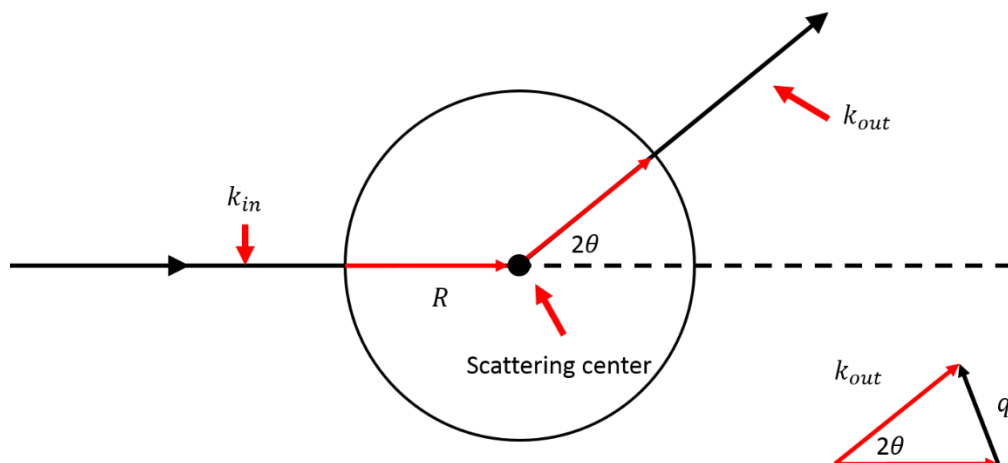


Figure 4.1: Diagram of the interaction between a point scatterer and an x-ray. An incident beam k_{in} will interact with the electrons of the scattering center and be deflected at some angle 2θ . Rearranging these vectors, we can define the wavevector transfer q to completely describe the scattering event.

polyelectrolytic nature of the highly-anionic C-terminal domain. Remarkably, we also found that small concentrations of divalent salts like Ca^{2+} and Mg^{2+} decrease steric stabilization, with calcium providing the stronger effect of the two.

Section 4.2: Methods

Section 4.2.1: Theory of small-angle x-ray scattering (SAXS)

Small-angle x-ray scattering (SAXS) is a high-energy x-ray technique that excels at elucidating the size and structure of electron-dense objects in solution. To understand the basic principles and applications of SAXS, we should first consider the interaction between an x-ray and a point scatterer. An electron-dense object like the one depicted in figure 4.1 will cause an incident beam of x-rays to scatter at a certain angle. If we define this angle as 2θ we can then rearrange the incident and scattered x-ray vectors to define a single vector q , called the wavevector transfer, which accurately describes the scattering event,

$$\vec{q} \equiv k_{out} - k_{in} = \frac{4\pi}{\lambda} \sin \theta$$

where k_{out} is the scattered x-ray, k_{in} is the incident x-ray, and λ is the wavelength of the x-ray. The wavevector transfer of many particles in solution will be related to the scattered x-ray amplitude and intensity according to the general scattering equation,

$$I_{SAXS}(\vec{q}) = |A(\vec{q})|^2 = \left| \int_V \rho(\vec{r}) e^{i\vec{q}\cdot\vec{r}} d^3r \right|^2$$

where $I(q)$ is the scattered intensity, $A(q)$ is the scattered amplitude, $\rho(r)$ is the scattering length density at some position r , and the exponential term $e^{i\vec{q}\cdot\vec{r}}$ is the phase factor of the scattered beam. For the example where x-rays are being scattered from a single point scatterer in solution, the general scattering equation can be rewritten as

$$I(\vec{q})_P = |\rho_P - \rho_{solvent}|^2 \left| \int_{V_P} e^{i\vec{q}\cdot\vec{r}} dV_P \right|^2 = |\Delta\rho|^2 V_P^2 |F(\vec{q})|^2$$

where the subscript P denotes a single particle and $F(q)$ is the single particle form factor, defined generally as

$$F(\vec{q}) = \frac{1}{V_P} \int_{V_P} e^{i\vec{q}\cdot\vec{r}} dV_P$$

The form factor shown above can take many forms depending on the size, shape, and movement of the particles in solution, exemplified by the variety and depth of form factors found in the relevant literature [8-10]. If we assume that our single particle in solution is a perfect sphere, we can evaluate the form factor above analytically by translating it into spherical coordinates

$$F(\vec{q}) = \frac{1}{V_P} \int_0^R r^2 \int_0^{2\pi} \int_0^\pi e^{i|\vec{q}r|\cos\theta} \sin\theta \, d\theta d\phi dr$$

$$F(\vec{q}) = \frac{1}{V_P} \int_0^R 4\pi r^2 \frac{\sin(\vec{q}r)}{\vec{q}r} dr$$

$$F(\vec{q}) = 3 \left(\frac{\sin(\vec{q}r) - \vec{q}r \cos(\vec{q}r)}{(\vec{q}r)^3} \right)$$

This relationship can be further simplified to

$$F(\vec{q}) = \frac{3J_1(\vec{q}r)}{\vec{q}r}$$

using the definition of the first spherical Bessel function

$$J_1(\vec{q}r) = \frac{\sin(\vec{q}r)}{(\vec{q}r)^2} - \frac{\cos(\vec{q}r)}{(\vec{q}r)}$$

where J_1 is a Bessel function of the first kind. With this expression for the form factor, the scattered intensity of a single particle can then be rewritten as

$$I(\vec{q})_P = |\Delta\rho|^2 V_P^2 |F(\vec{q})|^2 = |\Delta\rho|^2 V_P^2 \left| \frac{3J_1(\vec{q}r)}{\vec{q}r} \right|^2$$

The emergence of a Bessel function in the form factor above implies that the SAXS profile for a point scatterer will display a period of oscillations inversely proportional to the scatterer's radius. Data obtained from a solution containing only monodisperse silica nanoparticles confirms this behavior and provides a reference point for exploring other spherical scatterers (figure 4.2).

In addition to exploring the size and behavior of individual scatterers, SAXS is also capable of reporting on the macromolecular arrangement and interparticle correlations of many particles

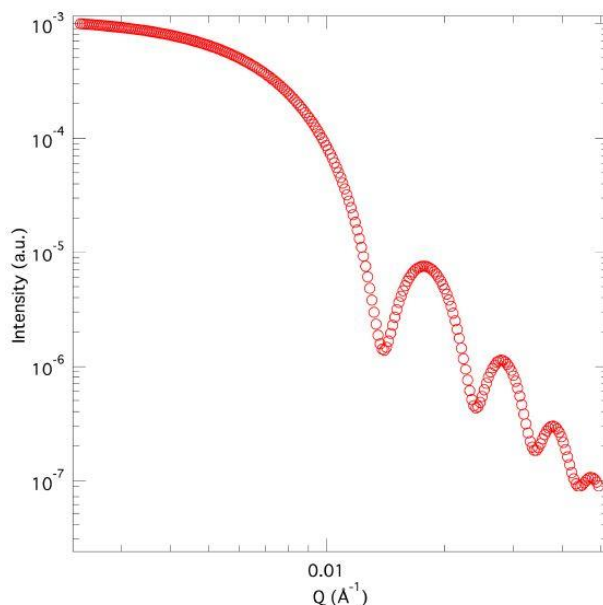


Figure 4.2: Sample SAXS scattering profile obtained for 60 nm silica nanoparticles in solution. Azimuthally averaged SAXS data collected from 60 nm silica nanoparticles in solution shows Bessel function-like behavior similar to what is expected from perfectly spherical scatterers. Deviations from the expected Bessel function behavior can be explained by slight differences in the shapes and sizes of the particles.

in solution. This is accomplished by introducing a structure factor $S(\vec{q})$ into the intensity relationship for a single scatterer above.

$$I_{SAXS}(\vec{q}) = |\Delta\rho|^2 V_P^2 |F(\vec{q})|^2 S(\vec{q})$$

The structure factor can take many forms depending on the expected interparticle correlations in a sample, but for the purposes of this study we will only consider the aggregation of perfectly spherical scatterers [11]. To illustrate how the structure factor will manifest in SAXS data, consider the scattering profiles of 5 nm particles with increasing volume fraction in figure 4.3. As the volume fraction of scatterers in solution increases and the interparticle spacing decreases, a new peak begins to emerge in the scattering profile at the wavevector transfer corresponding to the interparticle distance. By tracking the location and presence of this peak, we

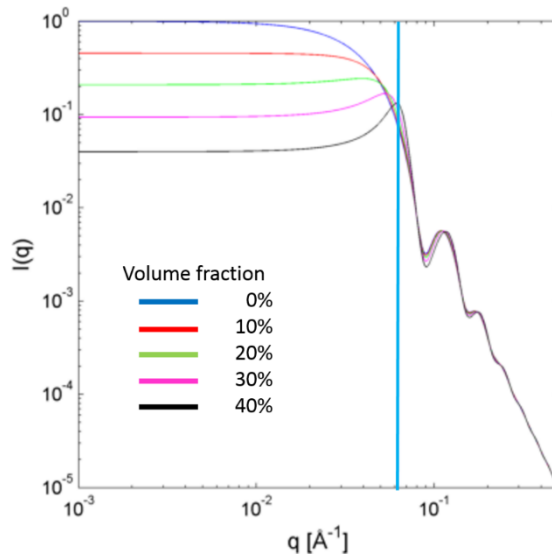


Figure 4.3: An interparticle correlation peak emerges in the SAXS profile as the volume fraction of scattering particles increases. Pictured above are simulated SAXS profiles of 5 nm radius hard spherical scatterers in solution. As the volume fraction of particles in solution increases and individual scatterers begin to “see” their neighbors, a correlation peak emerges in the SAXS profile at the wavevector transfer corresponding to the mean interparticle distance (vertical blue line). Adapted from [29].

can determine the structure and progression of an aggregated state over the course of an experiment; this will prove invaluable in our interpretation of SAXS results involving SSLBs and α -synuclein.

Section 4.2.2: Preparation of synaptic vesicle mimics using spherical-nanoparticle supported lipid bilayers (SSLBs)

With lipids acquired from Avanti Polar Lipids (Alabaster, AL, USA), mixtures of 50 mol% zwitterionic 1,2-dioleoyl-*sn*-glycero-3-phosphocholine (DOPC) and 50 mol% anionic 1,2-dioleoyl-*sn*-glycero-3-phosphate (DOPA) were suspended in chloroform, dried under a stream of nitrogen gas, and placed in a vacuum desiccator for at least an hour to remove residual solvent. After determining the mass via analytical balance, lipid mixtures were rehydrated into sucrose-loaded buffer (10 mM citrate, 150 mM NaCl, 650 mM sucrose, pH 6.0) and shaken for 1 hour at 40 °C to form multilamellar vesicles. The resulting solution was then subjected to five freeze-thaw cycles by alternatively submerging sample vial in a dry ice/ethanol bath and a heated water bath, which produces unilamellar vesicles with a high degree of polydispersity. To reduce the polydispersity, unilamellar vesicles were first pre-extruded through 400 nm pore size membranes (Whatman Nucleopore membrane; 25 mm in diameter) at 50 psi of ultra-high purity argon gas using a Lipex Extruder purchased from Evonik Transferra Nanosciences (Burnaby, BC, Canada). The resulting solution was then extruded again through 80 nm pore membranes at 250 psi to produce unilamellar vesicles with low polydispersity.

Spherical-nanoparticle supported lipid bilayers (SSLBs) were then prepared by rupturing lipid vesicles on nanoparticles via osmotic stress, as previously described [4]. Briefly, amine-

functionalized silica nanoparticles of ~60 nm diameter were purchased in ethanol (Lot # SCM0049) from nanoComposix (San Diego, CA, USA) and dialyzed against 1 L of Milli-Q water overnight to exchange the ethanol for water. Nanoparticles were resuspended into assembly buffer (10 mM citrate, 150 mM NaCl, pH 6.0) and were subsequently mixed with an equal volume of low-polydispersity large unilamellar vesicles. The mismatch of sucrose concentration inside and outside of vesicles drove the rupture and formation of a single lipid bilayer on the nanoparticle substrate. After incubating the nanoparticle-vesicle solution for 1 hour at 40 °C to maximize SSLB formation, excess vesicles were removed via three cycles of sample centrifugation at 1700 g for 15 minutes with resuspension in sample buffer (10 mM HEPES, 100 mM NaCl, pH 7.0). Prior to measurement, SSLB samples were allowed to rest for >6 hours to allow aggregates to settle to the bottom of the tube; the supernatant was removed and used for all experiments in this study.

Section 4.2.3: Protein purification

N-terminal acetylated α -synuclein (α Syn) and α -synuclein with truncated C-terminal domain (α Syn Δ CTD, amino acids 1-101 of α Syn) were bacterially expressed and purified, as previously described [12]. Briefly, pET-21a constructs were transformed into BL21 cells that included a plasmid encoding for an N- α -acetyltransferase [13]. After incubation in LB media at 37 °C until $OD_{600} = 0.6$, cells were induced with 1 μ M isopropyl β -D-1-thiogalactopyranoside and left to incubate for an additional 4 hours. Pelleted cells were resolubilized in 20 mM Tris-HCl, 5 mM EDTA and 1 mM phenylmethanesulfonylfluoride (pH 8.0) and subsequently lysed by ultrasonication for 5 second on/off intervals for 10 minutes at 300 W.

For α Syn purification, the pH of the lysate was adjusted to 3.5 to induce acid precipitation with the addition of 10 M HCl and the sample was subsequently spun down at 20,000 g for 20 minutes. After readjusting the pH of the supernatant to 7.0, ammonium sulfate was added to 50 wt/vol% to induce precipitation before being spun down again at 20,000 g for 20 minutes. Supernatant was then filtered and run through a Superdex 200 10/300 column (GE Healthcare Lifesciences), with protein eluting at ~14.5 mL into sample buffer (10 mM HEPES, 100 mM NaCl, pH 7.0). Protein concentration was measured via NanoDrop (ThermoFisher Scientific) at predicted absorbance (A_{280} coefficient = 5960), aliquoted into single-use vials, frozen with liquid nitrogen and stored at -80 °C until needed.

For α Syn Δ CTD purification, lysate was run through a HiTrap Q FF anion exchange column (GE Healthcare Lifesciences). Due to the cationic nature of the α Syn Δ CTD relative to other lysate constituents, α Syn Δ CTD was eluted in the flow through while other lysate constituents were captured by the column. α Syn Δ CTD was then filtered and run through a Superdex 200 10/300 column (GE Healthcare Lifesciences), with protein eluting at ~14.5 mL into sample buffer (10 mM HEPES, 100 mM NaCl, pH 7.0). Protein concentration was measured via NanoDrop (ThermoFisher Scientific) at predicted absorbance (A_{280} coefficient = 1490), aliquoted into single-use vials, frozen with liquid nitrogen and stored at -80 °C until needed.

Section 4.2.4: SAXS sample prep and PEG-induced depletion protocol

SAXS measurements were performed at beamline 4-2 at the Stanford Synchrotron Radiation Lightsource, SLAC National Accelerator Laboratory at 9 keV with a Si(111) monochromator. Scattering data were taken with a 2D area detector (MarUSA, Evanston, IL, USA)

with a sample-to-detector distance of ~3.5 m. Beampath length and detector were calibrated with a silver behenate control, with beam size approximately 150 μm (vertical) x 200 μm (horizontal).

For PEG-induced depletion experiments, appropriate concentrations of protein, polyethylene glycol (MWC = 10,000, or PEG10k), and divalent ions suspended in sample buffers were added to 20 μL of SSLB samples (corresponding to 2 mg/mL of nanoparticles) to a total volume of 50 μL. Osmotic pressure induced as a function of PEG10k concentration was calculated using the formula,

$$P = RT \left(10 * \frac{PEG10k \frac{wt}{vol} \%}{MW \text{ of } PEG10k} + 1.4 * 10^{-4} * \left(PEG10k \frac{wt}{vol} \% \right)^2 + 2 * 10^{-5} * \left(PEG10k \frac{wt}{vol} \% \right)^3 \right)$$

where R is the universal gas constant, T is the temperature in Kelvin, and the prefactors before the exponential terms are the second and third virial coefficients for PEG10k determined empirically [14]. Prepared samples were loaded into 1.5 mm quartz capillaries (Hampton Research, Aliso Viejo, CA, USA), sealed with epoxy, and allowed to equilibrate at 37 °C for 6 hours before being loaded into a custom-designed sample oven for subsequent SAXS measurements.

Section 4.3: Results

Section 4.3.1: The C-terminal domain is responsible for dispersing synaptic vesicle mimics

Previous experiments conducted in the Lee lab revealed that both wild-type and C-terminal truncated versions of αSyn stably bound to synaptic vesicle-mimetic SSLBs with roughly comparable affinity (92 and 42 μM, respectively) [7]. To reflect *in vitro* and *in vivo* data showing

that the surface-bound amount of α Syn is relatively small [15, 16], we selected a 1:80 protein:outer lipid ratio for all of our experiments, which has previously been shown not to disrupt the SSLBs [7]. To probe the force response of the steric stabilization afforded by α Syn at this protein:outer lipid ratio, we used SAXS to investigate the higher-order aggregate structure of α Syn-bound SSLBs as PEG10k was titrated into the system to induce depletion-attraction [17]. The azimuthally-averaged line shape of the α Syn-bound SSLBs displayed a correlation peak at $q \approx 0.0092 \text{ \AA}^{-1}$, consistent with the expected nearest-neighbor distance between a pair of bare SSLBs; this peak only emerged upon the addition of 10.5 wt/vol% PEG or more (figure 4.4). The presence of such a peak suggests that any repulsive potential between α Syn-bound SSLBs was overcome by depletion-attraction forces at sufficient PEG concentration.

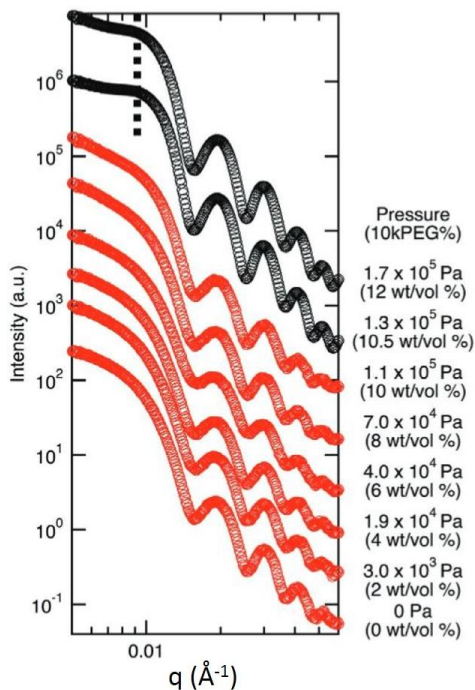


Figure 4.4: α Syn-SSLBs remain dispersed in solution until a critical concentration of osmotic depletant is added. Pictured above are the azimuthally averaged SAXS profiles obtained from α Syn-SSLBs as PEG10k was titrated into the system. Upon the addition of 10.5 wt/vol% PEG10k or more (black curves), a correlation peak emerges at a wavevector transfer $q \approx 0.0092 \text{ \AA}^{-1}$ corresponding to an average interparticle distance of $\sim 68 \text{ nm}$, which is approximately the size of a single SSLB. As a pair of non-interacting hard spheres would usually be expected to cluster at lower osmotic pressures, the α Syn-bound SSLBs can be described as a sterically stabilized colloid.

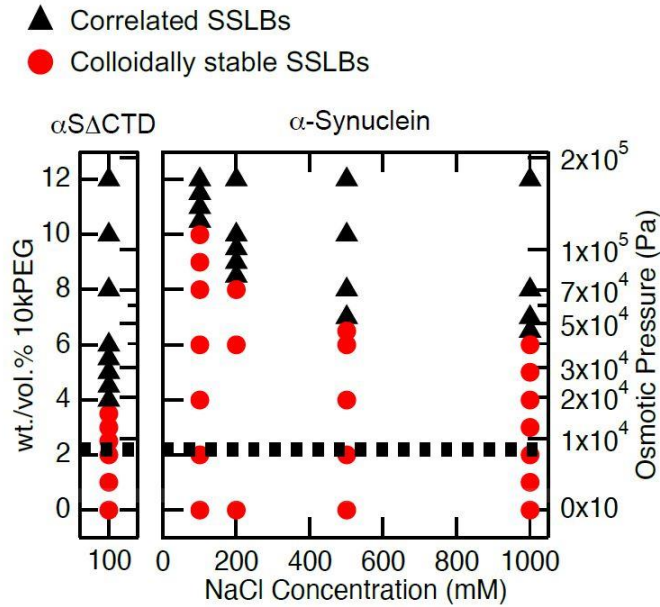


Figure 4.5: The critical osmotic pressure required for clustering α Syn-SSLBs changes as a function of protein length and electrostatic screening. The same PEG10k titration was performed for both α Syn Δ CTD-SSLBs in normal sample buffer (10 mM HEPES, 100 mM NaCl, pH 7.0) and α Syn-SSLBs in buffer containing increasing amounts of monovalent salt. **(Left):** α Syn Δ CTD-SSLBs were found to cluster at a critical osmotic pressure seven times lower than their full-length counterparts under the same conditions. While this reduction is significant, the critical clustering pressure remains roughly twofold higher than the pressure expected to cluster non-interacting hard spheres of similar size. **(Right):** as the amount of monovalent salt in solution increased, α Syn-SSLBs were found to cluster at lower and lower pressures; black triangles represent SAXS scans featuring an interparticle correlation peak, while red circles represent SAXS scans with no correlation peak present. The decrease in critical clustering pressure as monovalent salt concentration increases indicates that electrostatics play some role in the steric stabilization of α Syn-SSLBs.

A pair of non-interacting 70 nm diameter colloids similar to SSLBs would be expected to associate at a depletion-induced effective pressure of $P_C \approx 4 \times 10^3$ Pa; comparing this expected value to the experimentally observed critical pressure for clustering α Syn-bound SSLBs ($P_C \approx 1.3 \times 10^5$ Pa), it becomes clear that α Syn introduces a strong repulsive potential between neighboring SSLBs which could have physiological significance [18]. Furthermore, in comparing the depletion-attraction response of the SSLB-bound α Syn to its C-terminal truncated counterpart, one can clearly see that this strong repulsive potential likely arises from the steric repulsion of the C-

terminal domain, which is hypothesized to project off of a membrane surface due to its high negative charge [19]. When the same PEG10k titration experiments were performed with α Syn Δ CTD, the aforementioned interparticle correlation peak emerged at a much lower PEG concentration than for the wild-type protein; a total of 4 wt/vol% PEG10K, corresponding to a depletion pressure of 1.9×10^4 Pa, was required to cluster α Syn Δ CTD-bound SSLBs (figure 4.5). Taken together with the wild-type SAXS profiles, these data suggest that the C-terminal tail is in fact responsible for the nearly seven-fold difference in critical clustering pressure.

Section 4.3.2: Electrostatics and steric contributions both play a role in steric stabilization

To further elucidate the factors contributing to the changes in critical clustering pressure, we elected to explore the system's response to increased electrostatic screening. By increasing the concentration of monovalent salt (NaCl) in solution and performing the same PEG10k titration, we could effectively remove the electrostatic contributions to the repulsive force preventing clustering; a phase diagram summarizing the results of these experiments is shown in figure 4.5, (right panel). As our intuition suggested, the salt phase diagram clearly demonstrates a reduction in the critical clustering pressure for α Syn-bound SSLBs as a function of increasing NaCl concentration. At 1M NaCl, where the Debye length is of the same order as the distance between neighboring amino acids in a protein, we found that a critical pressure of $P_C = 4.6 \times 10^4$ Pa resulted in SSLB clustering, which is roughly three-fold lower than the critical pressure required for clustering in 0.1 M NaCl. Additionally, though increasing the NaCl concentration resulted in a reduction of the α Syn critical clustering pressure, we were not able to reproduce the critical clustering pressure of α Syn Δ CTD with salt alone; at 1M NaCl, the critical clustering pressure for α Syn-SSLBs is still roughly two-fold higher than the pressure required to cluster α Syn Δ CTD-

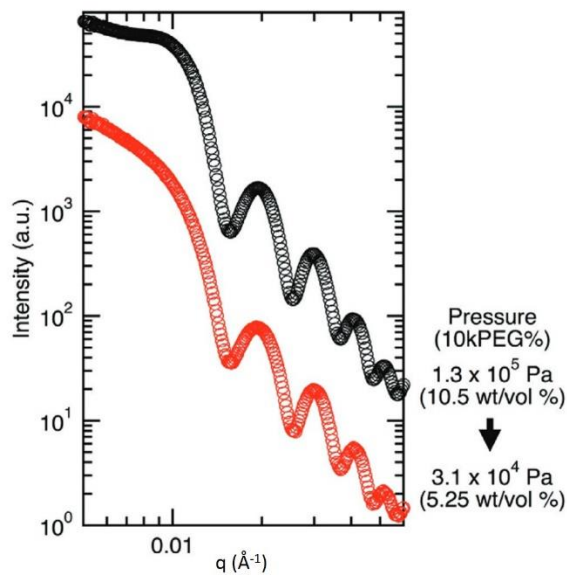


Figure 4.6: Dilution experiments demonstrate that the clustering of α Syn-SSLBs is reversible. To determine whether the depletion attraction-induced clustering of α Syn-SSLBs was reversible flocculation or irreversible aggregation, we diluted the concentration of PEG10k twofold with buffer in a sample displaying inter-SSLB correlation. Suppression of the correlation peak upon PEG10k dilution suggests that previously clustered α Syn-SSLBs disperse and we are observing reversible flocculation.

SSLBs. The large difference in these two measurements suggests that the repulsive force between α Syn-SSLBs has both electrostatic and steric components.

With salt data in hand, we then aimed to explore the nature of the steric component to the α Syn-SSLB repulsive force. We hypothesized that steric repulsion emerges from the polymeric behavior of the C-terminal domain, as it has been shown to only loosely associate with a membrane when the rest of the protein is stably bound [19]. To test this hypothesis, we performed a series of experiments aimed at determining the reversibility of α Syn-SSLB clustering; in these experiments, we would first induce clustering in a sample in normal buffer conditions (i.e., 100 mM NaCl) before subsequently diluting the sample by a factor of two with more buffer. While clustering in these samples was initially evidenced by the emergence of the inter-SSLB correlation peak, this

peak disappeared when the sample was diluted with more buffer, indicating that the depletion-induced clustering process was indeed reversible (figure 4.6). The reversibility of the clustering process is consistent with similar observations of non-specific steric repulsion in grafted polymers on opposing surfaces, and demonstrates the power of incorporating polymer research into biophysical studies [20, 21].

Section 4.3.3: Divalent ions alter the force response behavior of synaptic vesicle mimics in the presence of α Syn

Given the wide breadth of literature that suggests the C-terminal domain of α Syn can weakly bind divalent cations [3, 22, 23], we elected to examine the impact of such ions on the force response of α Syn-SSLBs. In particular, Ca^{2+} ions have been shown to be a physiologically

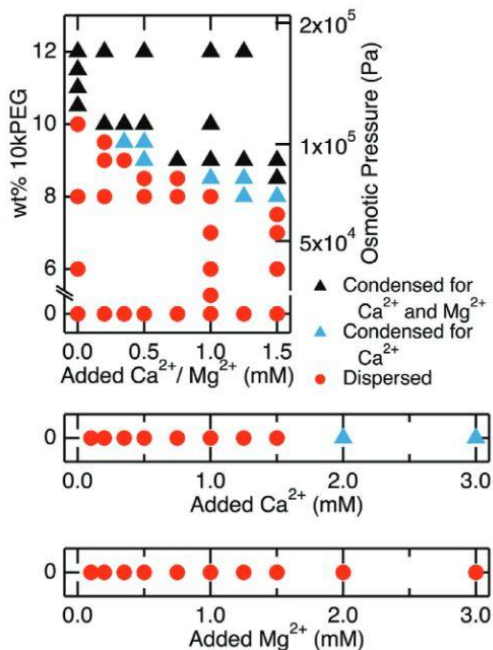


Figure 4.7: Depletion attraction-induced clustering is enhanced with small amounts of divalent ions in solution. (Top): The inclusion of either Ca^{2+} or Mg^{2+} ions in solution resulted in a global decrease in the critical osmotic pressure required to induce α Syn-SSLB clustering, but this effect was more pronounced for Ca^{2+} . **(Middle):** At millimolar concentrations of added Ca^{2+} , α Syn-SSLBs were found to cluster without the addition of PEG10k. **(Bottom):** A similar effect was not observed for Mg^{2+} without osmotic depletion.

relevant binding partner for α Syn due to the role of calcium signaling in neuronal signal transduction, despite their relatively weak affinity [3, 24]. In the context of our experiments, we hypothesized that calcium and other divalent ions would have the propensity to associate with the C-terminal tail and result in a reduced critical clustering pressure, as the negatively charged residues in the tail will be locally screened by the associated ions. Our SAXS experiments supported this hypothesis and revealed a modest decrease in the critical clustering pressure when either Ca^{2+} or Mg^{2+} was added to the sample, with calcium demonstrating the stronger effect of the two (figure 4.7). Additionally, we discovered that adding 2 mM Ca^{2+} to α Syn-SSLBs in the *absence* of PEG10k still produced a measurable interparticle correlation peak while no such peak appeared for similar concentrations of Mg^{2+} . To further explore this phenomenon, we replicated the reversibility experiments discussed in the last section with 3 mM Ca^{2+} in solution and found that dilution post-clustering did **not** remove the inter-SSLB correlation peak (figure 4.8); this suggests that calcium ions have the ability to coordinate the C-terminal domains on opposing membrane surfaces and may trigger similar behavior *in vivo*.

Section 4.4: Significance of α Syn's C-terminal domain in physiology and pathology

While the C-terminal domain of α Syn has long been implicated in the pathophysiology of Parkinson's disease and other synucleinopathies, there is limited literature precedent elucidating its physiological function. Previous studies have mostly explored the potential for the C-terminus to act as a solubilizing chaperone or oligomerization inhibitor for the central non-amyloid β component (NAC) region of the protein, suggesting that the C-terminus has no intrinsic function on its own [2, 25, 26]. Others have posited that similar to the N-terminal domain, which only adopts an α -helical structure upon binding to membranes, the intrinsic disorder of the C-terminal

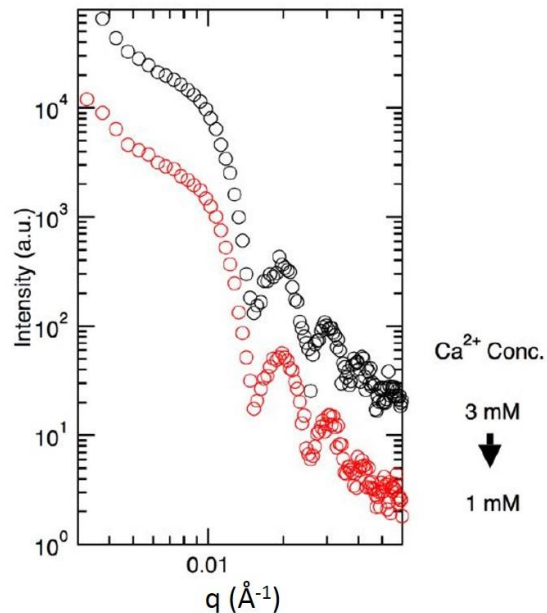


Figure 4.8: Calcium-induced clustering of α Syn-SSLBs without osmotic depletant is not reversible. Dilution of a sample containing 3 mM Ca^{2+} with buffer does not cause the inter-SSLB correlation peak to disappear, which suggests that calcium ions may be coordinated between the C-terminal domains of α Syn bound to opposing membranes.

domain may be physiologically irrelevant and disappear upon finding its own corresponding substrate. While these ideas deserve merit, it feels heavy-handed and extrapolatory to assume that the C-terminal domain does not play a role in the normal physiological behavior of α Syn.

Findings from our study have instead led us to propose that the C-terminal domain utilizes its persisting intrinsic disorder to affect the interaction potential near lipid membrane surfaces. Numerous lines of evidence presented here suggest that the C-terminal domain of α Syn behaves as a grafted polyelectrolyte on the surface of SSLBs. The high critical osmotic pressure at which clustering occurs (figure 4.4) and the reversibility of the clustering (figure 4.6) for α Syn-SSLBs are consistent with polymers on opposing surfaces that entropically do not want to interpenetrate. The decrease in and disappearance of critical osmotic pressure upon the increase in monovalent salt (figure 4.5) and calcium ions (figure 4.7), respectively, are consistent with established

literature on the behavior of grafted polyelectrolytes [5, 27]. Indeed, the aforementioned ability for the C-terminal domain to behave as a solubilizing chaperone should just as well apply for α Syn in solution as it does when α Syn is bound to a membrane surface; the same properties that allow the C-terminus in solution to prevent protein-protein contacts prior to α Syn oligomerization are the very same properties that inhibit SSLB-SSLB contacts in the experiments described here.

Intriguingly, the utilization of the C-terminal domain's intrinsic disorder to affect the force response of membrane surfaces has implications for both post-translational modifications of α Syn and differences within the synuclein family of proteins. First, the electrostatic component observed in steric stabilization of membranes by α Syn should only increase with increasing charge to a first-order approximation. The C-terminal domain of α Syn is often dynamically phosphorylated, with phosphorylation of Serine-129 being the most implicated post-translational modification in Parkinson's disease; as phosphorylation adds a divalent (i.e., charged) phosphate group to an amino acid, this post-translational modification could impact the electrostatic component contributing to inter-vesicle repulsion. An exciting avenue of inquiry would be to biophysically link post-translational modifications of α Syn to its force response on membrane surfaces, which could manifest as a cellular ability to "reprogram" surface interactions via intrinsically-disordered proteins.

Second, the major distinction between different synucleins is not in the conserved, membrane-binding region of synucleins but in the divergent C-terminal domains [28]. Compared to the α Syn C-terminal domain the β -synuclein C-terminal domain is slightly longer while exhibiting a similar charge density, and the γ -synuclein C-terminal domain is shorter while

exhibiting a much lower charge density. Should the force response of β - and γ -synuclein on membrane surfaces differ in concordance with polymer theory, such findings would not only elucidate the biophysical role of each synuclein isoform but also serve as a fascinating example by which evolution has tuned an interaction by adjusting the polymeric properties of a protein.

Section 4.5: References

- [1] Clayton, D. F. & George, J. M. *Journal of Neuroscience Research* **58**, 120–129 (1999).
- [2] Park, S. M. *et al. Journal of Biological Chemistry* **277**, 28512–28520 (2002).
- [3] Lautenschläger, J. *et al. C-terminal calcium binding of α -synuclein modulates synaptic vesicle interaction. Nature Communications* **9**, 712 (2018).
- [4] Chung, P. J., Hwang, H. L., Dasbiswas, K., Leong, A. & Lee, K. Y. C. *Langmuir* **34**, 13000–13005 (2018).
- [5] Chung Peter J. *et al. Proceedings of the National Academy of Sciences* **112**, E6416–E6425 (2015).
- [6] Chung, P. J. *et al. Nature Communications* **7**, 12278 (2016).
- [7] Chung, P. J. *et al. ACS Appl. Bio Mater.* **2**, 1413–1419 (2019).
- [8] Pedersen, J. S. *Advances in Colloid and Interface Science* **70**, 171–210 (1997).
- [9] Jones, M. R. *et al. Nature Materials* **9**, 913–917 (2010).
- [10] Tong, D., Yang, S. & Lu, L. *Journal of Applied Crystallography* **49**, 1148–1161 (2016).
- [11] Larsen, A. H., Pedersen, J. S. & Arleth, L. *Journal of Applied Crystallography* **53**, 991–1005 (2020).
- [12] Coelho-Cerqueira, E., Carmo-Gonçalves, P., Sá Pinheiro, A., Cortines, J. & Follmer, C. *The FEBS Journal* **280**, 4915–4927 (2013).
- [13] Johnson, M., Coulton, A. T., Geeves, M. A. & Mulvihill, D. P. *PLOS ONE* **5**, e15801 (2010).
- [14] Cohen, J. A. & Highsmith, S. *Biophys J* **73**, 1689–1694 (1997).
- [15] Pfefferkorn, C. M. & Lee, J. C. *J. Phys. Chem. B* **114**, 4615–4622 (2010).
- [16] Fakhree, M. A. A. *et al. Scientific Reports* **6**, 30658 (2016).
- [17] Kuhl, T. *et al. Langmuir* **12**, 3003–3014 (1996).
- [18] Park, K., Koerner, H. & Vaia, R. A. *Nano Lett.* **10**, 1433–1439 (2010).
- [19] Eliezer, D. *Journal of Molecular Biology* **425**, 2393–2396 (2013).

- [20] Björkegren, S. M. S., Nordstierna, L., Törnecrona, A., Persson, M. E. & Palmqvist, A. E. C. *Journal of Colloid and Interface Science* **452**, 215–223 (2015).
- [21] Israelachvili, J. *Intermolecular and Surface Forces*. Elsevier Inc. (2011).
- [22] Binolfi, A. *et al. J. Am. Chem. Soc.* **128**, 9893–9901 (2006).
- [23] Lowe, R., Pountney, D. L., Jensen, P. H., Gai, W. P. & Voelcker, N. H *Protein Science* **13**, 3245–3252 (2004).
- [24] Brini, M., Calì, T., Ottolini, D. & Carafoli, E. *Cellular and Molecular Life Sciences* **71**, 2787–2814 (2014).
- [25] Fink, A. L. *Acc. Chem. Res.* **39**, 628–634 (2006).
- [26] Li Wenxue *et al. Proceedings of the National Academy of Sciences* **102**, 2162–2167 (2005).
- [27] Zhulina, E. B., Borisov, O. V. & Birshtein, T. M. *Macromolecules* **32**, 8189–8196 (1999).
- [28] George, J. M. *Genome Biol* **3**, REVIEWS3002–REVIEWS3002 (2002).
- [29] Lee, B. SAXS/GISAXS principles <https://sites.google.com/site/byeongdu/saxsgisaxs-principles/2-assembly-of-particles?authuser=0> (Accessed March 2, 2022).

CHAPTER 5.
QUANTITATIVE ANALYSIS OF TOTAL REFLECTION X-RAY FLUORESCENCE
FROM FINELY LAYERED STRUCTURES USING XERAY

Section 5.1: Overview

Total reflection x-ray fluorescence (TXRF) is an experimental technique used to study the distribution of chemical elements among finely-layered structures with a high degree of precision and sensitivity. Though extremely powerful, TXRF as a technique remains out of reach for many researchers due to both the difficulty of producing high-intensity x-rays and the steep learning curve required for accurate and robust data analysis. In an attempt to address this latter problem, we have developed a MATLAB-based software package with a simplified graphical user interface, named *XeRay*, for fast, accurate, and intuitive analysis of TXRF data. *XeRay* allows a user to model any finely-layered system with independent chemical composition and thickness information for each layer in addition to offering fine-tuned data fitting. The accuracy of *XeRay* has been tested in the analysis of TXRF data obtained from both air/fluid and fluid/fluid interfaces, and has produced fit results in good agreement with the associated published studies. In this chapter, I will discuss the theory of TXRF, explain the structure of the *XeRay* program, and provide evidence for the accuracy of *XeRay* using two published case studies.

Section 5.2: Background

Finely-layered structures are essential building blocks for both artificial and biological systems. In artificial systems such fine structures often serve as a fundamental design pattern [3], giving rise to things like thin-layered polymer films [4], silicon wafers and computer chips [5], heavy metal ion extraction systems [6], and a wide range of substrates for surface catalysis and

localized chemistry [7]. In biology, researchers have found that lipid membranes can also manifest finely-layered structures via the recruitment of a variety of membrane-binding proteins [1] and messenger metal ions like Ca^{2+} [2], both of which can participate in intracellular functions and signaling events. Despite their ubiquitous nature though, much remains unknown about the functional consequences of how finely-layered systems are organized.

To better understand the impact of how layered structures are organized, it is important to explore the distribution of chemical elements within the layers as such information can provide critical insight into their macroscopic behavior. X-ray fluorescence is an ideal tool for studying such elemental distributions because it is relatively nondestructive and nonintrusive. In addition, x-rays have the added benefit of being able to probe condensed matter on the order of sub-nanometers to a few hundred micrometers in thickness [8,9], allowing for a wide variety of systems to be studied. First described by Yoneda and Horiuchi [10], total reflection x-ray fluorescence (TXRF) has become a commonly used method for quantitatively determining the distribution of metal ions and other elements across all kinds of finely-layered structures. The versatility of TXRF is manifested in the diversity of systems that it has been able to probe, including Langmuir monolayers [11-13], biological membranes [14], membrane-binding proteins [15,16], and biological tissues [18,19], to name a few. In recent decades, there has also been an increase in usage of TXRF due to increased accessibility of synchrotron light sources [22-24], which allow for greatly enhanced measurement precision and significantly lowered signal detection limits.

The high sensitivity of TXRF to interfacial elements can be attributed to the interaction between x-rays and the electrons of the substrate of interest. Due to their relatively high frequency

x-rays are capable of producing a refractive index smaller than unity; this gives rise to a critical angle below which an incident beam will experience total reflection and create a standing evanescent wave at the substrate interface without significantly penetrating into the sample. Conversely, above the critical angle x-rays largely bypass the interface and penetrate into the electron-rich medium below. Thus, x-rays can be uniquely tuned to probe both the interfacial and bulk elemental composition of a substrate; this forms the basis for using TXRF as a tool to detect chemical enrichment at an interface.

In addition to its high sensitivity to trace amounts of elements, TXRF has the added benefit of being largely nonintrusive and nondestructive compared to electron or other molecular beams. In TXRF the excitation energy is generally kept far away from the absorption edge of the element of interest so that the fluorescence intensity is proportional to the density of the element. The opposite is true of x-ray absorption near edge spectroscopy (XANES), in which the x-ray energy is changed while fixing the incidence angle; this technique provides detailed information on the valence states of the elements of interest and thus can be viewed as complementary to TXRF [25,26].

Given TXRF's unique ability to elucidate elemental distributions at interfaces, we have developed an intuitive MATLAB-based software package, called *XeRay*, to analyze TXRF data and to make TXRF more accessible to the scientific community. To test *XeRay*, we designed an experiment intended to measure Ca^{2+} accumulation beneath an anionic SOPA (1-stearoyl-2-oleoyl-*sn*-glycero-3-phosphatidic acid) monolayer sitting atop a Langmuir trough. Analysis of the data using *XeRay* revealed an approximate 1:1 stoichiometry between the anionic SOPA

headgroups and the cationic Ca^{2+} ions. Additionally, we have used *XeRay* to analyze a dataset on Sr^{2+} sequestration at the dodecane/surfactant/fluid interface from a previously published report [17]. Results from both analyses obtained from *XeRay* are consistent with values previously published, and demonstrate the power this program can have in streamlining TXRF data analysis.

Section 5.3: Theory of Total Reflection X-ray Fluorescence (TXRF)

X-rays, like all light, have the ability to excite atoms from their ground state to higher electronic states. The relaxation of such excited states causes the atom to fluoresce, producing unique energy peaks depending on the identity of the atom of interest. For example, calcium has a characteristic $\text{K}\alpha$ line at 3.7 keV and $\text{K}\beta$ line at 4.0 keV, whereas strontium has a $\text{K}\alpha$ line at 14.2 keV and an $\text{L}\alpha$ line at 1.8 keV; all elements heavier than sodium can produce such characteristic fluorescence decays, which provide a framework to understand the elemental composition of an interface. To obtain analytical closed-form solutions, the interfaces are assumed to be perfectly sharp, and all layers are assumed to be homogenous in composition. The interaction of x-rays with each layer is, to a good approximation, described by classical optics considerations. For each layer, the refractive index is described by

$$n = 1 - \delta + i\beta$$

where n is the index of refraction, and δ and β represent the dispersive and absorptive aspects of light interacting with matter. δ and β can be calculated additively from the absorption and dispersion properties of each elemental component I in the system, with the dispersion

$$\delta = \sum_i \frac{N_A}{2\pi} r_e \lambda^2 \frac{Z_i}{M_i} \rho_i$$

and the absorption

$$\beta = \sum_i \frac{\lambda}{4\pi} \mu_i$$

where N_A is Avogadro's number, r_e is the classical radius of the electron, λ the wavelength of incident x-rays, Z_i the atomic number, M_i the atomic mass, ρ_i the mass density, and μ_i the linear mass absorption coefficient. Here we use the database of the mass absorption coefficients of 92 elements from the periodic table with energies ranging from 30 eV to 30 keV [27]. Typically for condensed matter phases δ and β are much smaller than unity, with δ on the order of 10^{-6} and β on the order of 10^{-9} . The reader is encouraged to turn to a textbook such as Ref. [18], for a more complete explanation and treatment of these terms.

To calculate fluorescence induced by an x-ray, we adopted a previously developed matrix method [28,29]. First, we assume the system is comprised of $N + 1$ ($N \geq 1$) layers, the top, layer 0, being the infinite medium through which the x-rays arrive and the bottom, layer $N + 1$, being the infinite medium through which the x-rays leave the sample of interest. The refraction angle between two adjacent layers is related by Snell's law

$$\theta_{n+1} = \sqrt{\theta_n^2 - 2(\delta_{n+1} - \delta_n) + 2i(\beta_{n+1} - \beta_n)}$$

Deriving from Snell's law and the Fresnel relations, the incidence and reflection amplitudes between two adjacent layers are related by

$$\begin{pmatrix} A_n^t \\ A_n^r \end{pmatrix} = \begin{pmatrix} m_{11} & m_{12} \\ m_{21} & m_{22} \end{pmatrix} \begin{pmatrix} A_{n+1}^t \\ A_{n+1}^r \end{pmatrix}$$

where the matrix elements are given by

$$\begin{aligned}
 m_{11} &= \frac{\theta_n + \theta_{n+1}}{2\theta_n} \exp\left(-i\frac{\pi}{\lambda}(\theta_n d_n + \theta_{n+1} d_{n+1})\right), \\
 m_{12} &= \frac{\theta_n - \theta_{n+1}}{2\theta_n} \exp\left(-i\frac{\pi}{\lambda}(\theta_n d_n - \theta_{n+1} d_{n+1})\right), \\
 m_{21} &= \frac{\theta_n - \theta_{n+1}}{2\theta_n} \exp\left(i\frac{\pi}{\lambda}(\theta_n d_n - \theta_{n+1} d_{n+1})\right), \\
 m_{22} &= \frac{\theta_n + \theta_{n+1}}{2\theta_n} \exp\left(i\frac{\pi}{\lambda}(\theta_n d_n + \theta_{n+1} d_{n+1})\right)
 \end{aligned}$$

where d_n denotes the thickness of the layer n , and λ is the wavelength of the incident x-ray beam.

The relation between the amplitudes of the first layer and the last is

$$\begin{pmatrix} 1 \\ A_0^r \end{pmatrix} = \sum_{n=1}^N M_n \begin{pmatrix} A_n^i \\ 0 \end{pmatrix},$$

where two boundary conditions are used as follows: the amplitude of the incident beam is assumed to be 1 and the reflection amplitude coming from the bottom layer is 0. This equation enables us to solve for all the other amplitudes for the layers in between.

The decay of the incident beam and the excited fluorescence is characterized by a penetration depth at which the intensity decays to $1/e$ of the original incident intensity. For the incident wave at layer n , the penetration depth is

$$\Lambda_n^i = \frac{\lambda_i}{4\pi \text{Im}(\theta_n)},$$

where the superscript or subscript i refers to the incident excitation wave. For the fluorescence wave, the treatment can be greatly simplified as it has an incidence angle close to $\pi/2$ which is far larger than the critical angle; thus reflection can be ignored. The penetration depth of the fluorescence beam is

$$\Lambda_n^f = \frac{\lambda_f}{4\pi\beta_n^f},$$

where the superscript or subscript f refers to the fluorescence wave.

Having calculated the amplitudes of the transmission and reflection waves at each layers, and the penetration depths, the intensity of the excited fluorescence for each layer at position z is

$$I_n(z) = \exp\left(-\sum_{m=0}^{n-1} \frac{d_m}{\Lambda_m^i}\right) * \exp\left(-\frac{z - z_n}{\Lambda_n^i}\right) * |A_n^t \exp(ik\theta_n z) + A_n^r \exp(-ik\theta_n z)|^2.$$

The fluorescence intensity originating from layer n is described by

$$F_n = C_0 c_n \exp\left(-\sum_{m=0}^{n-1} \frac{d_m}{\Lambda_m^f}\right) \int_{z_n}^{z_{n+1}} I_n(z) \exp\left(-\frac{z - z_n}{\Lambda_n^f}\right) dz,$$

where C_0 is the scale factor that characterizes the geometry of the setup and the quantum efficiency of the excitation, c_n the concentration of the excited element, and z_n the position at which layer n begins. The total fluorescence intensity is then calculated as a sum over all layers

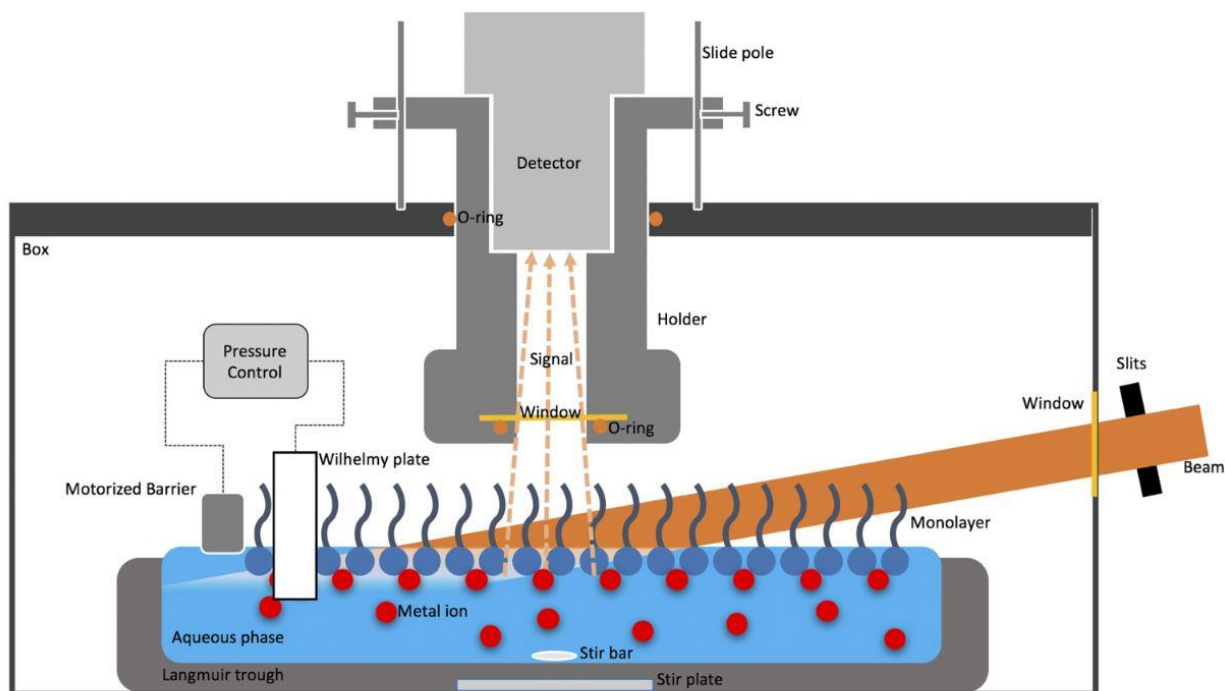


Figure 5.1: Schematic of the air/liquid TXRF setup. A Langmuir trough designed for surface scattering experiments is fully enclosed in an airtight box, with a novel detector holder fitted into the lid. A Kapton window and silica gel O-ring are used to seal the inward face of the detector holder, while a separate silica gel O-ring embedded in the lid of the box allows the user to adjust the distance between the detector holder and the liquid surface while keeping the box airtight. The liquid-facing end of the detector holder also has a thin tube measuring 10 mm in diameter (slightly larger than the 8 mm opening on the detector), which effectively acts as a collimator to attenuate the detection area on the liquid surface. The detector is mounted into the holder in an upright configuration. As is the case with many other Langmuir troughs, the surface tension/pressure is monitored and controlled by a feedback loop consisting of a Wilhelmy plate and a motorized barrier. For illustration purposes the barrier and Wilhelmy plate are drawn in the same plane as the beam, while they actually reside on different planes in the instrument.

$$F_0 = \sum_{n=1}^N F_n.$$

Note that the top layer ($n = 0$) is ignored in the sum because even if it were to contain any fluorescent elements, the x-ray would not be able to penetrate through this infinite layer.

Section 5.4: Methods

Section 5.4.1: Protocol for running TXRF experiments on Langmuir monolayers at the air/fluid interface

To demonstrate how a TXRF experiment is carried out, here I describe our air/fluid interface experimental setup and procedure. Similar studies can be conducted on any flat interface involving gaseous or condensed phases as well. As seen in figure 5.1, the experimental setup for air/fluid experiments includes three major parts: (1) a liquid surface x-ray spectrometer system that controls the geometry and intensity of the incident x-rays that hit a horizontal stage, (2) a Langmuir trough with stirring capability and a surface pressure control system, featuring a feedback loop composed of a Wilhelmy plate and a motorized barrier, all enclosed in an air-tight box filled with helium, and (3) an energy-resolved x-ray detector mounted via an air-tight and height-adjustable holder overhanging the surface. The air-tight helium-filled box serves to minimize oxidative damage to the interface of interest and reduces x-ray scattering by the more electron-dense nitrogen and oxygen in the air.

For Langmuir monolayers, quantification of an element bound to the fluid/lipid interface is of great interest to researchers [8]. First, the scale factor, which describes the excitation efficiency and particular geometry of the system, is determined via a calibration process, whereby x-ray fluorescence data are collected from a solution without a monolayer and with a known bulk concentration of the desired element. Data are then collected from the experimental system of interest with the insoluble monolayer present and fitted to yield the surface concentrations.

Section 5.4.2: Explanation of the XeRay tool and improvements over traditional data analysis methods

XeRay is an x-ray fluorescence analytical package with a graphical user interface (GUI) under the MATLAB environment. The MATLAB platform was chosen because of its popularity with scientific applications in academia and industry, cross-platform support, backward compatibility with earlier functions, and superb data manipulation capabilities. *XeRay* allows for individual spectral inspection of different elements, fits emission peaks to single or double Gaussian or Lorentzian line shapes, and fits the integrated fluorescence intensity over an incident angle range. If there exists a parallel pool of processors for MATLAB, which can be easily set up, computations in the fitting processes are efficiently parallelized into this pool of CPU cores. The program uses a combination of a brute force search and a trust region reflective (TRR) method [20] in the MATLAB *lsqnonlin* optimization function to search through the parameter space to obtain the fits and χ^2 values, defined as

$$\chi^2 = \sum_i \frac{(\hat{y}_i - y_i)^2}{\delta y_i},$$

where \hat{y}_i is the fitted fluorescence signal, y_i is the signal, and δy_i is the error of the signal.

XeRay uses the chemical formula for each layer to calculate the refractive index. If a chemical formula is not provided, the absorption term β is assumed to be 0 and the dispersion term δ is approximated by

$$\delta = \frac{\lambda^2 r_e}{2\pi} \rho_e,$$

where ρ_e is the electron density. Thus, using a chemical formula that matches the composition of a layer would improve the accuracy of fitting results.

The parameter space determining a fluorescence intensity vs. angle curve is composed of $N + 2$ parameters for a system made of N ($N \geq 2$) layers. *XeRay* assumes that the thickness of each layer is given; thickness information could come from hypotheses, design specifications, and physical measurements such as those from x-ray reflectivity and electron microscopy. The first three parameters are the aforementioned scale factor, a term describing the background noise, and an angle offset value. The purpose of fitting the angle offset is to account for the systematic error from the motor system moving to the desired angles in an experiment. The background comes from the presence of the element of interest in places not considered by the modeled system, such as in the absorbers used to attenuate the x-ray beam and the collimator used before the detector. The background is assumed to be constant due to the empirical observation that it is usually scattered around some mean value within the small energies where an excitation peak occurs, in either control experiments or samples of interest. The background can either be fitted or be fixed to the average fluorescence intensity from a control sample without the element of interest across the same range of angles, which is similar to the blank subtraction method used in a published iron x-ray fluorescence study [26]. The remaining $N - 1$ parameters are the concentrations of the element of interest in each layer excluding the top layer. The concentrations should conform to the unit of the user's choice, which could be in number or moles per unit volume, to name a few. To narrow the search space for fitting, as much physical intuition about the system as possible should be used. For example, if a given layer is devoid of the element of interest, the concentration of that element should be set to 0.

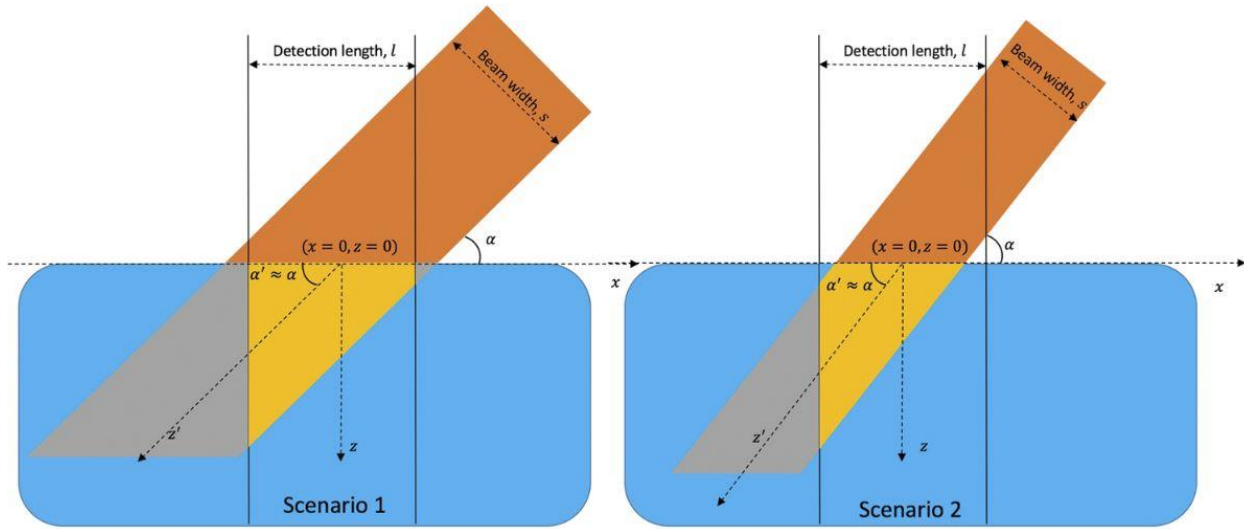


Figure 5.2: Two integration scenarios of the x-ray fluorescence signal. (Left): The incidence beam footprint is larger than the detection length. **(Right):** The incidence beam footprint is smaller than the detection length. In both scenarios, s represents the width of the incident beam, α is angle of incidence, and l is the detection length of the detector. The x -axis is assumed to be horizontal from left to right, with the z -axis perpendicular to the air/liquid interface and the y -axis perpendicular to the resulting x - z plane. Additionally, a z' -axis is assumed to follow the propagation direction of the transmitted beam. The yellow regions represent the area of the sample from which fluorescence signal can be detected.

The geometry of the system is accounted for with two important inputs: the detection length of the detector and the slit size of the incident beam. The software assumes the beam is centered around the detection length. Depending on the relative magnitude of the detection length and the slit size of the incident beam, the entire detection area could be fully or partially utilized, as illustrated in figure 5.2. These two scenarios, which consider the size of the footprint of the incident x-ray beam, are also accounted for in the calculations.

XeRay uses a “likelihood” approach to estimate errors of the fitting parameters, instead of the reduced χ^2 that is often used [30]. The likelihood of a set of parameter values being real is equivalent to the Bayesian probability of the fitting curve such parameters produce given the observed data. This likelihood is closely linked to χ^2 , wherein increasing χ^2 values are associated

with diminishing likelihoods. In fact, the likelihood of a fit being the true fit is proportional to $\exp(-\chi^2/2)$ under two key assumptions: (1) the model is appropriate, and (2) the fitting error behaves as a normal distribution. Both assumptions are proper in our context of gathering data by counting photons and fitting data to properly derived equations. Thus,

$$Likelihood \propto \exp\left(-\chi^2/2\right).$$

The program generally runs three fitting procedures for a given set of parameters. The first procedure runs an optimization over all parameters being fitted using the TRR method, which is a computationally inexpensive optimization algorithm. Intelligent starting values greatly increase the odds of TRR finding the true global minimum, though this is not always a guaranteed outcome. In order to obtain error estimates of fitted parameters, the program in the second procedure uses a brute force approach to fit each parameter systematically. Specifically, the program steps through a grid of one parameter while optimizing the others by TRR to find the minimized χ^2 value for each step. Then the program calculates the normalized likelihood values over the grid. Under most circumstances, a plot of the likelihoods over the grid produces a bell curve that is easily fit to a Gaussian function to yield the mean and estimated standard deviation of the fitted parameter. This second procedure is repeated for every parameter. Assuming all the likelihoods behave in this Gaussian fashion, one standard deviation of a parameter would represent a 0.6826^n error window, where n is the number of parameters being fitted. Therefore, standard deviations would need to be adjusted to reflect a true 0.6826 error window. Aside from the variance of a single parameter, we might be interested in looking at the correlation of two parameters in order to identify highly correlated scenarios. In the third procedure, the program steps through a grid of each pair of two

parameters and optimizes χ^2 via TRR, calculates the joint likelihoods over the grid, and enables the user to visualize the χ^2 or likelihood distribution of each pair.

In a typical fitting process, the user first builds up the layered system with the GUI and enters the starting values for the parameters while visualizing the calculated curve with experimental data from a system of interest. The user then tries to pick a number of parameters for *XeRay* to fit while holding the other parameters constant, plots the likelihood curve, and refines the fitting parameters and ranges for further rounds of fitting.

The *XeRay* package is published as a public repository on www.github.com. Users can obtain the most up-to-date package at <https://github.com/ZhiliangGong/xeray> and add the package (including all the subfolders) to the MATLAB search path to enable it. Note that at the time of writing, the software runs on MATLAB 2015a or later versions. There are two versions of the software, both contained in the package. The first version is launched with the command “XeRayGUI” and analyzes datasets with spectra, giving the user the ability to visualize, compare, and integrate peaks within the software. The second version is launched with the command “XeRayGUI(2)” and is for datasets with integrated intensity.

Section 5.5: Case study 1: using XeRay to determine Ca²⁺ accumulation underneath an SOPA monolayer

Enter “XeRayGUI” at the MATLAB command line to launch the version of *XeRay* for a dataset with spectra and resize the GUI for proper display. The GUI contains three panels: the left for listing datasets, the middle with two plot regions, and the right with inputs, outputs, and other

manipulation tools. This version of the software takes in spectral data files of a standardized text format with extension “.xfluo” which specifies the incident angle range, energy in keV, and x-ray fluorescence intensity and error for each corresponding angle. Two examples of “.xfluo” files can be found in the “example” folder. If manually formatting data files becomes too tedious, the user might consider writing a script to automate the formatting process, as was proven necessary for users at the ChemMatCARS facility at Argonne National Labs.

As a demo, we will utilize TXRF data collected from two CaCl_2 systems. The first dataset, “bulk.xfluo,” is from an aqueous solution of 50 mM CaCl_2 with 10 mM 4-(2-hydroxyethyl)-1-piperazineethanesulfonic acid (HEPES), pH 7.5; the second dataset, “surf.xfluo,” is from an aqueous solution of 1 mM CaCl_2 with 10 mM HEPES, pH 7.5 with an SOPA monolayer compressed to 30 mN/m at the air/buffer interface. Click “load” to load both data files from the “example” folder. After loading, the first spectrum from the “bulk” dataset appears. The program might take a significantly longer time to load for its first launch in a MATLAB environment. With data loaded, the user can now carry out some data visualization manipulations, such as comparing the spectra of multiple scans at multiple angles, looking for a specific element by selecting one from the available drop-down menu, fitting the peak of that element with Gaussian or Lorentzian lineshapes, and subtracting a linear background from the fitted peaks. If the displayed energy range for an element needs to be changed, or an element of interest is not listed, it can be added by clicking the “Add or Modify” option in the element drop-down menu.

For this demo, choose Ca from the element drop-down list, check “Start Fitting,” and then select all of the listed angles. After fitting, the lower figure of the central panel shows the integrated

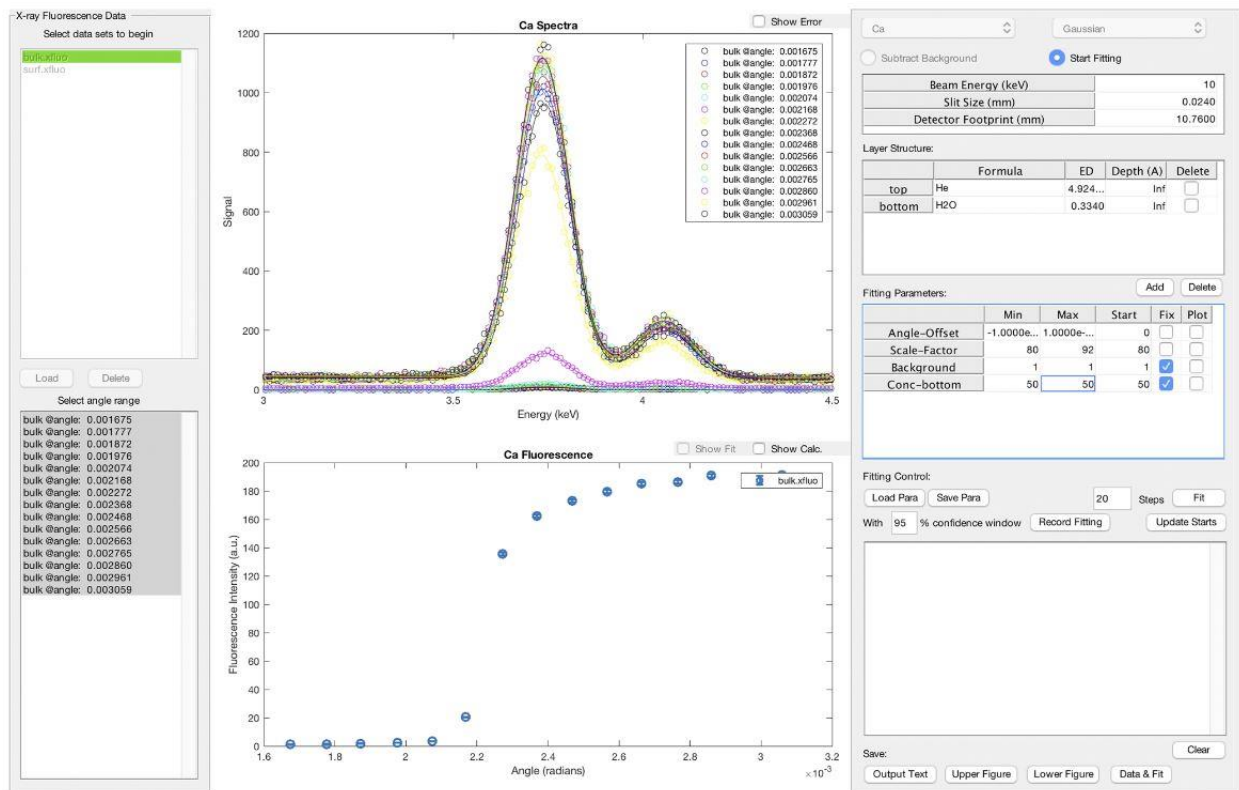


Figure 5.3: Fluorescence spectra and integrated signal from the bulk.xfluo data file. Scale the GUI window to show all graphical elements in the GUI properly. Input and check the following parameters: the beam energy (keV), the slit size of the incident beam (mm), and the detection length of the detector (mm). Build the layer structure with the use of the “Layer Structure” table, in which a chemical formula describes both the overall composition and electron density of a layer as calculated by the user or obtained otherwise. Note that the chemical formula should only contain element abbreviations and stoichiometry numbers, where the first letter of an element abbreviation is capitalized and the following letter, if applicable, is lowercase. Any element without an associated stoichiometry number is implied to be one. No spaces or other special symbols are allowed in the formula. Only the relative ratio of the atoms matter, so CH₂ is equivalent to C₂H₄. For example, a solution of 1M CaCl₂ can be represented as H₂O Ca0.018 Cl0.036. Also note that the bulk concentration is fixed at 50 mM, the surface concentration at 0 nm⁻², and the background at 0 a.u. for this “bulk” data set. The two varying parameters are angle offset and scale factor.

fluorescence intensities and the fits for all angles; the fits can look slightly different depending on the selected Gaussian or Lorentzian lineshape. At this point, the GUI should look like figure 5.3. Since there are two Gaussian peaks, each with a different energy and thus a different penetration depth in solution, the program chooses the peak with the higher intensity for subsequent data fitting.

A few fields describing the experimental system need to be filled in, as outlined in the caption for figure 5.3. The electron density of each layer can be obtained either by calculation given the composition and density of the layer or by other means, such as x-ray reflectivity studies. Below the parameter inputs is a table containing the fit parameters. The angle offset parameter accounts for small instrumental misalignment inherent to most instruments. As previously mentioned, the concentration in the top layer for an element of interest should be 0. Here the user can specify the lower bound, upper bound, and starting value for each parameter that the program fits. The “Min” and “Max” columns correspond to the lower and upper bounds, respectively. A parameter can be held constant throughout the fitting by checking “Fix.”

The user can click “Load Para” to load “bulk.xfluopara” to first analyze the bulk fluorescence signal. Inputs and data in the table can be manually edited or can be loaded by clicking the “Load Para” button, which loads a specifically formatted text file with extension “.xfluopara.” The user can click “Save Para” to save the current inputs and table data in this format or to manually create “.xfluopara” files based on the existing format. The purpose here is to fit the scale factor C_0 .

After loading the parameters, the user can check the “ShowCalc” box above the lower middle figure to show the calculated intensity for the given parameters and can perform a fitting procedure by clicking “Fit.” If a parallel pool is set up in MATLAB, an indicator should light up and the fitting would proceed in a parallelized fashion.

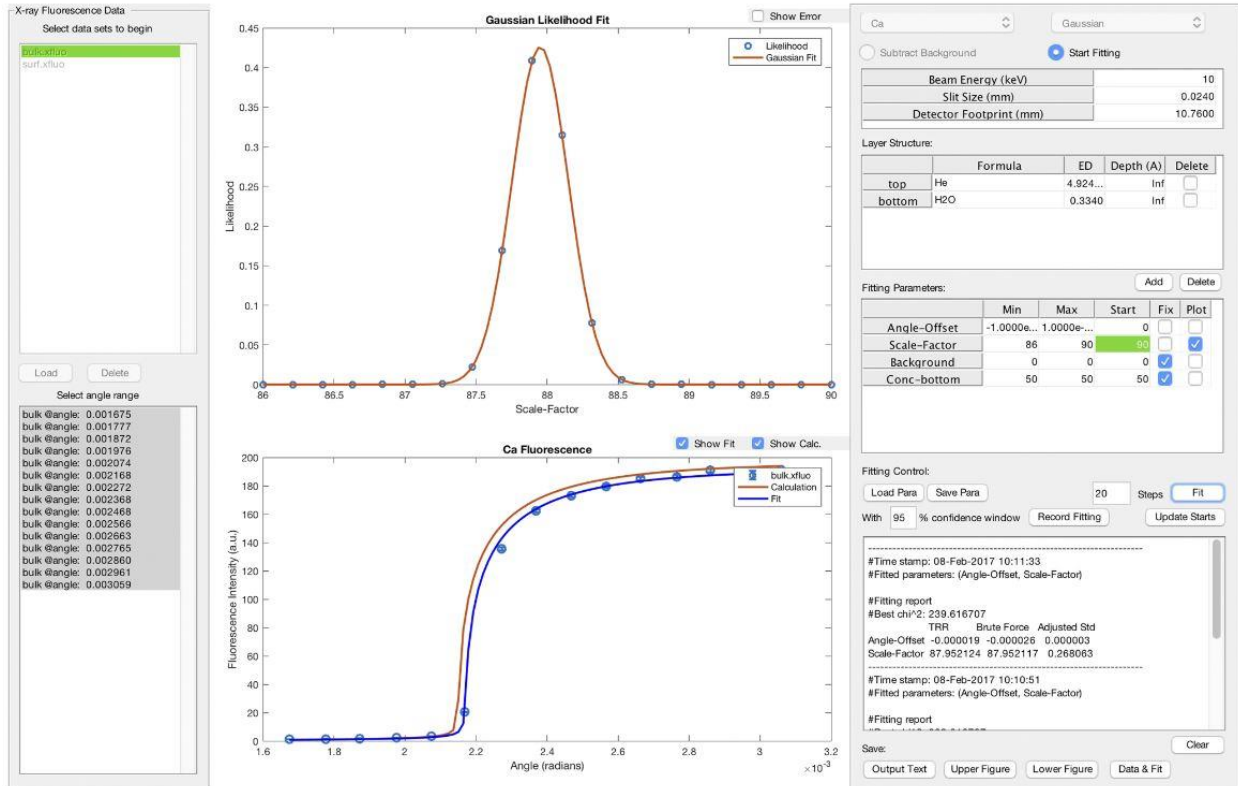


Figure 5.4: Fitted bulk.xfluo data set and visualization of the likelihood distribution of the angle offset. Fitting results are logged in the output box in the lower-right corner. Note that TRR in the output box means fitting is performed using the trust region reflective method, and “Adjusted Std” would represent a real 0.6826 error window for each parameter based on a brute force search. The purpose of fitting the “bulk” data is to obtain a scale factor, C_0 , which is found to be 88.0 ± 0.27 , a very tight error window. The upper plot shows the likelihood distribution of the scale factor and its Gaussian fit.

After the fitting procedure is completed, the fit is plotted on top of the data in the lower figure, and the fitting results are logged in the output box with a timestamp. At this point the user can choose to visualize the fitting quality based on likelihood, χ^2 , and their joint distributions between two parameters. To do so, one simply checks the “Plot” option in the table for the fitted parameters. The user can also change the reported confidence window, save the text from the output window, save the lower and upper middle figures, save the data the GUI is using, or save the data and fit together as a text file. The user can try checking “Plot” for angle offset, and the GUI should look something like figure 5.4.

The user should carefully inspect the likelihood and χ^2 distributions of the fitting parameters to ensure that all of them are nicely centered Gaussian or Gaussian-like distributions. Figure 5.5 shows an improper range for the scale factor. A typical fitting process would require multiple trials to iteratively refine the errors to a tight range for each fitting parameter.

After fitting the example data of the 50 mM CaCl_2 bulk signal, the user obtains a scale factor of 88.0 ± 0.27 and can now proceed to fit the surface data. At this point, the user can uncheck “Start Fitting,” select “surf.xfluo” in the file panel, select the whole angle range, check “Start Fitting,” load the “surf.xfluopara” parameter file for the surface data, and click “Fit.” Refer to figure 5.6 for the fitting parameters used. Fitting this dataset would give a surface Ca^{2+}

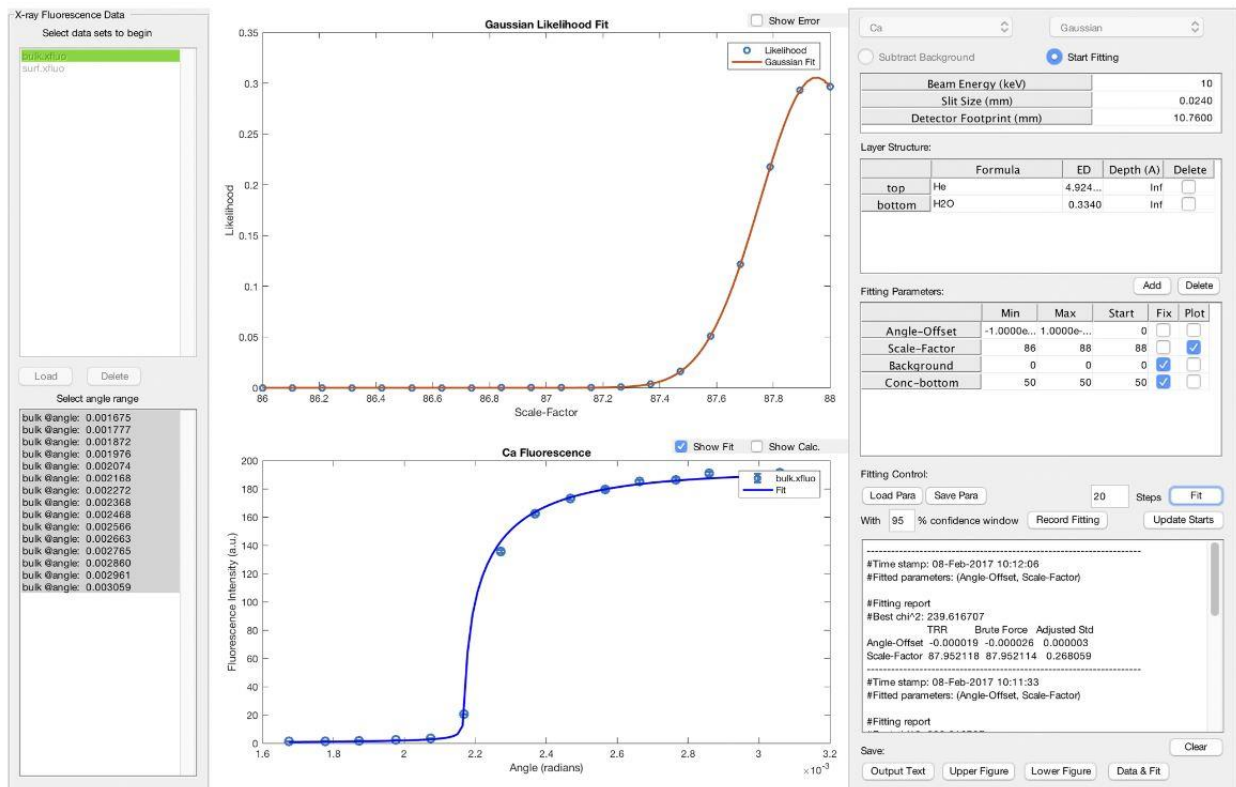


Figure 5.5: Example of an improperly set fitting range. A proper likelihood of the displayed parameter should be fit to a Gaussian or Gaussian-like distribution; in this example the upper bound of the scale factor is too small and needs to be increased.

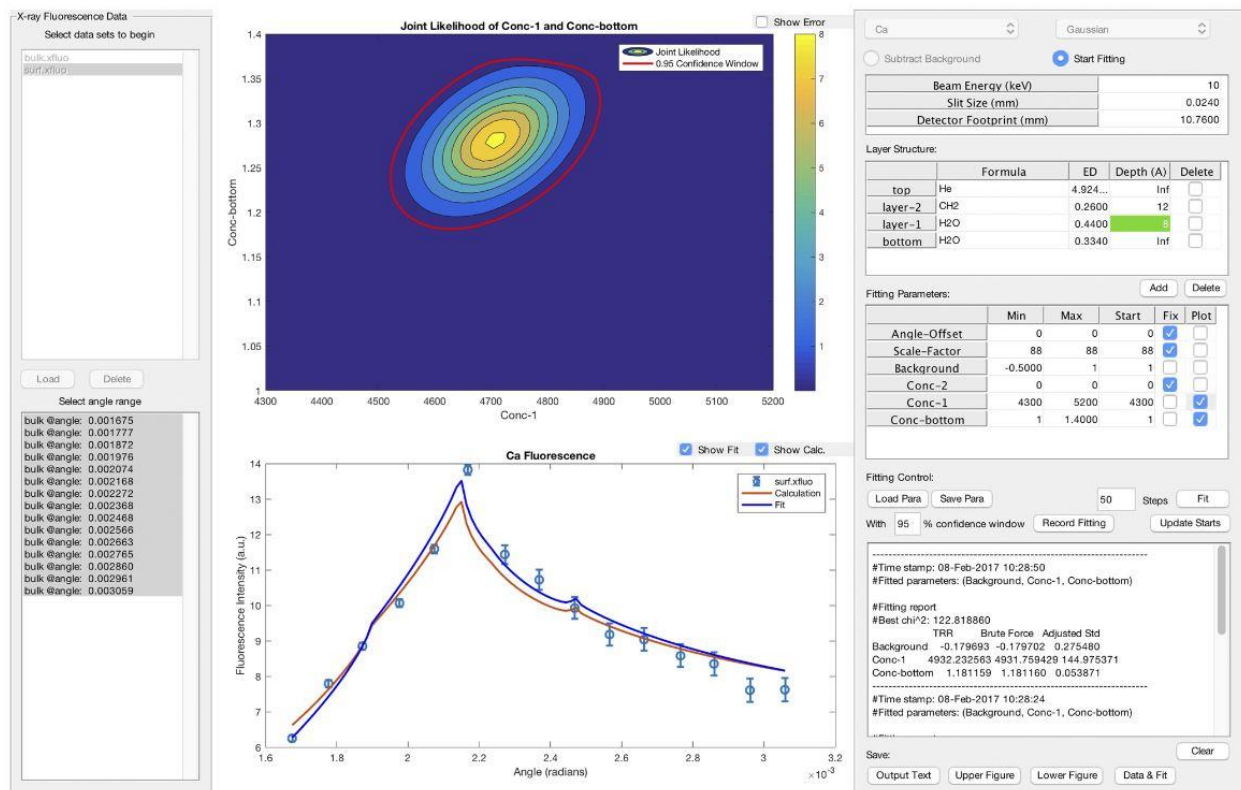


Figure 5.6: Fitting results for 1 mM CaCl₂ with an SOPA film. Proper fitting results yield a CaCl₂ concentration of 4.93 ± 0.14 M, corresponding to a surface concentration of 2.38 ± 0.06 ions/nm². The fitted results indicate a 1:1 stoichiometry between SOPA headgroups and Ca²⁺ ions. Note changes in the “Fix” column of the table, where the scale factor is now fixed to be 88. Here a constant negative background needs to be added to the signal from the insoluble Langmuir monolayer system, likely because the sensitivity of the instrument and our assumption of a perfectly coherent incident beam leads to an overestimation of the signal.

concentration of $4.93 \text{ M} \pm 0.14 \text{ M}$, which for the layer thickness of 8 nm (as measured from x-ray reflectivity) corresponds to 2.38 ± 0.06 ions/nm². The surface concentration of SOPA is 2.45 ± 0.03 molecules/nm², according to the surface pressure vs. area isotherm of SOPA at the experimental temperature of 23°C on a buffer with 10 mM HEPES and 1 mM Ca²⁺, pH 7.5. Therefore, the stoichiometry between SOPA headgroups and Ca²⁺ at the surface is close to 1:1. In fact, two earlier studies also revealed a 1:1 stoichiometry between Ca²⁺ and 1,2-dimyristoyl-*sn*-glycero-3-phosphate (DMPA) [31], we well as with 1,2-dioleoyl-*sn*-glycero-3-phosphate (DOPA)

[32]. It is worth noting that metal ions heavier than calcium generally have much higher excitation efficiency and thus produce much more accurate measurements.

Section 5.6: Case study 2: using *XeRay* to analyze fluorescence data obtained from a dodecane/surfactant/water interface

In addition to testing *XeRay* with an air/fluid interface dataset, we further confirmed the capability of the program to analyze total reflection fluorescence from a liquid/liquid interface. Here we used an x-ray fluorescence dataset on Sr^{2+} , a model heavy metal ion, from a dodecane/surfactant/water system as originally reported by Bu *et al.* [33]. Here the top liquid phase is the organic solvent dodecane, and the bottom liquid phase is an aqueous solution of Sr^{2+} at pH 5.7. The calibration data are collected from a dodecane/aqueous solution sample with 50 mM Sr^{2+} in the aqueous phase and no surfactants, and thus no interfacial enrichment of Sr^{2+} . The interface sample data of interest are collected from a dodecane/surfactant/water system, where the surfactant is di-hexadecyl phosphate (DHP) and the aqueous solution contains 0.01 mM Sr^{2+} . The “examples” folder contains the two datafiles as “sr-calibration” and “re-interface,” respectively. It is worth noting that in liquid/liquid interface studies, x-rays are incident on the sample from the *side* of the top phase as opposed to the *top* so as to incur minimal scattering upon entering the system. As a result, it is proper to assume the top organic phase to be infinite in thickness.

Here the fluorescence spectra are already integrated to give the total fluorescence signal, in which case we launch *XeRay* by typing “XeRayGUI(2)” in the MATLAB console. Besides the fact that there are no spectra visualization components in this new user interface (see, for example, figures 5.7 and 5.8), the analysis procedure closely resembles that of the air/fluid case.

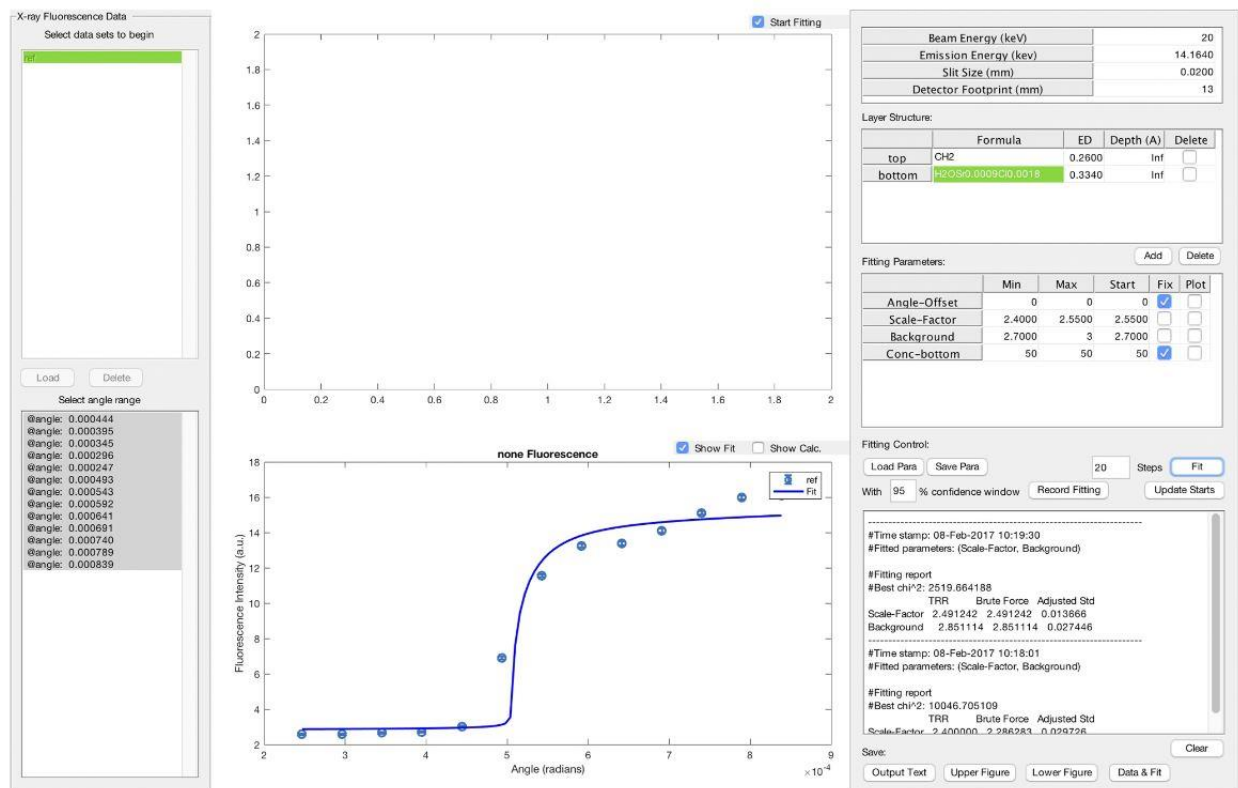


Figure 5.7: Fitting results for the dodecane/water calibration sample. Proper fitting yields a scale factor of 2.49 ± 0.01 . In this example, the thickness of dodecane is about 1.1 mm. Since the incident wave enters the dodecane phase from the side, scattering will be minimized when entering the system. The top phase is assumed to be infinite in thickness due to the significant distance the beam will have traveled by the time it reaches the interface. Note that “CH₂” was used to represent the chemical formula of dodecane, which suggests that slight deviations of the stoichiometry ratios in a chemical formula are not critical.

A scale factor of 2.49 ± 0.01 is first obtained from analyzing the calibration sample, which is then applied to fitting the surface enrichment of Sr²⁺ at the headgroup layer of the sample of interest. The layer structure of the sample of interest is built according to the result of fitting x-ray reflectivity data [33]. Specifically, there are five layers in total: the top infinite layer of dodecane, a small disordered layer attributed to the end methyl group of the surfactant, the hydrophobic tailgroup layer of the surfactant, the hydrophilic headgroup layer of the surfactant, and the bottom infinite layer of water. Sr²⁺ ions would predominantly accumulate at the headgroup layer and the fitting results indicate that as much as $5.3 \text{ M} \pm 0.2 \text{ M}$ Sr²⁺ is present in the headgroup layer, more

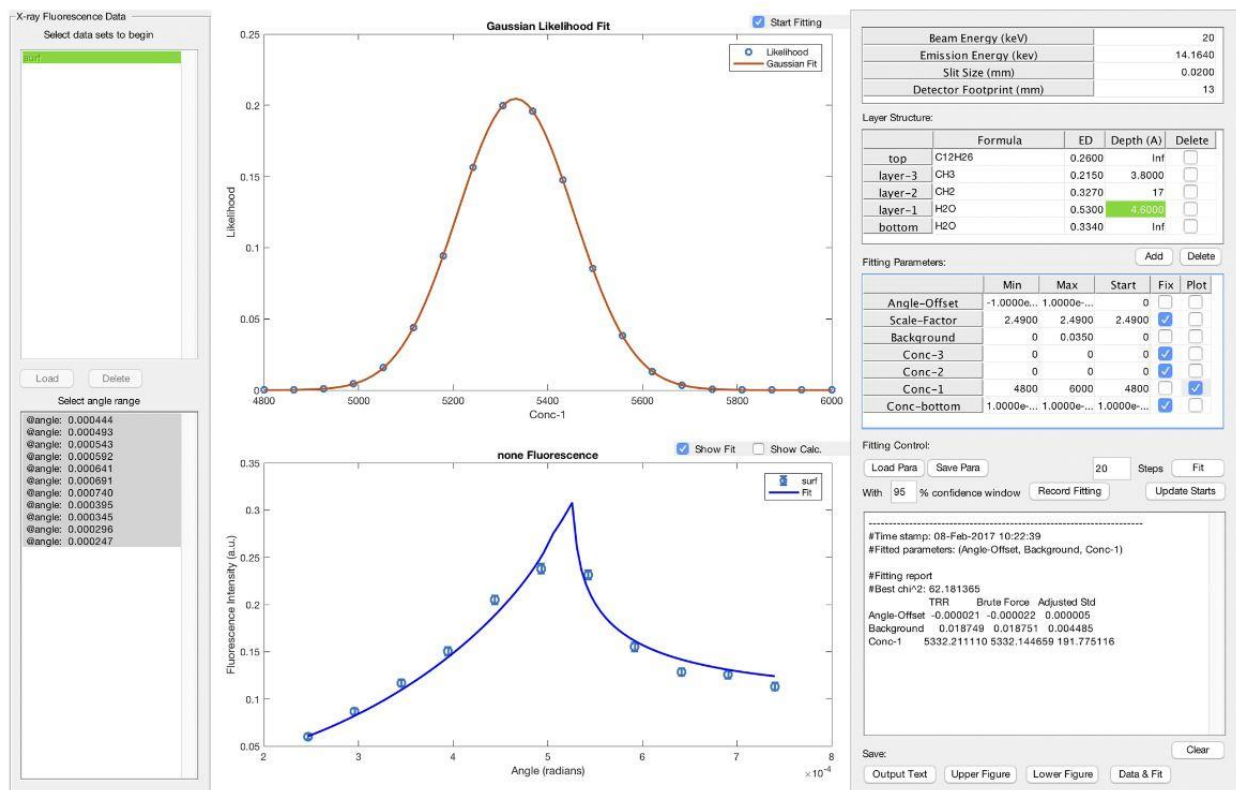


Figure 5.8: Fitting results for Sr^{2+} fluorescence from a dodecane/surfactant/water interface. With only 0.01 mM Sr^{2+} in the bulk of the aqueous phase, the signal emanating from the aqueous phase is small compared to that of the interface. The fitted surface concentration of 5.3 ± 0.2 M Sr^{2+} represents more than 5 orders of magnitude enrichment of the ion at the interface in the presence of the surfactant.

than 5 orders of magnitude more than the bulk concentration. This layer concentration translates to an area of $68_{-5}^{+6} \text{ \AA}^2$ (95% confidence) per Sr^{2+} ion, overlapping with the result from the previously reported range of $86_{-15}^{+20} \text{ \AA}^2$ (95% confidence). One possible contribution to the discrepancy between the mean values of the two results is the possible curvature of the liquid/liquid interface accounted for by the earlier report [33], but not considered in *XeRay*.

Section 5.7: Conclusions

Using *XeRay* we have been able to accurately analyze TXRF data from two distinct model systems, i.e., Ca^{2+} accumulation at the air/liquid interface and Sr^{2+} extraction at the liquid/liquid

interface. With the air/liquid dataset, we established a 1:1 stoichiometry between SOPA headgroups and Ca^{2+} ions at the air/water interface. In the liquid/liquid dataset, we have been able to reproduce the fitting results of Sr^{2+} enrichment at the dodecane/surfactant/water interface from a published report. We reasonably believe that *XeRay* could be readily used in studies involving solids or any other phases. We encourage potential users to try out the software package and contact the authors, beamline scientists at ChemMatCARS, or other liquid surface x-ray scattering facilities to discuss the potential for running similar experiments.

Section 5.8: Notes

Author contributions: Z.G., D.K. designed research; Z.G., D.K., H.L.H., J.M.H., T.S., **B.R.S.**, K.D.C. performed research; **B.R.S.** trained T.S. on the Langmuir trough; Z.G., D.K. produced the *XeRay* tool; Z.G., D.K., H.L.H., J.M.H., T.S., **B.R.S.** analyzed data; and Z.G., D.K. wrote the paper; Z.G., D.K., H.L.H., T.S., **B.R.S.** edited the paper.

Section 5.9: References

- [1] Lemmon, M. A. *Nature Reviews Molecular Cell Biology* **9**, 99–111 (2008).
- [2] Clapham, D. E. *Cell* **131**, 1047–1058 (2007).
- [3] Decher, G. & Schlenoff, J. B. *Multilayer thin films: sequential assembly of nanocomposite materials*. (John Wiley & Sons, 2006).
- [4] Kato, T. *Advanced Materials* **12**, 1543–1546 (2000).
- [5] Beckhoff, B. *et al. Anal. Chem.* **79**, 7873–7882 (2007).
- [6] Moyer, B. A. *Ion Exchange and Solvent Extraction: A Series of Advances, Volume 19*. (CRC Press, 2009).
- [7] Somorjai, G. A. & Li, Y. *Introduction to surface chemistry and catalysis*. (John Wiley & Sons, 2010).
- [8] Wobrauschek, P. *X-Ray Spectrometry* **36**, 289–300 (2007).
- [9] Bohlen, A. & Klockenkämper, R. Total-reflection X-ray fluorescence analysis and related methods. (2015).
- [10] Yoneda, Y. & Horiuchi, T. *Review of Scientific Instruments* **42**, 1069–1070 (1971).
- [11] Bu, W., Flores, K., Pleasants, J. & Vaknin, D. *Langmuir* **25**, 1068–1073 (2009).
- [12] Novikova, N. N. *et al. Journal of Applied Crystallography* **36**, 727–731 (2003).
- [13] Graber, Z. T. *et al. RSC Adv.* **5**, 106536–106542 (2015).
- [14] Szoboszlai, N., Polgári, Z., Mihucz, V. G. & Zárny, G. *Analytica Chimica Acta* **633**, 1–18 (2009).
- [15] Wang, W., Kuzmenko, I. & Vaknin, D. *Phys. Chem. Chem. Phys.* **16**, 13517–13522 (2014).
- [16] Körner, A. *et al. J. Phys. Chem. B* **117**, 5002–5008 (2013).
- [17] Bu, W. *et al. J. Phys. Chem. B* **118**, 12486–12500 (2014).
- [18] Geraki, K., Farquharson, M. & Bradley, D. *Physics in Medicine & Biology* **49**, 99 (2003).
- [19] Marguí, E., Queralt, I. & Hidalgo, M. *TrAC Trends in Analytical Chemistry* **28**, 362–372 (2009).

- [20] Borgese, L. *et al. Measurement Science and Technology* **20**, 084027 (2009).
- [21] Mantler, M. & Schreiner, M. *X-Ray Spectrometry* **29**, 3–17 (2000).
- [22] Lin, B. *et al. Physica B: Condensed Matter* **336**, 75–80 (2003).
- [23] von Bohlen, A. *Spectrochimica Acta Part B: Atomic Spectroscopy* **64**, 821–832 (2009).
- [24] Pianetta, P. *et al. Review of Scientific Instruments* **66**, 1293–1297 (1995).
- [25] Rehr, J. J. & Ankudinov, A. L. *Coordination Chemistry Reviews* **249**, 131–140 (2005).
- [26] Wang, W. *et al. Langmuir* **28**, 4274–4282 (2012).
- [27] The Atomic Scattering Factor Files. http://henke.lbl.gov/optical_constants/asf.html (Accessed 2/4/2022).
- [28] Vidal, B. & Vincent, P. *Appl. Opt.* **23**, 1794–1801 (1984).
- [29] Weisbrod, U., Gutschke, R., Knoth, J. & Schwenke, H. *Applied Physics A* **53**, 449–456 (1991).
- [30] Andrae, R. *arXiv preprint arXiv:1009.2755* (2010).
- [31] Garidel, P. & Blume, A. *Langmuir* **16**, 1662–1667 (2000).
- [32] Takahashi, H., Yasue, T., Ohki, K. & Hatta, I. *Biophysical journal* **69**, 1464–1472 (1995).
- [33] Bu, W. *et al. Journal of Applied Physics* **110**, 102214 (2011).

CHAPTER 6.

**LESSONS LEARNED FROM THE CREATION AND DEVELOPMENT OF A
RESEARCHER-LED SAFETY ORGANIZATION AT THE UNIVERSITY OF
CHICAGO**

Section 6.1: Overview

Safety standards and practices within academia have fallen well below those of their industrial and governmental counterparts due, in large part, to a relative absence of the financial and public pressures that become driving forces for such standards within government and industry [1]. However, it has been shown that a strong safety-centric culture has a significant statistical correlation with a low occurrence of high-risk behaviors, low accident rates, high productivity, low absenteeism, and long-term institutional success [2-6]. Considering these correlations and the numerous devastating accidents within academia [7], vigorous discussions about how to build and maintain academic safety cultures have been spreading across the United States. Numerous connections between strong, coherent, safety-minded leadership and the institution's safety culture have been made [7-12], yet the unique and sometimes nebulous leadership structures within academia often complicate and fragment these efforts, leading to diffuse, sometimes conflicting, leadership and a primary emphasis on regulation compliance over collaborative, proactive engagement. In an effort to address these issues, here I describe a case study of the implementation of a researcher-led safety team working to bridge the gap between safety administration, departmental administration, and researchers at The University of Chicago: The Joint Research Safety Initiative (JRSI). In this chapter, I will provide a framework for understanding safety culture in academia, some context for the recent advances of safety teams as a mechanism to improve

safety culture, and some of the programs implemented by the JRSI in its first few years of existence.

Section 6.2: Background

Chemistry has exposed researchers to life-threatening accidents and safety concerns for as long as the discipline has formally existed, so much so that for several centuries sacrificing one's life or limbs was viewed as a necessary part of being a successful chemist. The earliest recorded lab accident which was documented as such occurred in 1767, when Johann Gottlob Lehmann, a German geologist, died from inhaling toxic fumes after a crucible containing arsenic compounds exploded during heating [13]; a curious reader would struggle to find this information as it is often overlooked or not mentioned in the historical record [14]. Sadly, this phenomenon where chemist's accomplishments are lauded while details of their laboratory mishaps are overlooked appears to become a trend over the subsequent centuries: Joseph-Louis Gay-Lussac, most famously known for his work on ideal gases, suffered temporary blindness and long-term eyesight problems as a result of a potassium explosion that occurred when he was not wearing any protective eyewear [15, 16]; Robert Bunsen, namesake of the Bunsen burner popularized for flame tests, permanently lost the use of one of his eyes after a cacodyl chloride explosion in his lab [15, 17]; and Humphry Davy, whose work with electrolysis helped to isolate elemental potassium and sodium, suffered injuries from a nitrogen trichloride explosion [18, 19], to name a few. More startlingly, historical records indicate that major lab accidents resulting in injury or loss of life have occurred every few years since the beginning of the 20th century, and continue to happen even in modern times.

Although health hazards and accidents have long been intertwined with the pursuit of chemistry, interest in safety in the United States really only took off with the rise of industrialization in the early 1900's [20]. With the advent of new production technologies and the creation of large-scale manufacturing came a slew of new workplace hazards that threatened the life and wellbeing of the workforce; only through investigative journalism (at the time deemed "muckraking") and increasing public outcry did the local and national governments begin to pay attention to the appalling conditions workers experienced. As more and more workplace hazards were brought to the public attention, safety issues began to be addressed through government legislation and workplace best-practices.

Despite the widespread public interest in making workplaces more safe, it was not until 1970 with the signing of the Occupational Safety and Health Act that a formal government organization was founded to set and enforce formal safety standards [21]. The Occupational Safety and Health Act created the Occupational Safety and Health Administration (OSHA), which has persisted to this day and continues to set federal safety standards to ensure safe and healthful working conditions. While OSHA has reported many successes from its formal legislation and enforcement strategies [22, 23], it tends to shy away from making statements or suggestions about safety culture because it has proven incredibly difficult to quantify and assess, despite it being widely regarded as important [24]. Overall, this focus on legislation and enforcement while ignoring culture and climate has produced the circumstances that most academic labs find themselves in today, where safety begins and ends at passing routine inspections.

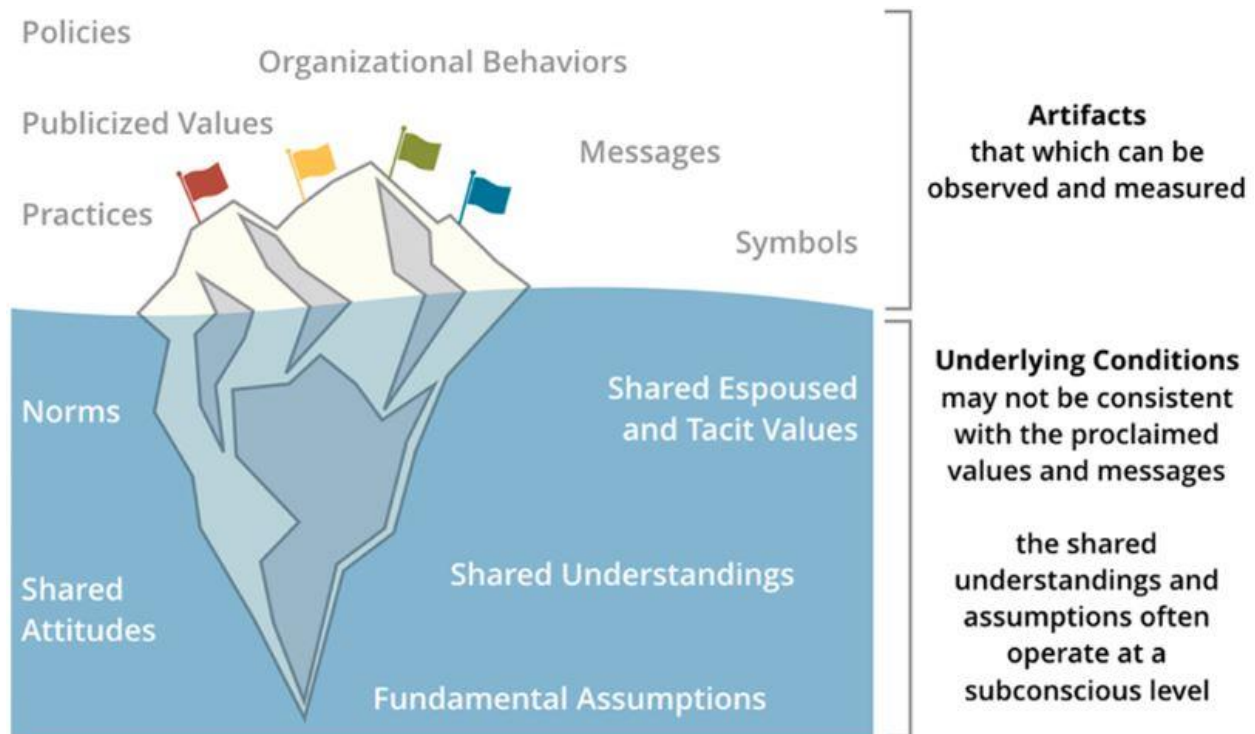


Figure 6.1: Schematic representation of organizational culture based on Edgar Schein’s levels of culture. While many of the short-term goals of the JRSI were established to address artifacts of the safety culture at The University of Chicago, improving the underlying conditions requires long-term engagement of active programming, researcher education, and organizational evaluation. Visual cartoon adapted from [26].

Section 6.3: The Advent and Expansion of Safety Teams in the United States

Safety culture is an exceptionally difficult thing to quantify and assess due to its inherent intangibility; the precise definition of an institution’s safety culture is ill-defined and varies greatly between fields [25]. Herein, I will use Edgar Shein’s model of organizational culture [26], where I will use the term “safety culture” to refer to an organization’s shared beliefs, values, and attitudes regarding safety (underlying conditions) as well as the organization’s observable safety-related behaviors, policies, publicized values, and front-facing messages (artifacts) as depicted in figure 6.1. With this definition in hand, how then can we inspire a change in safety culture?

To begin addressing the question of how to most efficiently and effectively motivate institutional cultural shifts within academia, two key starting points have been pursued: (1) emulating aspects of industrial and governmental efforts to maintain standards of safety, risk management, and standard operating procedure protocols, and (2) establishing researcher-led safety teams and initiatives to internally motivate and invigorate safety-minded improvements. A distinguishing force in this alignment of industrial and academic safety practices has been the Dow Lab Safety Academy (DLSA), a program built to highlight the integrated nature of safety and science at the industrial level, to “enhance the awareness of safe practices in academic research laboratories, and to promote a safety-first mindset in the future workforce of the chemical industry.” [27] In 2012, it was through a partnership with The Dow Chemical Company that researchers from The University of Minnesota’s Department of Chemical Engineering and

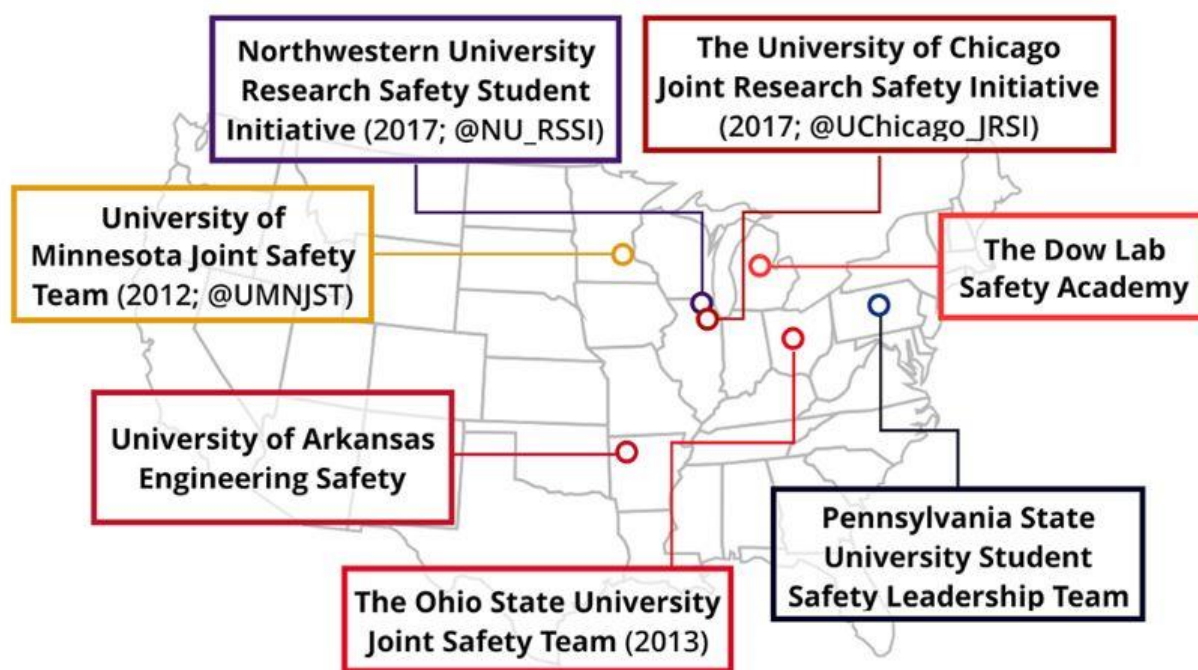


Figure 6.2: Student-led safety initiatives and teams in the U.S. that were established through partnership with The Dow Lab Safety Academy. The information in parentheses provides their year of establishment and Twitter handles, if available. This schematic is not inclusive of all current laboratory safety teams; for a comprehensive list, see [28].

Materials Science created the first researcher-led safety team, The University of Minnesota Joint Safety Team (UMN JST) [9], which would later serve as the inspirational catalyst for many of the other academic safety teams appearing throughout the United States.

In the past decade, there has been rapid growth in the number of researcher-led safety teams in the United States. Martin and coworkers provide an excellent account of the growth of these laboratory safety teams over the past decade [28]. In addition to the DLSA, workshops have been organized by the American Chemical Society (ACS) to give participants knowledge and resources to develop teams at their home institutions, as detailed by Miller and Tyler [29]. I direct interested readers to these reports for a comprehensive overview of the expansion of groups like the JRSI. For the scope of this work, figure 6.2 exhibits a select number of groups that have directly partnered with the DLSA. It is my hope that this case study can provide context, inspiration, and lessons learned for established teams, newly created teams, and future teams alike.

Section 6.4: Creation of the JRSI at The University of Chicago

With the support of safety administrators and with inspiration from the successes of the UMN JST, 10 representatives from The University of Chicago (eight researchers, one faculty member, and one divisional lab safety specialist) attended the DLSA in the Fall of 2017 to learn how to model their safety practices after industrial standards and how to form their own safety team [30]. The creation of the JRSI at The University of Chicago was catalyzed in large part by this fruitful excursion full of collaborative discussions and brainstorming sessions with Dow representatives, UMN JST members, and University of Chicago safety administrators. But in order to understand the formation of the JRSI, it is first necessary to understand the context and history

of safety administration at The University of Chicago. Prior to 2009, The University of Chicago's safety administration consisted of the traditional Environmental Health and Safety (EH&S) department which was broadly responsible for the health, safety, and environmental compliance of the local educational and research communities. However, in 2009, Malcom Casadaban, a University of Chicago Associate Professor, died after being exposed to *Yersinia pestis* and contracting the plague; a mere two years later, a university researcher was hospitalized for surgery and antibiotic treatment after being exposed to *Bacillus cereus*. It was in response to these startling exposures that The University of Chicago restructured its traditional safety department by creating the Office of Research Safety (ORS) which reported directly to the Vice President of Research and National Laboratories and took on the responsibility of assessing research risk, providing new training, and conducting regular inspections. This newly created ORS took an active role in supporting researchers and sought to empower researchers in strengthening safety culture by implementing a variety of programs, including creating an online anonymous incident reporting tool and publishing a publicly available lessons learned repository.

In alignment with the key principles of safety teams discussed in the literature [9,12,31], the JRSI does not assume the enforcement roles or hazard training responsibilities that EH&S and ORS assume. Instead, the JRSI works to facilitate dialogues between the various administrative, student, and researcher groups within the Pritzker School of Molecular Engineering (PME) and the Department of Chemistry, with the goal of working hand in hand with these various groups to make resources easier to access and to involve researchers more directly in conversations about safety. Figure 6.3 depicts the different ways in which the JRSI has collaborated closely with safety

administration at The University of Chicago by organizing various responsibilities and collaborations into a Venn diagram.

The JRSI serves and comprises researchers spanning two separate departments at The University of Chicago: the PME and the Department of Chemistry. The Department of Chemistry was one of the first departments established when The University of Chicago was founded in 1890. At the time of writing The Department of Chemistry consists of 20 research-conducting professors, 2 associate professors, 6 assistant professors (3 new hires since the JRSI's inception), 175-200 full time graduate student researchers, and approximately 60 postdoctoral researchers. The Department of Chemistry conducts research in the areas of inorganic, organic, and physical chemistry with



Figure 6.3: Responsibilities of and collaboration between EH&S, ORS, and the JRSI.

interdisciplinary work in the areas of biology, physics, and materials science. The Institute for Molecular Engineering (IME), later renamed the Pritzker School for Molecular Engineering (PME), is dedicated solely to applying molecular-level science to the design of advanced devices, processes, and technologies, and was founded in 2011 through partnership with Argonne National Laboratory before becoming a separate school at The University of Chicago in 2019. At the time of writing, the PME consists of 20 research-conducting professors (12 new hires), 100-150 full time graduate student researchers, and approximately 80 postdoctoral researchers. The interdisciplinary research themes of the PME include “Arts, Sciences and Technology,” “Immuno-engineering,” “Materials Systems of Sustainability and Health,” and “Quantum Engineering,” and it should be noted that the PME is the first school dedicated to molecular engineering in the United States. In both the Department of Chemistry and the PME, all laboratories are required to have at least one Lab Safety Contact (LSC), who traditionally has served as a point of contact for ORS and EH&S in safety-related matters. The LSC position can either be voluntary or it can be appointed by the Principle Investigator (PI), and it can be filled by a graduate student researcher, a postdoctoral research associate, a research staff member, or the PI themselves. There is no limit to the length of time that an LSC can serve in the position, and there are no year-related restrictions on who can serve as an LSC for graduate students.

Section 6.5: Description and analysis of implemented programs and events

Section 6.5.1: Development of the JRSI’s organizational structure

Upon returning to The University of Chicago from the excursion to the DLSA, a subset of attendees interested in the practical development of a safety team began meeting monthly with

administrators from EH&S and ORS. At these meetings, the JRSI's initial members worked with safety administration to form a more holistic picture of safety and research at The University of Chicago and to outline both short-and long-term goals. We worked with departmental administration to coordinate a meeting with faculty members where we could introduce our mission with the support of department heads. After explaining our purpose and niche, we spent the next two years developing programs and creating and organized repository of documents and advertising materials. During this time, the JRSI continued to operate under a mostly informal structure where JRSI members took on various roles as needed, with the exception of more formalized executive positions (President and Vice President). The President's and Vice President's responsibilities included meeting with departmental heads, coordinating regularly scheduled meetings, speaking with outside safety teams, and promoting the visibility of programs and activities. While we did not officially solicit new members during our first few years, we did welcome those who showed interest in participation and developing the organization. The number of board members fluctuated during this time, but after approximately one year board composition stabilized to 5 members. As we began implementing programming and started having member turnover, we initiated conversations with departmental heads about providing a small quarterly supplemental stipend for members of the JRSI. This stipend is meant to ensure the JRSI's continuation through supporting the work that JRSI members do on top of their already heavy research load and through encouraging new members to participate.

In the summer of 2019, we began our first round of active recruitment by sending an application to apply for board membership via email; in this solicitation, we detailed the potential benefits of participating in our organization, including distinguishing one's CV with professional

service, obtaining low-stakes experience in a safety career path, working toward the development of one's department, and the aforementioned supplemental stipend. During this first application round, we received 14 applications – 8 from the PME and 6 from the Department of Chemistry – with 50% of applicants being participants in our first Peer Lab Walkthrough event and 43% of applications currently or previously serving as LSCs (21% of applicants were both participants in the Peer Lab Walkthrough and LSCs). During this application cycle, we brought on 7 new members for a new total of 10 board members. It was at this point that the JRSI's organizational structure became more formalized, consisting of an Executive Committee comprised of two Co-Presidents and a Treasurer, and four different subcommittees each chaired by a member of the Executive Committee. The four subcommittees were organized around the four key areas of the JRSI's work (Publicity, Surveying, Education, and Finance) and have allowed us to function more efficiently through the compartmentalization of responsibilities while keeping avenues of communication between committees clear and well-defined.

Section 6.5.2: Evaluating Safety Culture and Organizational Effectiveness

The major and subsisting effects of our implemented programs will likely not be seen during the tenure of the original JRSI team. Further, in order to appropriately gauge the effectiveness of the JRSI and its programs on positively impacting safety culture, it is imperative to utilize appropriate and robust methods to probe not only the artifacts of a university's safety culture but the underlying conditions as well. While there are numerous reports on evaluating *safety culture* (as defined above and illustrated in figure 6.1) and *safety climate* (i.e., the perception of valuing safety in an organization at specific points in time) at universities [7,9,11,12,25,32], to the extent of my knowledge very few long-term studies have been conducted.

When the JRSI was first forming, we endeavored to conduct surveys to be able to make conclusions on the state of The University of Chicago's safety culture and to identify specific areas that could be targeted for improvement. To this end, we developed a short initial survey that was sent to all of the LSCs within the PME and the Department of Chemistry, for which we offered no incentive to respond. Though we were able to glean a fair bit of information from this initial survey and used it to internally motivate programming, the biased nature of our chosen sampling precludes us from making a true assessment of the nature of The University's safety culture, and our failure to obtain formal Institutional Review Board (IRB) exemption or approval prior to surveying precludes us from sharing the survey results with external communities. The JRSI is currently working on the development of a robust, IRB-approved, department-wide survey for which we will offer entry into a raffle drawing for a financial prize as an incentive to participate.

Section 6.5.3: Educating Researchers, Teachers, and Safety Contacts

In an effort to make the most efficient impact on our University's safety culture, we identified and targeted two key demographics – LSCs and first-year graduate students – and developed interpersonal training programs and support systems for them. One of the first endeavors the JRSI undertook was to create an original program intended to develop safety-minded interpersonal training for these targeted key demographics. We strategized that incoming students can be strong drivers of cultural change in that they have not yet been exposed to the existing institutional safety culture; this, in combination with the fact that they still have many years of research ahead of them, may make matriculating graduate students an impactful demographic for working on long-term cultural change. With this in mind, we developed a training for first-year

students aimed at developing the soft skills required to communicate effectively and to contribute to a positive and supportive atmosphere around safety. It is our hope that, over time, these students will bring these skills into their research laboratories and set a new precedent for future generations of graduate students.

The first-year training we devised can be broken up into three sections: (1) a description of tools for positive, effective communication, (2) a demonstration of how these tools can be applied in relevant laboratory settings, and (3) an opportunity to practice using these tools in a low-stakes roleplay with peers. The main tool described in the presentation is an adaptation of a concept we originally encountered at the DLSA: we encourage all researchers to make S.P.A.C.E. for safety [27]. Using this tool, we hoped to empower researchers to Speak up about potential safety issues, Personalize conversations about safety, Ask open-ended questions, Create an atmosphere where questioning is encouraged, and Escalate an issue to an appropriate authority if needed. Following this introduction to S.P.A.C.E., students were given a handout with tips, tricks, and reminders for how to positively approach a confrontation about safety; this document is reproduced in appendix 6.1.

With S.P.A.C.E. and conflict resolution strategies in hand, JRSI presenters roleplayed demonstrations on applying these tools in a lab setting, including an example where a safety issue is easily identified and corrected (e.g., getting an undergraduate student to wear their goggles in a general chemistry lab), and an example where a peer is particularly stubborn about an unsafe practice (e.g., wearing gloves while using glove-free communal computers). Then, after discussing and demonstrating how new students might go about having these difficult conversations, we gave

them an opportunity to practice what they learned through additional roleplaying with their peers. Students were split into groups of four and given two scenarios to enact; each scenario was navigated by two students – one who made an egregious safety mistake, the other a peer who intervened – while the other two students observed the interaction and commented on the successes and shortcomings of each conversation. After the enactments, the room reconvened to discuss what did and did not work well in each of their situations; this public forum to discuss their experiences facilitated the reinforcement of good practices that were well received in the interactions and opened discussion about why some tactics did not work well. This training was made mandatory for all first-year students (approximately 40 people per department) during orientation through collaboration with departmental administration. We are currently working on developing programs through which we can check in with students who completed this training and through which we can follow their journey as they integrate into the existing safety culture within their research laboratories.

On a different note, when the JRSI began reaching out to LSCs to solicit input on new programs and areas of interest, we realized that many of our respondents viewed their jobs differently; some LSCs felt that they assumed total legal responsibility for the safety of their lab, whereas others viewed the position as a simple title that merely required their contact info to be posted around laboratory spaces. Additionally, there were some respondents who openly admitted that they did not have any idea what the role entailed. To tackle the wide breadth of misconceptions about the LSC role, we adopted a twofold approach wherein we (1) formalized and compiled a list of responsibilities, expectations, and a guidebook for anyone serving as an LSC (reproduced for the reader's reference in appendix 6.2), and (2) implemented an LSC training which detailed the

newly formalized list of responsibilities and presented a tutorial for how to interact with important safety resources on campus, including using the UCAIR system [33], maintaining laboratory placards and signage through our EH&S Assistant, and how to properly request hazardous waste pickup. In addition, during the training LSCs were given an abbreviated version of the aforementioned first-year training aimed at improving interpersonal communication skills; since the LSCs are expected to engage in potentially difficult conversations involving safety, we decided to equip them with the same strategies and tools to facilitate productive, non-confrontational conversations. After the training, LSCs were given the aforementioned compiled guidebook; since there is no set timeframe for LSC turnover at The University of Chicago, we strategized that this guidebook would serve as an introduction to the position for new LSCs until they had the opportunity to participate in the annual training.

Section 6.5.4: Facilitating open dialogues and collaborations

It is largely recognized that collaborative, inclusive interactions increase active participation and involvement within an organization. Furthermore, it has been concluded that insufficient collaboration, specifically between researchers and internal safety administration in academia, cultivates an overly top-down, largely compliance-based approach to safety [1]. Thus, from the beginning, a defining theme of our organization has been to facilitate dialogues both on the peer-to-peer level and on the administration-to-researcher level. In this section, I will elaborate on programs that were implemented to address these collaborative engagement goals, including examples of programs that were developed by the JRSI as well as programs modified from other existing safety teams.

When the JRSI was first getting established, it hosted a two day kickoff symposium and vendor fair to officially unveil the organization and to begin forging interpersonal connections between researchers, safety administrators, and departmental administrators. This novel symposium, hosted in Spring 2018, commenced with talks from the Deans of both the Physical Sciences Division (under which the Department of Chemistry falls) and the PME, as well as the Senior Associate Vice President for Strategic Initiatives at the Office of Research and National Laboratories. These talks were followed by invited experts in laboratory safety, hailing from academic institutions, national laboratories, and prominent industry partners. Guest speakers discussed their experiences in chemical health and safety, as well as their personal stories on both the importance of safety and their own efforts to build a more robust safety culture at their respective institutions or companies. Afterward, we organized a small reception and poster session to encourage further discussions among attendees. Roughly 65 students, postdocs, researchers, and faculty attended the talks and reception, accounting for around 20% of the personnel in Chemistry and the PME combined. Attendance at this event was encouraged by entering the names of those who both RSVP'd in advance and who signed in at the welcome table into a raffle for monetary and nonmonetary prizes (both provided by the JRSI and donated by industrial partners).

Two days after the invited speaker symposium, the JRSI organized a safety-centric vendor fair. In addition to their normal marketing, these vendors performed safety demonstrations and distributed safety-related promotional items such as glove samples and informational posters. In contrast to the symposium several days earlier, our goal for the vendor fair was to approach the discussion of safety from a more hands-on perspective; this was accomplished by encouraging conversations about and demonstrations on ways in which researchers could immediately enact

tangible changes to improve safety, such as adopting better PPE or new engineering controls for a procedure. Around 150 graduate researchers, postdoctoral researchers, undergraduates, faculty, and staff from the PME and the Department of Chemistry attended this event for which we received overall positive feedback, both from the vendors and the attendees.

Another creative and potentially high-impact approach to fostering positive safety culture is hosting a lab walkthrough event. Inspired by the successes of our sister organization, the UMN

A



B



Figure 6.4: Photographs from the Peer Lab Walkthrough event. (A): Graduate student volunteers participated in training on the scoring criteria. **(B):** The Huang Lab won the grand prize trophy for the demonstration of excellence in safety among peers.

JST, the JRSI introduced a pilot Peer Lab Walkthrough in early 2019. This event was a friendly competition in the Department of Chemistry and the PME which was intended to promote safety innovation, to elicit camaraderie, and to encourage open discussions between labs about best practices with regards to safety. The competition was a collaborative educational opportunity for research groups to share safety knowledge, creative solutions, and lessons learned without regulatory authority or the threat of punitive action. Events similar to a Peer Lab Walkthrough are beneficial to all members of the research community in that they permit the transfer of unique perspectives on protocols and effective risk management, which can be especially vital for new techniques or reactions [34]. Additionally, communication between laboratories can assist with formulating and transferring solutions to ubiquitous safety problems. LSCs and graduate student researchers from both units volunteered as judges (figure 6.4a) to assess a dozen voluntarily participating laboratories (6 laboratories or 26% of active research laboratories from the Department of Chemistry and 6 laboratories or 28% of active research laboratories from the PME at the time of the walkthrough, correcting for joint appointments). The JRSI, in partnership with ORS, established a detailed scoring rubric adapted from the one used by the UMN JST. The 2019 scoring rubric is included in appendix 6.3.

A month before the scheduled walkthroughs, the JRSI trained volunteers on how to score effectively and uniformly while putting an emphasis on collaboration and mutual brainstorming. A number of hazards and standard practices – such as eyewash maintenance, PPE usage, and waste storage – were considered and normalized for each lab’s specific hazard categories; scoring awarded innovative, proactive solutions to common problems and noted shortcomings that may lead to minor incidents and major accidents. After all laboratories were assessed and scores were

tallied, the JRSI hosted an awards ceremony and gave prizes to the highest-scoring laboratories (figure 6.4b). One of the unique challenges to conducting a single joint walkthrough event between a strongly established department and a brand new one was the consideration of how to distribute awards in a manner ensuring that each department had a fair chance of winning. Our solution to this problem was to award a single Grand Prize (up to \$500) for the highest scoring lab spanning both units, and two Runner-Up Prizes (up to \$250 each) for the highest-scoring lab in the non-winning unit and the runner-up lab in the winning unit. Monetary prizes were awarded in the form of a reimbursement for an event or items of the lab's choosing; in 2019, winners purchased lab-branded items, took a lab-outing to play whirlyball and to bowl, and had a cookout. Bonus honorable mentions were given to laboratories that had particularly innovative and creative solutions to common lab problems, such as using colored tape to designate chemically-contaminated bench space or using voice control to play music hands-free in the lab. Approximately 30-40 total attendees were present at the award ceremony, and anecdotal evidence from some participants indicated that the ceremony itself may have boosted participation in the Walkthrough event. The Peer Lab Walkthrough will be an annual event, which we hope will garner even more participants from the Department of Chemistry and PME in upcoming years.

Section 6.5.5: Defragmenting safety efforts and resources

A 2012 report by the Safety Culture Task Force of the ACS Committee on Chemical Safety identified several key barriers to achieving a strong safety culture, many of which involved fragmented infrastructure, support, resources, and educational materials [1]. The Task Force argued that this disjointed approach to safety leads to a significant lack of clarity and an overall dissolution of responsibility and motivation. The JRSI's response to this identified problem has

been a three-fold combination of newly implemented and modified programs; namely, we (1) developed a centralized JRSI website [33] where the disparate internal and external resources are compiled and presented clearly and concisely; (2) have acted as a conduit among university, departmental, and safety administrators and researchers to better coordinate safety efforts; and (3) created and maintained a compiled database of the aforementioned Safety Moments.

Central to a strong, vibrant safety culture is a coherent, accessible, and robust safety infrastructure, and thus, central to the JRSI is the elevation of this infrastructure. In the development of its website, the JRSI worked with safety administrators to identify and clarify the disparate but related safety resources, both internal and external to The University of Chicago, and coalesced them into a single accessible portal where all members of our constituency – researchers, undergraduates, teaching assistants, faculty, safety administrators, staff, and visitors – can navigate our broader, more complex infrastructure with ease. Aside from using our website to shed light on internal resources that are oftentimes unknown in the community, we also provide faster access to knowledge about emergency response procedures, have a compiled FAQ section, and maintain a Helpful Contacts section where we highlight helpful members of the community who were previously discovered via word of mouth. To date, the JRSI's website has served as a place for the advertisement and organization of collaborative engagement events like the Peer Lab Walkthrough, a place where researchers and staff can ask questions and request program development in an otherwise nebulous structure, and a place for outside communities to interface with the Initiative. I anticipate that many other academic institutions might struggle with coherency and approachability in their safety administration; in response to this common problem, the JRSI

has found that maintaining a sociable, cohesive, and open website is an effective means by which to begin bringing larger communities together.

Section 6.6: Conclusions

In the broadest sense, the focus of the JRSI is to build a strong, positive, and robust culture of safety at The University of Chicago by improving both the visible artifacts of culture along with their intangible underlying conditions, as outlined in our initial discussions of Shein's levels of culture in figure 6.1. The achievement of this endeavor unavoidably requires an extensive period of time as well as strong and carefully crafted metrics to gauge its progress. However, we believe that reporting on the initial lessons learned from the development and implementation of a researcher-led safety group at The University of Chicago, where we serve not only the well-established Department of Chemistry but also the comparatively new PME, can help researchers across the country more efficiently and effectively start their own teams in a variety of new conditions.

Although there has been clear institutional progress in academic laboratory safety, much work remains to be done. Safety culture is challenging to measure, but a key component of it is to build a foundation for researchers to engage in active conversations about safety. Too often, laboratory safety is viewed as a system based on compliance, rules, and regulations that are enforced with admonishment or punitive repercussions, when it should really be viewed through the lens of preventing harm to researchers, society, and the environment. New initiatives from ACS Chemical Health & Safety, such as Safety Highlights [35], Literature Highlights [36], and Community Highlights [37] are well poised to change this perception for all members of the

chemical health and safety community, especially for researchers in academia. Ultimately, we strive to create a culture where people are not following safe practices because they are *forced* to, but rather that they see it as an *imperative component* of conducting research – the first step of which, we believe, is to report on a new set of lessons learned from the development of a new paradigm of safety communication and researcher involvement.

Section 6.7: References

- [1] *Creating Safety Cultures in Academic Institutions: A Report of the Safety Culture Task Force of the ACS Committee on Chemical Safety*; American Chemical Society: Washington, DC, 2012.
- [2] Fernández-Muñiz, B., Montes-Peón, J. M. & Vázquez-Ordás, C. J. *Journal of Safety Research* **38**, 627–641 (2007).
- [3] Cooper, M. D. & Phillips, R. A. *Journal of Safety Research* **35**, 497–512 (2004).
- [4] Hurst, N. W., Young, S., Donald, I., Gibson, H. & Muyselaar, A. *Journal of Loss Prevention in the Process Industries* **9**, 161–172 (1996).
- [5] Holizki, T., Nelson, L. & McDonald, R. *Industrial Health* **44**, 166–168 (2006).
- [6] Wurzelbacher, S. J. *et al. American Journal of Industrial Medicine* **57**, 1398–1412 (2014).
- [7] Ménard, A. D. & Trant, J. F. *Nature Chemistry* **12**, 17–25 (2020).
- [8] Kemsley, J. *Chem. Eng. News Archive* **88**, 33 (2010).
- [9] McGarry, K. A. *et al. J. Chem. Educ.* **90**, 1414–1417 (2013).
- [10] Bertozzi, C. R. *ACS Cent. Sci.* **2**, 764–766 (2016).
- [11] Armstrong, B. M. *J. Chem. Health Saf.* **26**, 65–70 (2019).
- [12] Wang, X., Thorarinsdottir, A. E., Bachrach, M. & Blayney, M. B. *ACS Cent. Sci.* **5**, 1900–1903 (2019).
- [13] The Laboratory Safety Institute. *Memorial Wall*. <https://www.labsafety.org/memorial-wall> (Accessed March 9, 2022).
- [14] The Editors of Encyclopedia Britannica. *Johann Gottlob Lehmann*. <https://www.britannica.com/biography/Johann-Gottlob-Lehmann> (Accessed March 9, 2022).
- [15] Michalovic, M. *Not-So-Great Moments in Chemical Safety*. <https://www.sciencehistory.org/distillations/not-so-great-moments-in-chemical-safety> (Accessed March 9, 2022).
- [16] Crosland, M. P. *Joseph-Louis Gay-Lussac*. <https://www.britannica.com/biography/Joseph-Louis-Gay-Lussac> (Accessed March 9, 2022).

- [17] Kingsland, J. *Robert Bunsen did a whole lot more than invent the Bunsen burner*. <https://www.theguardian.com/science/blog/2011/mar/31/robert-bunsen-burner-inventor-chemist> (Accessed March 9, 2022).
- [18] Science History Institute. *Humphry Davy*. <https://www.sciencehistory.org/historical-profile/humphry-davy> (Accessed March 9, 2022).
- [19] Wikipedia. *Humphry Davy*. https://en.wikipedia.org/wiki/Humphry_Davy (Accessed March 9, 2022).
- [20] National Academy of Sciences. *C, Significant Events in the History of Occupational Safety and Health*. 2000. <https://www.ncbi.nlm.nih.gov/books/NBK225533/> (Accessed March 9, 2022).
- [21] The United States Department of Labor. *OSH Act of 1970*. <https://www.osha.gov/laws-regs/oshact/toc> (Accessed March 9, 2022).
- [22] The United States Department of Labor. *OSHA's Small Business Success Stories*. <https://www.osha.gov/successstories> (Accessed March 9, 2022).
- [23] The United States Department of Labor. *OSHA Voluntary Protection Program Success Stories*. <https://www.osha.gov/vpp/success-stories> (Accessed March 9, 2022).
- [24] Yule, S. *Senior Management Influence on safety performance in the UK and US energy sectors*. Doctoral thesis, University of Aberdeen, Scotland. (2003).
- [25] Cooper Ph.D., M. D. *Safety Science* **36**, 111–136 (2000).
- [26] Schein, E. H. 2004. *Organizational Culture and Leadership*, 3rd ed.; Jossey-Bass: San Francisco, CA; pp 25-37.
- [27] *Dow Lab Safety Academy*. <https://corporate.dow.com/en-us/science-and-sustainability/innovation/safety-at-dow.html> (Accessed March 9, 2022).
- [28] Martin, J. A., Miller, K. A. & Pinkhassik, E. *ACS Chem. Health Saf.* **27**, 170–182 (2020).
- [29] Miller, K. A. & Tyler, K. I. *J. Chem. Health Saf.* **26**, 20–26 (2019).
- [30] The University of Chicago Office of Research and National Laboratories. *Students Lead New Lab Safety Effort*. <https://researchinnovation.uchicago.edu/2018/09/25/students-lead-new-lab-safety-effort/> (Accessed March 9, 2022).
- [31] Alaimo, P. J., Langenhan, J. M., Tanner, M. J. & Ferrenberg, S. M. *J. Chem. Educ.* **87**, 856–861 (2010).

- [32] National Research Council. *Safe Science: Promoting a Culture of Safety in Academic Chemical Research*; The National Academies Press: Washington, DC, 2014.
- [33] *University of Chicago Accident Incident Reporting (UCAIR) System*. <https://safety.uchicago.edu/tools/university-of-chicago-accident-incident-reporting-ucair/> (Accessed March 9, 2022).
- [34] Miller, A. J. M. & Tonks, I. A. *Organometallics* **37**, 3225–3227 (2018).
- [35] Reid, M., Perlmutter, S. J. & Williams, B. *ACS Chem. Health Saf.* **27**, 71–72 (2020).
- [36] Blayney, M. B., Bancroft, L., Wasson, M. C. & Williams, B. *ACS Chem. Health Saf.* **27**, 60–62 (2020).
- [37] Wood-Black, F., Schaufele, M., Dicken, R. D. & Blayney, M. B. *ACS Chem. Health Saf.* **27**, 66–68 (2020).

6.1 Appendix 6.1 – Handout for first-year training

Conflict Resolution in the Lab

Produced by the UChicago JRSI

September 2018

Conflicts can take many forms in the lab, and facing them head-on can be difficult. Keep this cheat-sheet handy to provide useful tactics for resolving lab conflicts easily and effectively!

1. When approaching a labmate about a potential safety hazard...

- Ask them about what they're doing; don't assume that they've intentionally made an unsafe decision. Most people don't intentionally want to run the risk of losing an eye, hand, etc.
- Make sure your questions are open-ended. Open-ended questions allow for you to have a conversation with your labmate as opposed to simple yes/no questions that don't get to the point. For example, "why did you do X?" instead of "did you check X?"
- Focus on the issue, not on the person. "What are you, stupid? Your condenser tube is on upside-down!" isn't nearly as effective as "Hey, are you sure your glassware is set up correctly?"

2. If a labmate gets defensive when a potential safety hazard is brought up...

- Don't start an insult war; things can escalate very quickly to a hostile situation that would affect the entire lab. Remember, regardless of the outcome, you need to continue working together in the same space, and the average PhD is 6 years.
- Remind them that it's not a personal attack, you're just concerned for their safety and the safety of your labmates. Accidents have the potential to affect many people (i.e. explosions, floods, gas leaks, fires), not just the person running a reaction or performing a technique.

3. If someone approaches you about a potential safety hazard...

- Have a conversation about it! When you talk through it, you may even figure out a better way to run your experiment.
- Remember, your labmate isn't trying to personally attack you; they're just concerned about a potential hazard. Just like when you approach someone else, focus on the issue and not on hurling insults back and forth.

4. If a labmate continually dismisses your safety concerns and is unwilling to have a conversation about what they're doing...

- Don't hesitate to escalate the issue if the situation demands it. Escalation could mean anything from talking about the issue with another labmate or your LSC to informing your PI or a representative from ORS/EHS. How you choose to escalate is entirely dependent on the situation and what you feel comfortable with – if you're unsure how to proceed, ask a JRSI member for some advice!

5. Remember your SPACE principles! Speak up, make it personal, ask open-ended questions, create an environment where people can ask questions, and escalate issues when necessary!

Appendix 6.2 – Lab Safety Contact (LSC) Responsibilities and Guidebook

The Lab Safety Contact: A Guide

Produced by the UChicago JRSI

April 2019

Contents

1	Summary of Responsibilities	2
2	Lab Safety Delegation Contract	3
3	Research Personnel Orientation Checklist	4
4	UCAIR FAQ Sheet	5
5	Sample Incident Report – September 2018	6
6	EHSA User Manual – Training	7
7	EHSA User Manual – Worker Registration	12
8	EHSA User Manual – Laboratory Placards	17
9	Conflict Resolution in the Lab	21

Quick Links



UCAIR website



EH&S Assistant



JRSI website

1 Summary of Responsibilities

The position of Lab Safety Contact (LSC) is assigned for a (renewable) one year term. All labs are recommended to have both a primary (and ideally a secondary) LSC, with the primary LSC being an older graduate student or researcher and the secondary LSC being someone newer to the lab. The official responsibilities of an LSC are:

- 1. Lab-specific training on general safety-related tasks.** This includes just about anything that isn't covered by formal training modules given by ORS and EH&S. It also can't hurt to make sure that lab members know the material covered in the formal trainings, either.
- 2. Orientation and registration of new researchers.** Whenever someone new joins the lab, it's the LSC's responsibility to go through the ORS orientation checklist (see page 4) with them and to register them with your lab in the Environmental Health and Safety Assistant (EHSA).
- 3. Lab training status and personnel info.** LSC's are given additional access in EHSA to monitor the training status of all lab members. It's the LSC's responsibility to make sure that all lab personnel update their training when necessary. Additionally, the LSC should check to make sure that all personnel are correctly entered into the EHSA system and that their info is up to date.
- 4. Liaison between your PI and ORS/LSS staff.** One of the biggest roles of an LSC is to act as a point of contact for ORS and Lab Safety Specialist (LSS) staff; this includes participating in annual inspections and ensuring that new policies/protocols are communicated to the appropriate parties.

In addition to the formal responsibilities outlined above, it's your job as an LSC to **(1)** delegate lab safety tasks to your labmates, either informally or through the use of a Lab Safety Delegation Contract (pg. 3), and **(2)** be an educational resource for everything safety-related in the lab – you should have general knowledge of proper precautions and best practices for lab techniques, and familiarity with navigating internal resources should a situation arise that you're unfamiliar with. As an LSC, your primary internal resources are:

- **UCAIR (ucair.uchicago.edu):** Used for submitting incident and near-miss reports.
- **EHSA (ehsa.uchicago.edu):** Used for waste management, training documentation, safety inspection histories, lab placards, and chemical inventory.
- **JRSI (jrsi.uchicago.edu):** Features a collection of UChicago resources as well as safety moments and links to outside resources.
- **PSD/IME Lab Safety Specialist (LSS):** Kimberly (kimberly33@uchicago.edu) is your primary point of contact for most (if not all) of your safety-related questions.
- **ORS/EH&S:** For any questions or issues that can't be fixed with the resources above, feel free to shoot an email to ORS (researchsafety@uchicago.edu) or EH&S (safety@uchicago.edu).

2 Lab Safety Delegation Contract

Lab: _____ Year: _____

The purpose of this contract is to ensure that lab safety tasks are delegated efficiently and that all lab members are aware of their responsibilities for maintaining a safe workspace. We recommend that this document be revisited at the start of Fall quarter annually to ensure that all tasks are accounted for and maintained.

Task	LSC Initials	Lab Member Initials
Submission of waste disposal requests		
Maintenance of chemical inventory		
Flushing of eyewashes		
Maintenance of lab PPE		
Monitoring sharps/broken glass containers		
Maintenance of high-hazard chemicals (specify below)		

In addition to the tasks outlined above, **all** lab members are responsible for:

1. Ensuring chemical waste from personal experiments is properly segregated and stored.
2. Checking chemical against the inventory and confirming hazards before making a purchase.
3. Writing/updating/maintaining Standard Operating Procedures (SOPs) for any specific procedures or equipment in the lab.
4. Ensuring all containers/glassware are properly labeled.
5. Maintaining a clean and safe working space within fume hoods/biosafety cabinets/on benchtops.
6. Reporting accidents and incidents/near-misses through UCAIR.
7. Ensuring yourself and other lab members are properly using PPE.

Notes: _____

PI Signature: _____ Date: _____

3 Research Personnel Orientation Checklist



THE UNIVERSITY OF
CHICAGO

Office of
Research Safety



Researcher Laboratory-Specific Orientation Checklist

EMPLOYEE INFORMATION

Name: _____ Start Date: _____
Position: _____ Principal Investigator: _____

STARTING IN THE LABORATORY

- | | | |
|--|---|--|
| <input type="checkbox"/> Provided a laboratory notebook | <input type="checkbox"/> Purchasing System | <input type="checkbox"/> Register for EHSA account |
| <input type="checkbox"/> Assigned a designated office and laboratory space | <input type="checkbox"/> Location of stockrooms | |
| <input type="checkbox"/> Introduction to Building manger | <input type="checkbox"/> Hazardous waste procedures | |

ADMINISTRATIVE CONTROLS

- | | | |
|--|--|--|
| <input type="checkbox"/> Review key policies | <ul style="list-style-type: none"> • Chemical Hygiene Plan • Biological Safety Manual • Radiation Safety Manual • EHS and Office of Research Safety websites | <ul style="list-style-type: none"> • Institutional Biosafety Committee Protocol • Animal Care and Use Protocol • Safety Data Sheets (SDS) |
|--|--|--|

REQUIRED TRAINING

- | | | |
|---|--|---|
| <input type="checkbox"/> General University Provided Training: | <ul style="list-style-type: none"> • Chemical Hygiene Plan (First time in-person) • Chemical Hygiene Plan (Annual Refresher) • Recombinant DNA at BSL-1 • Recombinant DNA at BSL-2 • Blood-borne pathogens for biomedical researchers • Biological toxins • Viral Vectors • Biological Safety Cabinets | <ul style="list-style-type: none"> • Shipping infectious substance • Radiation safety awareness • X-ray safety and awareness • Laser safety • Radioactive Material User • Radioactive Material Laboratory Designee • Irradiator Operator and Security (in-person only) |
| <ul style="list-style-type: none"> • Online training available at : ehsa.uchicago.edu/training • In-person training registration at: ehsa.uchicago.edu/trainingregistration | | |
| <input type="checkbox"/> Laboratory-specific Training | <ul style="list-style-type: none"> • Orientation Checklist • Personal Protective Equipment • Standard Operating Procedure | <ul style="list-style-type: none"> • Other : _____ • Other : _____ • Other : _____ |

EMERGENCY PROCEDURES

- | | | |
|--|--|---|
| <input type="checkbox"/> Tour of emergency equipment, including: | <ul style="list-style-type: none"> • Emergency Exits • Fire Extinguishers • Emergency Eyewash and Shower • Emergency Contact Sheet | <ul style="list-style-type: none"> • First Aid Kit • Spill Kit • Phone • UCAIR Reporting System |
| <input type="checkbox"/> cALERT (http://calert.uchicago.edu)
Uchicago's electronic emergency notification system. | | |
| <input type="checkbox"/> UC Safe app (https://safety-security.uchicago.edu/services/uchicago_safe_mobile_safety_app/) | | |

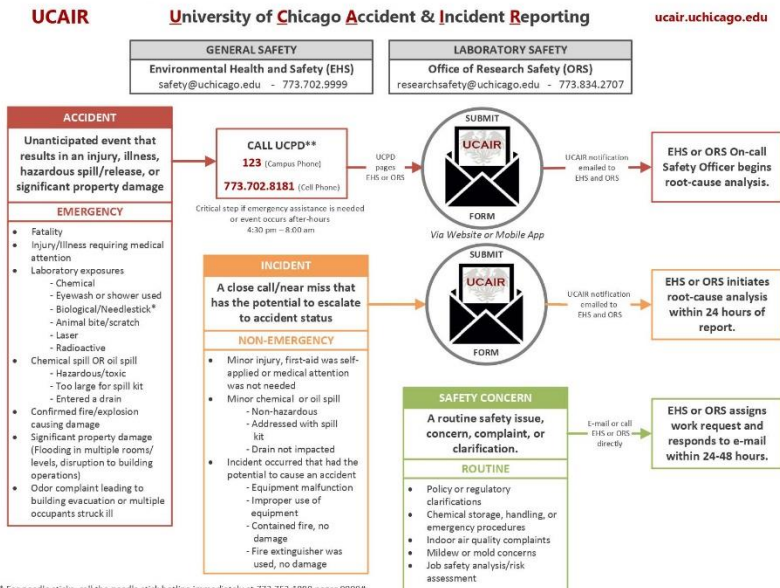
PERSONAL PROTECTIVE EQUIPMENT

- | | | | |
|------------------|--|--|---|
| Laboratory Coat: | <input type="checkbox"/> Flame Resistant | <input type="checkbox"/> Non-flame resistant | Size _____ |
| Gloves: | <input type="checkbox"/> Disposable | <input type="checkbox"/> Non-disposable | Size _____ |
| Eye Protection: | <input type="checkbox"/> Safety Glasses | <input type="checkbox"/> Safety Goggles | <input type="checkbox"/> Prescription Safety Lenses |

ENGINEERING CONTROLS

- Fume hoods Biosafety Cabinet Other: _____

4 UCAIR FAQ Sheet



FAQs
<p>Q: Where can I submit a report? A: Download the UCAIR mobile app (iOS or Android) or go to ucair.uchicago.edu to submit a report online and learn more about UCAIR. The UCAIR link is also present on the websites of both safety offices (EHS and ORS).</p> <p>Q: Do I need to login to UCAIR? A: No. Anyone can access the UCAIR tool and submit a report.</p> <p>Q: Can I report an accident/incident anonymously? A: Yes. However, anonymous reporting is only for events that do not require medical attention. If a University employee sustains an injury requiring medical attention they must follow the Human Resources Policy 525 – Workers' Compensation and complete three forms with their supervisor. If you are reporting a non-injury anonymously, please be as detailed as possible to ensure we can locate the area to determine the root cause.</p> <p>Q: I work in a Medical Center building, does the process change? A: Yes. Call Public Safety at 773.702.6262 to report all emergencies in the Medical Center and follow their reporting procedures. If you are a University employee, then you can submit a report using the UCAIR tool.</p> <p>Q: If I submit a report to UCAIR, does it also notify UCPD? A: No. The UCAIR tool only sends a notification to the main email boxes of the safety offices (EHS and ORS). In the event of an emergency call UCPD at 123 or 773.702.8181 to ensure proper emergency response procedures are triggered (e.g., UCPD pages: On-call engineer, On-call Safety Officer for EHS and/or ORS, Dean On-call if students are involved, etc.).</p>

FAQs
<p>Q: Why should I use UCAIR? A: Your UCAIR report will allow the safety offices to follow-up and determine the root cause of an accident/incident, which can drive change and eliminate future occurrences.</p> <p>Q: What is the difference between UCAIR and UCARE? A: UCAIR is a system for submitting a report about any accident/incident that occurs on campus or work-related injuries at off-campus locations. UCARE is the University of Chicago Alcohol Risk Reduction Education Program that is managed by Student Health and Counseling Services (SHCS).</p> <p>Q: Does this replace the whistleblower hotline? A: No. Please call the University's whistleblower hotline at 1.800.971.4317 to report unethical or inappropriate behavior.</p> <p>Q: How do I know whether to report something? A: All accidents/incidents should be reported no matter how minor. Reporting of accidents/incidents helps identify the cause and prevent future occurrences. If in doubt, report it.</p> <p>Q: When should I not use the UCAIR system? A: UCAIR's main goal is to eliminate preventable injuries and significant accidents that impact university employees or disrupt facility operations on a large scale. Do not use UCAIR to report crimes, building maintenance issues, condensation, musty odors, mold/mildew, nor nuisance odors related to food/cooking. Contact Facilities Services or Physical Plant for all building related maintenance issues and the appropriate safety office for routine safety work requests. Contact Environmental Health and Safety for non-lab related issues and the Office of Research Safety for lab related issues.</p>

Contact Information
<p style="text-align: center;">Laboratory Safety</p> <p>Questions regarding UCAIR in research labs or lab activities? Contact your LSS first. Laboratory Safety Specialists (LSS)</p> <p>BSD Labs Jeff Melton.....773.834.1171 Jay Schroeder.....773.834.1202</p> <p>PSD/IME Labs Kimberly Mormann.....773.834.2121</p> <p>SSD Labs Mike McCarthy.....773.834.4350</p> <p>Office of Research Safety researchsafety@uchicago.edu 773.834.2707</p> <p>Radiation Safety 773.702.6299</p>
<p style="text-align: center;">General Safety (Non-Lab)</p> <p>Questions in University buildings (non-lab activities), construction sites, and campus grounds?</p> <p>Environmental Health and Safety safety@uchicago.edu 773.702.9999</p>
<p style="text-align: center;">Building Issues</p> <p>For non-emergency building issues or building maintenance requests, contact your facility operations group to submit a work order. If you have a facility manager contact them first, they may be able to provide assistance and coordinate building-wide requests.</p> <p>Facilities Services.....773.834.1414</p> <p>Physical Plant.....773.702.6295</p>

5 Sample Incident Report – September 2018

September 2018 Dept. of Chemistry/IME Incidents

Date	Type	Description	Recommendations
9/7/2018	Near Miss	ORS was contacted about old chemicals with crystal formation on outside of container	<ul style="list-style-type: none"> Avoid storage of incompatibles in the same cabinet Minimize storage of non-flammables inside flammable cabinets
9/18/2018	Exposure	Undergraduate received exposure to HF-pyridine when needle separated from syringe.	<ul style="list-style-type: none"> Keep sash as low as possible when working Hold the needle and syringe when adding or use Luer lock syringes Consider additional PPE (face shield) when high hazard chemicals are used
9/28/2018	Flood	Leak from fume hood sink on 4 th floor East GCIS caused damage and mold growth all the way on 2 nd floor	<ul style="list-style-type: none"> Contact Facilities Services at first sign of leak

Other campus events suggesting a trend

Type	Description	Recommendations
Flood	Leaks from fume hoods sinks cause damage to floors below (twice)	<ul style="list-style-type: none"> Contact Facilities Services (773.834.1414, urgent request) at first sign of leak
Exposure	Needle stick from overfilling sharps containers (numerous overfilled containers were found in lab and adjacent lab spaces)	<ul style="list-style-type: none"> Replace sharp containers when full Do not shake sharp containers to lower level of sharps Know how to use the Needle Stick hotline Inform physician of hazards you work with when an exposure occurs

6 EHSA User Manual – Training

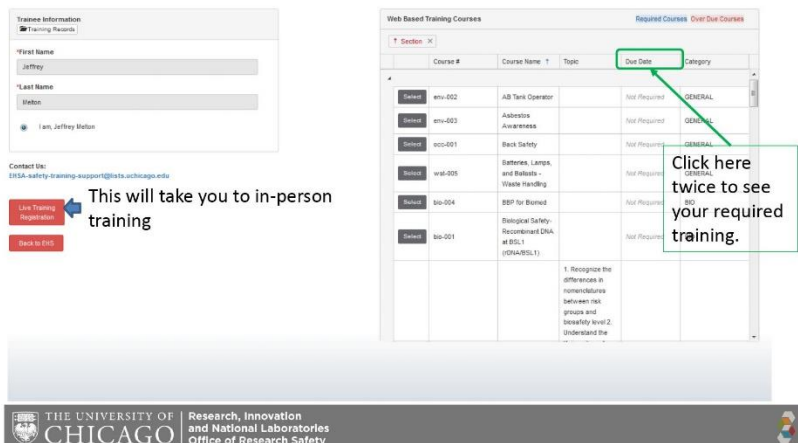


EHSA User Manual – Training

Completing Web-Based Training
& Registering for In-Person Training



<https://ehsa.uchicago.edu/training>
For Web Training Courses



Training Information

Training Search

*First Name
jeffrey

*Last Name
Hebin

I am, Jeffrey Hebin

Contact Us:
EHSA-safety-training-support@ehsa.uchicago.edu

[Link Training Registration](#) This will take you to in-person training

[Back to EHSA](#)

Web Based Training Courses Required Courses Over Due Courses

Course #	Course Name	Topic	Due Date	Category
env-002	AB Tank Operator		Not Required	GENERAL
env-003	Asbestos Awareness		Not Required	GENERAL
occ-001	Back Safety		Not Required	GENERAL
wel-005	Extruder, Lamps, and Belts – Waste Handling		Not Required	GENERAL
bio-004	SSP for Bioreactor		Not Required	GEN
bio-001	Biological Safety Recombinant DNA at BSL-1 (GDA-BSL-1)		Not Required	GEN

1. Recognize the differences in nomenclatures between the groups and biosafety level 2. Understand the

Click here twice to see your required training.

Trainee Information

Training Records

*First Name
Jeffrey

*Last Name
Melton

Station
I am, Jeffrey Melton

Contact Us:
EHS&S-safety-training-support@lists.uchicago.edu

Live Training Registration

Back to EHS

Web Based Training Courses

Required Courses Over Due Courses

Section	Course #	Course Name	Topic	Due Date	Category
Select	rad-005	X-ray Safety and Awareness		11-16-2021	RAM
Select	rad-004	Radiation Safety Awareness		11-16-2019	RAM
Select	rad-002	Radioactive Material User Refresher		11-16-2019	RAM
Select	fu-001	Fire Safety and Evacuation		12-06-2019	GENERAL
Select	asb-003	Asbestos Awareness		Not Required	GENERAL
Select	os-001	Back Safety		Not Required	GENERAL
Select	wh-001	Batteries, Lamps, and Solvents - Waste Handling		Not Required	GENERAL
Select	bio-001	Biological Safety: Recombinant DNA at DSL1 (GCRABESGL1)		Not Required	BIO

Required training that has been completed

Training that needs to be completed

Optional Training - Not Required

Click Select to take the training

THE UNIVERSITY OF CHICAGO | Research, Innovation and National Laboratories Office of Research Safety

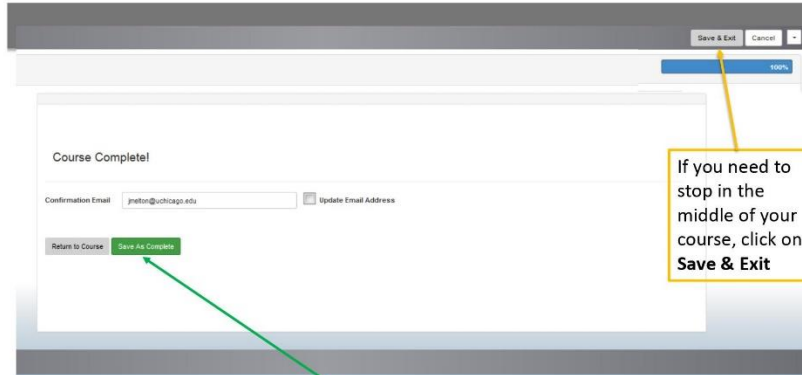
If you stopped taking a course part way through, this message will pop up. Click **Continue** to pick up where you left off. Click **New Course** to start from scratch.

Continue Previous Session

You have a previously unfinished course. Would you like to Continue OR start a New Course.

New Course Continue

THE UNIVERSITY OF CHICAGO | Research, Innovation and National Laboratories Office of Research Safety



Once you have gone through the course, make sure your email is correct, Then click **Save As Complete** to record your progress.



Now the training is marked as complete

Trainee Information

Training Records

*First Name
Jeffrey

*Last Name
Meton

I am, Jeffrey Meton

Contact Us:
EHS&A safety training support@lists.uchicago.edu

Live Training Registration

Back to EHS

Web Based Training Courses

Section	Course #	Course Name	Topic	Due Date	Category
Select	rad-005	X-ray Safety and Awareness		11-16-2021	RAM
Select	fs-001	Fire Safety and Evacuation		12-06-2019	GENERAL
Select	rad-004	Radiation Safety Awareness		11-16-2019	RAM
Select	rad-002	Radioactive Material User Refresher		11-16-2019	RAM
Select	env-003	Ashleton Awareness		Not Required	GENERAL
Select	ooc-001	Back Safety		Not Required	GENERAL
Select	wab-005	Substanc, Lamps, and Balasts - Waste Handling		Not Required	GENERAL
Select	bs-001	Biological Safety, Recombinant DNA at BSL-1 (OR&MSL1)		Not Required	BSL

This will take you to in-person training

On the next page, you will see how to register for in-person training



<https://ehsa.uchicago.edu/trainingregistration>
For In-Person Training Courses

Click here to see sessions you have registered for

Traine Information
 Training Records
 *First Name: Jeffrey
 Last Name: Nelson
 I am, Jeffrey Nelson

Contact Us:
 EHS&A safety training support@ehsa.uchicago.edu
 On Site Training
 EHS&A Home Page

This will take you to web training

To sign up for a course session, click the Register button

Upcoming Training Sessions	Date	Start Time	End Time	Session Location	Status	
Asbestos Awareness	Register	03-07-2019	01:00:00 PM	03:00:00 PM	5225 S. Cottage Grove Ave., Room 201	36 Spaces Open.
Back Safety	Register	01-24-2019	01:00:00 PM	02:00:00 PM	F5-Service Bldg. 5225 S. Cottage Grove, Room 201	35 Spaces Open.
Chemical Hygiene Plan - Laboratory Safety (in person)	Register	01-08-2019	12:00:00 PM	01:15:00 PM	CLSC 617	8 Spaces Open.
	Register	01-22-2019	12:00:00 PM	01:15:00 PM	CLSC 617	12 Spaces Open.
	Register	12-19-2018	12:00:00 PM	01:15:00 PM	CLSC 181	24 Spaces Open.
Comprehensive Biosafety Training	Register	01-22-2019	01:15:00 PM	04:00:00 PM	CLSC 617	11 Spaces Open.
	Register	01-08-2019	01:15:00 PM	04:00:00 PM	CLSC 617	12 Spaces Open.
	Register	12-11-2018	01:15:00 PM	04:00:00 PM	CLSC 617	9 Spaces Open.
Confined Spaces	Register	03-14-2019	09:00:00 AM	10:00:00 AM	5225 S. Cottage Grove Ave., Room 201	34 Spaces Open.

Click Confirm to reserve a space in the training session

Registration Confirmation

Are you sure you want to register for this Session?
 Current Status: 36 Spaces Open.

Register Confirm Cancel

Click **Un-Register** if you cannot attend the training session

Click here to see other sessions that are available

Training Information

Training Records

First Name: Jeffrey

Last Name: Jackson

I am, Jeffrey Jackson

Contact Us: EHS&S safety training support@state.uchicago.edu

[On-Rite Training](#)


[EHS&S Home Page](#)

Upcoming Training Sessions [View All Sessions](#) [Expand](#) [Collapse](#)

	Date	Start Time	End Time	Session Location	Status
Asbestos Awareness	03-07-2019	01:00:00 PM	03:00:00 PM	5225 S Cottage Grove Ave., Room 201	25 Spaces Open.

Once you attend and complete the training session, the completion will be recorded by the instructor who is leading the training

7 EHS User Manual – Worker Registration



EHS User Manual – Worker Registration

Adding and Removing researchers
from your lab



What is a PERMIT?

Every PI in EHS has at least one Permit. A permit defines the who, what, and where of the PI's lab. People listed on a PI's permit can see the lab's chemical inventory and inspection results, while the PI and LSC can track their training status.

This will only deal with CHEM permits. To add someone to your IBC protocol, please submit a Personnel / Funding Amendment using [AURA IBC](#)



Once you log in, you will be on the Main Menu of EHS
Left-Click here to **view** your lab's permits



Worker Registration

You can add and remove workers from your lab's permit using **Worker Registration**. All action in Worker Registration require approval from the Office of Research Safety to taking effect.

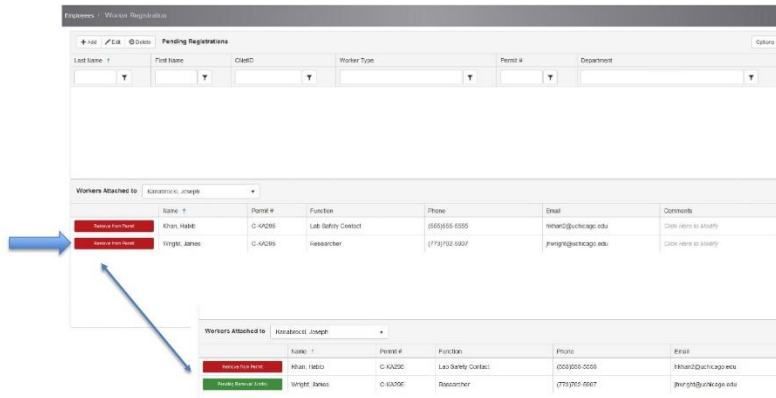
Only people with **PI / Alternate** access can use this feature (typically Principal Investigators or Lab Safety Contacts).



Once you log in, you will be on the Main Menu of EHS
 Double-Click **Worker Registration** here



To Remove Workers, click the red button next to their names labeled **Remove from Permit**. The button will turn green. To undo a removal, click the green button next to the name.

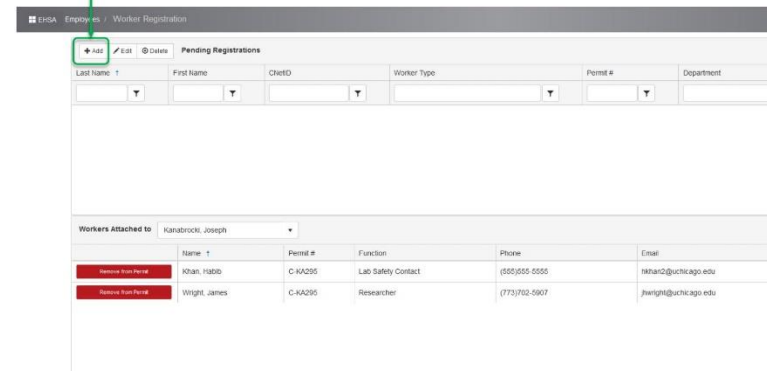


Before Adding a Worker

- Find the worker's CNetID and ChicagoID
 - Most emails are CNetID@uchicago.edu
 - ChicagoID on back of University ID (8 numbers & 1 letter)
- Whoami.uchicago.edu
 - Search by Name, CNetID, or ChicagoID



Click **+Add** to request a worker to be added to your permit



Worker Registration

This is the **Worker Addition** screen. First, try entering the new worker's last name in the **Last Name** field.

This will search for any person already in the system who has the same last name.

Here you can see the PI and permit. If you would like this worker to be a new Lab Safety Contact, make sure to select that option under **Function**. Otherwise, leave it blank.

THE UNIVERSITY OF CHICAGO | Research, Innovation and National Laboratories Office of Research Safety

After you search for a person's last name, it will populate the other required fields like CNetID. Please check to make sure you have the right person.

We are adding Hsiang-Ming Wang, who has the CNetID anthonywang. Since the CNetIDs match, we know we have the right person.

You may need to fill out more details here, like the email address and department.

Save If the worker is not found when you search by last name, enter the worker's data that you looked up on Whoami. Incorrect information can result in delays, so strive for accuracy. Avoid entering any extra spaces.

You can still request for the worker to be a lab safety contact here

Make sure to **Save** the worker after you are done!



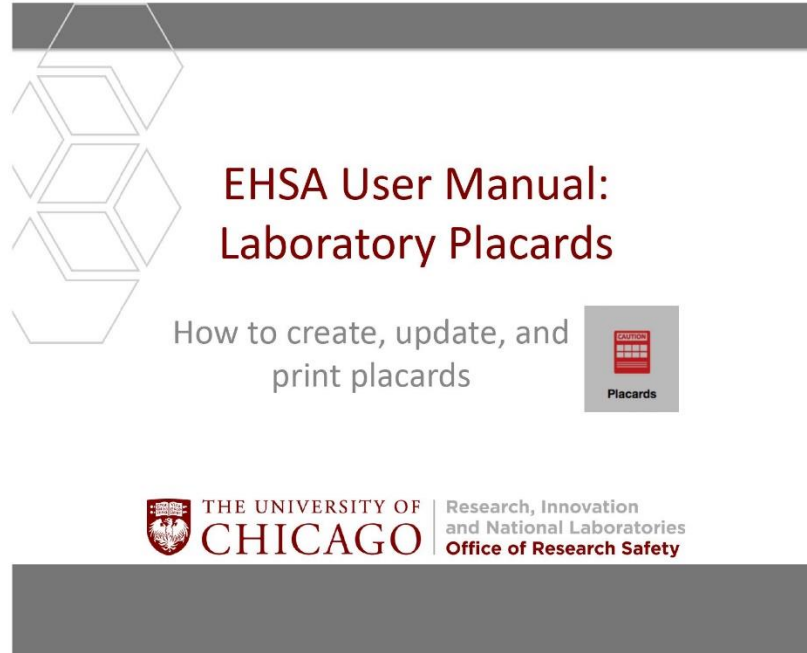
Once a worker registration is saved, you will be sent back to the Worker Registration menu. If you click once on one of the names, that will **highlight** that row. You will then be able to edit or delete the worker addition request by clicking the appropriate button. You can also double-click a name to edit the worker addition request.

Last Name	First Name	CNetID	Worker Type	Permit #	Department
Melton	Jeffrey	jmelton	Researcher	C-8A206	Office of Research Safety
Wang	Huiqing	hwanghqsq	Researcher	C-8A206	Office of Research Safety

Workers Attached to: Karabochi, Joseph						
Worker Name	Permit #	Function	Phone	Email	Comments	
Huan, Hailin	C-8A206	Lab Safety Contact	(312) 235-2335	hmhuan@uchicago.edu	Link Here to Activity	
Wang, JINXI	C-8A206	Researcher	(773) 752-5827	hwangh@uchicago.edu	Show Here to Activity	

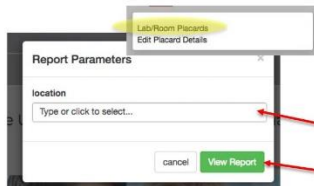


8 EHSA User Manual – Laboratory Placards



Two options are displayed when left clicking on the “Placard”:

- **“Lab/Room Placards”**: print placards for lab/rooms
- **“Edit Placard Details”**: update information on the placard

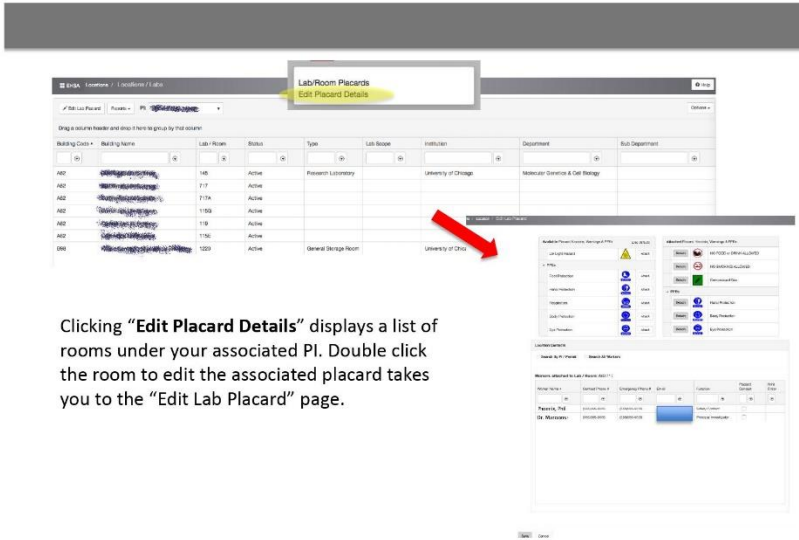


To print an existing placard, click the **“Lab/Room Placards”** link and the **“Report Parameters”** link pops up.

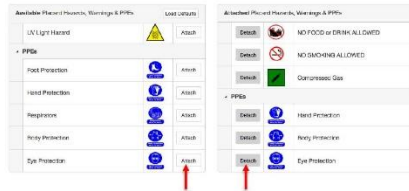
Click to display all rooms or type room number to search.* once the desired room is selected, click **“View Report”**

* If the room number does not appear in the dropdown, contact ORS for support.





Clicking “Edit Placard Details” displays a list of rooms under your associated PI. Double click the room to edit the associated placard takes you to the “Edit Lab Placard” page.



On the top of the “Edit Placard Page” the available hazard warning signs and PPEs are displayed

Use the “Attach”/”Detach” buttons to add/remove safety warning icons on the placard

For a wet research lab, the followings icons must be selected: **NO FOOD or DRINK ALLOWED, NO SMOKING ALLOWED, Hand Protection, Body Protection, and Eye Protection.** Consult with ORS if you are uncertain whether certain hazard is applicable.

Location Contacts

Search By PI / Permit Search All Workers

Workers attached to Lab / Room: A62-717

Worker Name	Contact Phone #	Emergency Phone #	Email	Function	Placard Contact	Print Order

On the bottom “Location contact” section, the information of the responsible “Principal Investigator” and a Laboratory “Safety Contact” (as applicable) must be selected.



Location Contacts

Search By PI / Permit Search All Workers

PI: [Dropdown] Permit #: [Dropdown]

Worker Name: [Search] [Clear]

Worker: [Dropdown] PI: [Dropdown] Permit #: [Dropdown]

Workers attached to [Dropdown]

Check "Search By PI/Permit" box allow quick access to everyone listed under your associated PI

To properly display all associated personnel, select the permit number that begin with "C-".**

Location Contacts

Search By PI / Permit Search All Workers

Begins With Contains Equals

Worker Name: [Text Input] [Search] [Clear]

Alternatively, checking the "Search All Workers" box allow you to find anyone in the system.**

The results of your search will be displayed on the lower left with an "Attach" button for adding the corresponding person to the placard

PI: Dr. Maroons
Permit #: C-1234

Worker Name	Attach
Phoenix, Phil	Attach
[Redacted]	Attach
[Redacted]	Attach

Worker Name Contains "phi"

Worker Name	Attach
Phoenix, Phil	Attach
[Redacted]	Attach
[Redacted]	Attach

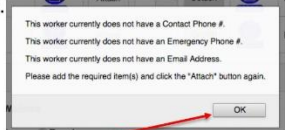
** If you are unable to find the name using either method, contact ORS for support.



Worker Name Contains "phi"

Worker Name	Attach
Phoenix, Phil	Attach
[Redacted]	Attach
[Redacted]	Attach

Clicking the "Attach" button will add the information of the selected individual onto the placard. However, if emergency contact of this individual is not present, the following error will be shown*.



Click "OK" and complete the Contact Phone # (campus phone number), Emergency Phone # (off campus number), and Email Address**.

Contact Phone #: [Text Input] Emergency Phone #: [Text Input]

Email Address: [Text Input]

Worker Name Contains "phi" Workers attached to Lab / Room: [Dropdown]

Worker Name	Contact Phone #	Emergency Phone #	Function
Phoenix, Phil	[Text Input]	[Text Input]	[Text Input]
[Redacted]	[Text Input]	[Text Input]	[Text Input]

Click "Attach" again once the contact information is updated. All three fields are required.

* You may see less errors than the one shown. Error is triggered only for information not currently in the system. Once updated, the phone numbers and email address will be saved and can be edited under each person's profile.
 ** If there is an error in your contact information, you need to edit your user profile. For detail instructions, see EHS User Manual- User Profile Maintenance



Workers attached to Lab / Room: **4021186**

Worker Name	Contact Phone #	Emergency Phone #	Email	Function
Detach Dr. Maroons	(555)555-5555	(555)555-5555	555555555555	Principal Investigator
Detach Phoenix, Phil	(111)111-1111	(111)111-1111		Safety Contact

Function	Placard Contact	Print Order
Principal Investigator	<input checked="" type="checkbox"/>	1
Safety Contact	<input type="checkbox"/>	2

After attaching all personnel, add "Function" associated to each personnel by clicking on the blank space under the "Function" column and select either "Principal Investigator" or "Safety Contact"

You can also specify the order of the names on the placard using the "print order" column to the right

Each person MUST have a "Function" to be properly displayed on the placard.

Up to 8 names can be displayed on a single placard with any combination of Principal Investigators and Safety Contacts



After editing the placard, you may return to the home page and use the "Room/Lab Placards" link to print the placard. Each room need to be edited separately.

9 Conflict Resolution in the Lab

Conflicts can take many forms in the lab, and facing them head-on can be difficult. Keep this cheat-sheet handy to provide useful tactics for resolving lab conflicts easily and effectively!

1. When approaching a labmate about a potential safety hazard...

- Ask them about what they're doing; don't assume that they've intentionally made an unsafe decision. Most people don't intentionally want to run the risk of losing an eye, hand, etc.
- Make sure your questions are open-ended. Open-ended questions allow for you to have a conversation with your labmate as opposed to simple yes/no questions that don't get to the point. For example, "why did you do X?" instead of "did you check X?"
- Focus on the issue, not on the person. "What are you, stupid? Your condenser tube is on upside-down!" isn't nearly as effective as "Hey, are you sure your glassware is set up correctly?"

2. If a labmate gets defensive when a potential safety hazard is brought up...

- Don't start an insult war; things can escalate very quickly to a hostile situation that would affect the entire lab. Remember, regardless of the outcome, you need to continue working together in the same space, and the average PhD is 6 years.
- Remind them that it's not a personal attack, you're just concerned for their safety and the safety of your labmates. Accidents have the potential to affect many people (i.e. explosions, floods, gas leaks, fires), not just the person running a reaction or performing a technique.

3. If someone approaches you about a potential safety hazard...

- Have a conversation about it! When you talk through it, you may even figure out a better way to run your experiment.
- Remember, your labmate isn't trying to personally attack you; they're just concerned about a potential hazard. Just like when you approach someone else, focus on the issue and not on hurling insults back and forth.

4. If a labmate continually dismisses your safety concerns and is unwilling to have a conversation about what they're doing...

- Don't hesitate to escalate the issue if the situation demands it. Escalation could mean anything from talking about the issue with another labmate or your LSC to informing your PI or a representative from ORS/EHS. How you choose to escalate is entirely dependent on the situation and what you feel comfortable with – if you're unsure how to proceed, ask a JRSI member for some advice!

5. Remember your SPACE principles! Speak up, make it personal, ask open-ended questions, create an environment where people can ask questions, and escalate issues when necessary!

Appendix 6.3 – Peer Lab Walkthrough Scoring Rubric 2019

JRSI's Peer Lab Walkthrough Competition

April 2019

Volunteer Instructions

1. Contacts and Escorts

- A. You will be escorted through the lab by a member of the lab, preferably the Lab Safety Contact (LSC) if available. This escort will be your primary point of contact during the walkthrough.
- B. A member of the JRSI will accompany you, but you will be the primary scorer.
- C. The volunteer should direct all questions to the escort, not to other lab members.

2. Walkthrough Process

- A. In general, do not extensively look through and open all drawers and cabinets in the lab.
- B. Ask directed questions and look in specific locations (*e.g.*, ask the escort where the primary chemical storage is, and then look specifically in that location).
- C. Inspect any storage space that carries a higher safety significance (*e.g.*, flammables cabinet).
- D. If the participating group shares their lab space with another group (without walls or doors for separation), ask which portion(s) of the lab is (are) used by the participating group. Conduct your evaluation *only* on this portion of the shared lab space.
- E. Labs should have extra goggles for visitors, but they should not be expected to have extra fireproof lab coats.
- F. Ask where documentation is kept (*e.g.*, SOP, SDS) and ask to see a few examples. Accessible, recently updated documentation is sufficient evidence for lab member awareness; Individual lab members do not need to be questioned.

3. Scoring

- A. The base score for each category is a 3; this baseline represents the minimal standards for safe operation that adheres to ORS guidelines. Points can be added or removed from this baseline.
- B. Do not award half points. If you are between points, use your best judgment.
- C. If you are unsure which score to award, err on awarding the higher score.
- D. In general, look for reasons to add points rather than for reasons to deduct points.
- E. Avoid the appearance of being overly-critical or of searching for reasons to deduct points (*i.e.*, do not look for very small infractions or go through every drawer).
- F. If a category does not apply to a group, do not score it.

- G. If awarding a 1 or a 5, provide a brief description of why you gave that score (no more than a sentence is required). For other scores, a short description would be helpful but is not necessary.
- H. Base your evaluation only on the participating group; Do not give significant weight to anything that is the result of a different research group.
- I. Score the group's laboratory space collectively. Each group should get one score per rubric category, regardless of how many different labs they have. If a category applies to multiple lab spaces, each lab space does not need to carry equal weight when determining the overall score.
- J. If something is broken (*e.g.* low flow eyewash or low hood airflow) but a work order has been properly submitted for the repair, consider it to be in acceptable working order.
- K. The two bonus categories allow for labs to be scored either positively or negatively for significant things that are not accounted for on the rubric. If something is not covered by the rubric but you see something significant (either good or bad), use these bonus categories to award or remove discretionary points. Please provide an explanation for your scoring in these categories for all scores (*i.e.* not just 1 or 5).

4. Volunteer Safety

- A. Bring your own PPE with you (safety glasses, lab coat, *and* gloves); the JRSI member that is accompanying you will store your PPE in a bag in order to give the lab a chance to offer you PPE. If you are not offered PPE, the JRSI member will give you your stored PPE.
- B. If you at any point feel unsafe in a lab, leave immediately. If possible, please discuss your reason for leaving with the lab escort and/or the LSC.

General Safety

Signage, PPE, SOPs, Organization, etc.

<i>Safety Item</i>	<i>Score Guide</i>	<i>Explanation</i>
PPE (Personal Protective Equipment)	1	Lacking or incorrect PPE for present lab hazards, PPE in poor condition, improperly stored PPE, or PPE not worn
	2	Correct PPE but not properly worn
	3	Clean, correct, and complete PPE worn
	4	All researchers are provided with and are wearing correct PPE, and PPE is available for visitors
	5	All researchers are provided with and are wearing PPE, as are all visitors; Lab members insist everyone, even visitors, wear PPE, and PPE is well-organized and accessible
Lab Signage (Emergency contacts, PPE requirements)	1	No signage
	2	Present, but out of date or missing information
	3	Up to date signage, contains all required information (hazards, contact information)
	4	Provides all signage necessary; Information is presented efficiently, or extra details given
	5	Signage is exceptional and inspiring for improvement for other labs, contains useful information/formatting not seen in most labs
Aisles and Hallways	1	Clutter blocking exits or safety equipment, trip/injury hazard
	2	Clutter, but no obvious risk presented (“organized mess” away from walkways, doorways, etc.)
	3	Well-organized with no potential risk
	4	Innovative ideas on using the space for efficiency
	5	Innovative ideas on using the space for efficiency; considers possible risk and provides preventative, proactive solutions

Eyewashes	1	Eyewash not functioning correctly, hasn't been reported; No identifying signs; Inaccessible; Hasn't been checked monthly within the last six months	<i>Required for 1,5</i>
	3	Checked monthly and in good working order, accessible; Not functioning correctly, but has been reported	
	5	Checked weekly, results recorded, accessible, and water is clean	

Food and Drink	1	Food drink present in lab, food or drink items present in trash located in lab	<i>Required for 1,5</i>
	5	No food or drink items present	

Electronics	1	Electronics are placed in unsafe locations and are not safely connected (<i>e.g.</i> , power strips on floor)	<i>Required for 1,5</i>
	2	Electronics are placed in safe locations, but are not safely connected (<i>e.g.</i> , power strips above floor)	
	3	Electronics are placed in safe locations, and are safely connected—no daisy chaining, (<i>i.e.</i> , multiple surge protectors are not plugged into each other)	
	4	Electronics are safely placed and connected; Those not in use are unplugged or put away	
	5	Electronics are safely placed and connected with good organization; Those not in use are unplugged or put away	

SOPs (Standard Operating Procedures)	1	No SOPs, or location is unknown	<i>Required for 1,5</i>
	2	Some SOPs but needs additional	
	3	All SOPs available and organized	
	4	SOPs are available and near the process used	
	5	SOPs are current, near where they are used and thoroughly written	

SDSs (Safety Data Sheets)	1	No way to access SDSs in the lab or office (either on paper or online)	<i>Required for 1,5</i>
	2	No convenient way to access SDSs in the lab	
	3	Online SDSs can be easily accessed in the lab	
	4	Can easily access online SDSs and a collection of hard copy SDSs for high hazard chemicals exists	
	5	Can easily access online SDSs and a full collection of recently updated hard copy SDSs for high hazard chemicals exists	

Organization	1	Potential accidents imminent (<i>e.g.</i> , bottles on shelf edges, heavy items that could easily fall on researchers, unsecured water lines), corrosives above eye level	<i>Required for 1,5</i>
	2	An organizational method exists, but items are not routinely placed based on this system, and/or an organizational method exists and is followed, but the system poses risks	
	3	All heavy/hazardous/liquid chemicals stored below eye level or secured so that they cannot fall on researchers; Organization in the rest of the lab could be improved to minimize risks	
	4	Most risks addressed where items are accessible, but organization could be improved; Glass containers stored below eye level	
	5	Risks addressed so that items stored up high are secured so that they can't fall on researchers and have a safe method to reach them (<i>e.g.</i> , stepladders, if necessary); Glass containers stored below eye level	

Chemical Storage Safety

Chemical Segregation, etc.

<i>Safety Item</i>	<i>Score Guide</i>		<i>Explanation</i>
Samples and Non-Commercial Chemicals	1	No information	<i>Required for 1,5</i>
	2	Some information provided but incomplete description; No hazards communicated	
	3	Description and hazard of contents labeled	
	4	All samples and chemical labels complete and clearly legible	
	5	Trays and shelves are labeled with the relevant hazard class, if relevant; Details sample hazards and contact information in case of emergency	

Secondary Containment	1	Lack of secondary containment; Spills might create a serious hazard	<i>Required for 1,5</i>
	2	Some liquids and chemicals especially larger than 0.5 L are not in secondary containment or secondary containment is not appropriate (too small or may have holes, <i>etc.</i>)	
	3	Liquids and chemicals stored in correctly sized secondary containment especially those greater than 0.5 L	
	4	All liquids > 0.5 L and chemicals stored in appropriate secondary containment. All smaller vials are also in secondary containment as well	
	5	All liquids and chemicals stored in appropriate secondary containment. All smaller are also in secondary containment as well as storage of glass solid containers. Broken glass boxes protected from water by secondary containment.	

Chemical Hazards	1	No organization of chemicals; Observation of incompatible materials stored next to each other (<i>e.g.</i> , NaOH with HCl, oxidizers with explosives)	<i>Required for 1,5</i>
	2	A chemical organizational system exists, but it prioritizes convenience over hazards (<i>e.g.</i> , chemicals organized by element or alphabetical)	
	3	Chemicals stored and labeled separately according to broad hazard classes (<i>e.g.</i> , there are shelves or cabinets for different hazard classes, which are labeled)	
	4	Minor hazard classes are also indicated (<i>e.g.</i> , in the category of acid, organic acids and oxidizing acids should be separate)	
	5	All of the things observed in 4 plus: clear labels (and warning signs when necessary) of chemical hazard class in storage area	

Waste Safety

Labeling, Storage, Sharps, etc.

<i>Safety Item</i>	<i>Score Guide</i>		<i>Explanation</i>
Sharps	1	Sharps left out on benchtop, no sharps container, container over fill line, capped needles in sharps container	<i>Required for 1,5</i>
	3	Sharps properly stored and covered, sharps container in lab	
	5	All sharps are properly disposed of, sharps container is not full, empty sharps container readily available, instructions for disposal present	

Waste Storage	1	Observations of many waste containers that are either unlabeled, uncapped, or not contained in a secondary container	<i>Required for 1,5</i>
	2	Waste bottle labels are incompletely labeled (<i>i.e.</i> , missing hazards, missing category, <i>etc.</i>); Observation of some waste containers that are incorrectly capped, labeled, or contained in secondary containers, but most waste is stored according to 3	
	3	Waste labeled and capped/sealed appropriately, waste in secondary containers	
	4	Includes all for a score of 3 plus: good workflow of waste management; waste segregated by categories	
	5	Includes all for a score of 4 plus: Excellent workflow of waste management (<i>i.e.</i> , designated waste accumulation area and storage area with clear instructions, details on yellow waste tag including all info needed)	

Equipment Safety

Hoods, Gas Cylinders, Lasers, etc.

<i>Safety Item</i>	<i>Score Guide</i>		<i>Explanation</i>
Lasers	1	No containment	<i>Required for 1,5</i>
	3	Beams are well contained when maintenance/alignment is not in progress	
	5	Beams are fully contained, containment is segmented to limit the loss of containment while working, containment without interlock is labeled	

Hoods	1	Nearly all or all hood sashes open even when no one is working in the hood	<i>Required for 1,5</i>
	2	Some hood sashes open even when no one is working in the hood.	
	3	Most hood sashes closed or below noted level when not in use, as low as practical when in use	
	4	One or two hood sashes as low/closed as practical when in use, lowered/closed when not in use; Back panels or airflow is free from obstructions	
	5	No hood sashes open more than recommended level. Back panels or airflow is free from obstructions; Blast shields have been added appropriately	

Gas Cylinders	1	Cylinders not stored vertically or not secure, not sorted by hazard classification (e.g., hydrogen and oxygen together)	<i>Required for 1,5</i>
	2	Cylinders poorly secured (not permanent structure, or more than three with one strap/chain), but sorted by hazard classification	
	3	Cylinders are secured but not clearly labeled, sorted by hazard classification	
	4	Cylinders are secure and properly labeled	
	5	Cylinders are clearly labeled with contents and hazards, firmly and individually attached to a permanent structure, flammables are far away from sources of combustion	

Bonus

Discretionary Points.

<i>Safety Item</i>	<i>Score Guide</i>		<i>Explanation</i>
	1	Accidents inevitable	<i>Required for 1,2,3,4,5</i>
	2		
	3	Minimum requirements for safe operation	
	4		
	5	Creative, innovative, proactive solutions that go above and beyond	

	1	Accidents inevitable	<i>Required for 1,2,3,4,5</i>
	2		
	3	Minimum requirements for safe operation	
	4		
	5	Creative, innovative, proactive solutions that go above and beyond	

CHAPTER 7.

CONCLUSIONS

Section 7.1: Summary of findings and comments

In this work, I have described experiments aimed at elucidating the physiological role of α -synuclein, an intrinsically disordered protein found primarily in neurons which is believed to play a role in a number of neurodegenerative diseases like Parkinson's, dementia with Lewy bodies, and multiple system atrophy. These experiments included (1) an exploration of the impact of osmotic tension, lipid tail composition, and lipid packing defects on the equilibrium binding properties of α Syn, and (2) elucidating the behavior and polymeric activity of the C-terminal domain, whose putative function *in vivo* has yet to be well defined. The former experiments were carried out using a novel experimental procedure whereby α Syn binding to model vesicles was measured using confocal microscopy and a robust colocalization analysis, whereas the latter utilized high-energy x-ray methods to probe the depletion-induced force response of α Syn-coated SSLBs. Taken together, these experiments demonstrate the many complexities informing our understanding of α Syn's normal physiological behavior, and these multitude complexities were contextualized within the synaptic vesicle cycle in which α Syn is hypothesized to participate.

The results obtained using the confocal binding assay to quantify α Syn binding to model vesicles admittedly do not help much to elucidate α Syn's normal physiological behavior at present, but they do raise some interesting questions. If model vesicles comprised only of lipids are known to resist swelling under osmotic tension, how then do actual synaptic vesicles grow to nearly double their size *in vivo* upon neurotransmitter loading without the loss of their contents? Even if synaptic vesicles swell *in vivo*, would swelling translate to more defects being present for the lipid

composition and conditions encountered in the synapse? How would the inclusion of synaptic proteins influence membrane dynamics? And what might the implications be for normal binding if indeed α Syn's affinity for membrane defects is independent of the presentation of such defects? Clearly, much work remains to be done in order to assemble a complete picture of α Syn's behavior *in vivo*.

In chapter 4, we took a different approach aimed at understanding the potential physiological relevance of the unstructured C-terminal domain of α Syn. In performing depletion-induced force experiments, we were able to show that the C-terminal domain confers steric stability for SSLBs similar to how a grafted polyelectrolyte might confer steric stability to a spherical colloid. Additionally, through the use of mono- and di-valent salts, we were able to demonstrate that there were both electrostatic and steric components contributing to the overall steric stability observed. Overall, our work helps to shed light on the behavior of α Syn's C-terminal domain and opens many doors for potential future exploration of the polyelectrolytic behavior of other intrinsically disordered proteins *in vivo*.

Taken together, the results discussed herein suggest that there is far more work to be done to uncover α Syn's true physiological behavior. As an intrinsically disordered protein, much of the field's traditional "structure determines function" dogma simply is not applicable for making predictions about the protein's behavior and interaction partners. Thus, only through the concerted and interdisciplinary efforts of many researchers from many different fields will we be able to finally elucidate α Syn's normal physiological role and make strides towards alleviating Parkinson's disease and other synucleinopathies.

Section 7.2: Future directions

Section 7.2.1: Probing α Syn binding with confocal microscopy

One of the primary advantages of my newly developed confocal binding assay is its high degree of customizability; with sufficient sampling, equilibrium binding parameters can be measured for any combination of membrane-binding protein and substrate vesicles, provided that both can be fluorescently-tagged with non-interacting fluorophores. As such, a logical extension to the work discussed in this thesis would be to characterize α Syn binding on other model vesicle systems in the physiological size limit exhibiting specific packing defect presentation. Previous work in the field has suggested that α Syn may preferentially bind to vesicles displaying a greater number of shallow defects; in these studies, shallow defects were explicitly emphasized by including a high proportion of either 1,2-diphytanoyl-*sn*-glycero-3-phosphocholine (DPhPC, a bacterial lipid species) or other lipids containing a single polyunsaturated tail into a planar membrane substrate of interest [1, 2]. While beneficial for our understanding of what factors may contribute to α Syn binding, it remains unclear how these observations would translate into a more physiological model system exhibiting both the high curvature and high charge density of native synaptic vesicles. Thus, I believe the field would benefit greatly from a comprehensive study aimed at characterizing differences in α Syn binding as a function of lipid defect presentation in the curvature and charge limit of actual synaptic vesicles. Such a study would ideally include (1) molecular dynamics simulations and PackMem defect analysis [3] for a variety of membrane compositions of increasing complexity and curvature, as well as (2) confocal binding data describing α Syn's association with the same membrane compositions. Working together, these

two techniques can solidify any potential link between membrane defect presentation and α Syn binding.

Another potential avenue for future study suggested by this work would be to explore α Syn binding parameters using purified synaptic vesicles as opposed to a synthetic model system. Synaptic vesicles are one of the few organelles whose composition has been fully explored and documented, including both exact copy numbers of all proteins present as well as the distribution of head groups and tails among all lipids present [4]; with this information in hand, it becomes clear that synthetic vesicle models, and particularly those without any synaptic protein, are likely not a good representation of actual synaptic vesicles *in vivo*. Thus, I believe the next big step in α Syn research would be to consider α Syn's behavior in the proper contextual environment of the synaptic vesicle, especially since synaptic vesicles have been shown to exhibit qualities otherwise unobserved in their synthetic model counterparts [5, 6].

Lastly, I believe that a promising future direction for work involving packing defects and protein binding would be to run experiments using a Langmuir trough. A Langmuir trough is an instrument uniquely capable of tuning the intermolecular packing and organization of an oriented lipid monolayer at an air/fluid interface; if the packing and organization can be uniquely tuned, my assumption is that defect presentation can be uniquely tuned as well. Experiments performed on a Langmuir trough would have the additional benefit of decoupling curvature from membrane defect presentation due to the flat geometry of the air/fluid interface. For these experiments, it would be interesting to explore the binding of α Syn and other peripheral membrane proteins as a function of the monolayer surface pressure – is there a critical surface pressure at which a protein

can no longer bind to the monolayer? How (if at all) does the amount of protein bound to the monolayer change as a function of the monolayer compression? Does the observed protein binding behavior change when lipids of different geometries are introduced into the monolayer? The possibilities are endless, but regardless of the direction I believe through experiments will help to shed some light on the miniscule and transient world of lipid packing defects.

Section 7.2.2: The C-terminal domain and steric stability *in vivo*

The force response experiments performed and discussed in chapter 4 demonstrated the ability of the C-terminal domain of wild-type α Syn to sterically-stabilize synaptic vesicle-like mimics. As many point mutations have been extensively studied elsewhere in the literature due to their implication in neuronal dysfunction, a logical extension to the work performed here would be to explore changes in the force response behavior for commonly-studied mutations encountered in Parkinson's disease or dementia with Lewy bodies, such as A53T or G51D [7]. If these point mutations outside of the C-terminal domain do indeed alter the force response behavior, such experiments would help to re-contextualize the role of the C-terminal domain *in vivo* and enforce the need for further interdisciplinary research. Additionally, I believe that future experiments building off of this work should pay special attention to the impact of phosphorylation on force response behavior, particularly at position S129 which has been implicated in Parkinson's disease. As phosphorylation alters the local charge environment *via* the introduction of more negative charge and we have shown here that charge plays a role in steric stabilization, it seems reasonable that this highly specific post-translational modification may have sweeping impacts on α Syn's physiological behavior.

Another avenue to pursue using force response experiments would be study the force response and critical clustering behavior of the different synuclein isoforms. β - and γ -synuclein differ from the α -isoform primarily in the sequence and length of the C-terminal domain; thus, it seems reasonable to expect that these isoforms will display different repulsive behavior. As previous work has shown that the different synuclein isoforms localize to different areas of the brain, it would be interesting to study how the cooperation or competition of the various isoforms contributes to differences in synaptic vesicle clustering and behavior in different regions of the brain [8].

Section 7.3: References

- [1] Garten, M. *et al. Phys. Chem. Chem. Phys.* **17**, 15589–15597 (2015).
- [2] Brummel, B. E., Braun, A. R. & Sachs, J. N *Biochim Biophys Acta Biomembr* **1859**, 529–536 (2017).
- [3] Gautier, R. *et al. Biophysical Journal* **115**, 436–444 (2018).
- [4] Takamori, S. *et al. Cell* **127**, 831–846 (2006).
- [5] Budzinski, K. L. *et al. Biophysical Journal* **97**, 2577–2584 (2009).
- [6] Lee, J.-S., Cho, W. J., Shin, L. & Jena, B. P. *Exp Biol Med (Maywood)* **235**, 470–477 (2010).
- [7] Meade, R. M., Fairlie, D. P. & Mason, J. M. *Molecular Neurodegeneration* **14**, 29 (2019).
- [8] Li, J.-Y., Henning Jensen, P. & Dahlström, A. *Neuroscience* **113**, 463–478 (2002).